Article:
Yang, Y., Hoeflich, P.A., Baade, D. et al. (2020) The young and nearby normal type Ia supernova 2018gv: UV-optical observations and the earliest spectropolarimetry. Astrophysical Journal, 902 (1). 46. ISSN: 0004-637X

https://doi.org/10.3847/1538-4357/aba759

Draft version March 27, 2019
Typeset using LaTeX **preprint** style in AASTeX62

The Young and Nearby Normal Type Ia Supernova 2018gv: UV-Optical Observations and the Earliest Spectropolarimetry

Yi Yang (杨轶) ,[1] Peter Hoeflich,[2] Dietrich Baade,[3] Justyn R. Maund,[4] Lifan Wang,[5,6] Peter. J. Brown,[5] Heloise F. Stevance,[4] Iair Arcavi,[7] Jamison Burke,[8,9] Aleksandar Cikota,[10] Alejandro Clocchiatti,[11] Avishay Gal-Yam,[1] Melissa. L. Graham,[12] Daichi Hiramatsu,[8,9] Griffin Hosseinzadeh,[13,8,9] D. Andrew Howell,[8,9] Saurabh W. Jha,[14,15] Curtis McCully,[8] Ferdinando Patat,[3] David. J. Sand,[16] Steve Schulze,[1] Jason Spyromilio,[3] Stefano Valenti,[17] József Vinkó,[18,19,20] Xiaofeng Wang,[21] J. Craig Wheeler,[20] Ofer Yaron,[1] and Jujia Zhang[22,23]

[1]*Department of Particle Physics and Astrophysics, Weizmann Institute of Science, Rehovot 76100, Israel*
[2]*Department of Physics, Florida State University, Tallahassee, Florida 32306-4350, USA*
[3]*European Southern Observatory, Karl-Schwarzschild-Str. 2, 85748 Garching b. München, Germany*
[4]*Department of Physics and Astronomy, University of Sheffield, Hicks Building, Hounsfield Road, Sheffield S3 7RH, UK*
[5]*George P. and Cynthia Woods Mitchell Institute for Fundamental Physics & Astronomy, Texas A. & M. University, 4242 TAMU, College Station, TX 77843, USA*
[6]*Purple Mountain Observatory, Chinese Academy of Sciences, Nanjing 210008, China*
[7]*The Raymond and Beverly Sackler School of Physics and Astronomy, Tel Aviv University, Tel Aviv 69978, Israel*
[8]*Las Cumbres Observatory, 6740 Cortona Drive, Suite 102, Goleta, CA 93117-5575, USA*
[9]*Department of Physics, University of California, Santa Barbara, CA 93106-9530, USA*
[10]*Physics Division, Lawrence Berkeley National Laboratory, 1 Cyclotron Road, Berkeley, CA 94720, USA*
[11]*Instituto de Astrofisica, Pontificia Universidad Catolica (PUC), Casilla 306, Santiago 22, Chile*
[12]*Department of Astronomy, University of Washington, Box 351580, U.W., Seattle, WA 98195, USA*
[13]*Harvard-Smithsonian Center for Astrophysics, 60 Garden Street, Cambridge, MA 02138, USA*
[14]*Department of Physics and Astronomy, Rutgers, the State University of New Jersey, 136 Frelinghuysen Rd., Piscataway, NJ 08854, USA*
[15]*Center for Computational Astrophysics, Flatiron Institute, 162 5th Avenue, New York, NY 10010, USA*
[16]*Steward Observatory, University of Arizona, 933 North Cherry Avenue, Rm. N204, Tucson, AZ 85721-0065, USA*
[17]*Department of Physics, University of California, Davis, CA 95616, USA*
[18]*Konkoly Observatory, MTA CSFK, Konkoly Thege M. ut 15-17, Budapest, 1121, Hungary*
[19]*Department of Optics & Quantum Electronics, University of Szeged, Dom ter 9, Szeged, 6720 Hungary*
[20]*Department of Astronomy, University of Texas at Austin, Austin, TX 78712, USA*
[21]*Physics Department and Tsinghua Center for Astrophysics (THCA), Tsinghua University, Beijing, 100084, People's Republic of China*
[22]*Yunnan Observatories (YNAO), Chinese Academy of Sciences, Kunming 650216, People's Republic of China*
[23]*Key Laboratory for the Structure and Evolution of Celestial Objects, Chinese Academy of Sciences, Kunming 650216, People's Republic of China*

(Received; Revised; Accepted)

Corresponding author: Yi Yang
yi.yang@weizmann.ac.il

Submitted to ApJ

ABSTRACT

The non-detection of companion stars in Type Ia supernova (SN) progenitor systems lends support to the notion of double-degenerate (DD) systems and explosions triggered by the merging of two white dwarfs. This very asymmetric process should lead to a conspicuous polarimetric signature. By contrast, observations consistently find very low continuum polarization as the signatures from the explosion process largely dominate over the pre-explosion configuration within several days. Critical information about the interaction of the ejecta with a companion and any circumstellar matter is encoded in the early polarization spectra. In this study, we obtain spectropolarimetry of SN 2018gv with the ESO Very Large Telescope at -13.6 days relative to the $B-$band maximum light, or $\sim$5 days after the estimated explosion — the earliest spectropolarimetric observations to date of any Type Ia SN. These early observations still show a low continuum polarization ($\lesssim$0.2%) and moderate line polarization (0.30±0.04% for the prominent Si II λ6355 feature and 0.85±0.04% for the high-velocity Ca component). The high degree of spherical symmetry implied by the low line and continuum polarization at this early epoch is consistent with explosion models of delayed detonations and is inconsistent with the merger-induced explosion scenario. The dense UV and optical photometry and optical spectroscopy within the first $\sim$100 days after the maximum light indicate that SN 2018gv is a normal Type Ia SN with similar spectrophotometric behavior to SN 2011fe.

Keywords: polarization — galaxies: individual (NGC 2525) — supernovae: individual (SN 2018gv)

1. INTRODUCTION

Thermonuclear supernovae (Type Ia SNe) have been very well calibrated at low redshift and are used as cosmic distance indicators out to redshift $z \sim 2$ (Riess et al. 1998; Perlmutter et al. 1999; Riess et al. 2016, 2018). However, this calibration is purely empirical and parametric, lacking a detailed physical foundation. The general consensus is that Type Ia SNe are powered by the ignition of degenerate nuclear fuel from carbon/oxygen white dwarfs (CO WDs, Hoyle & Fowler 1960, see e.g. Howell 2011; Hillebrandt et al. 2013; Maoz et al. 2014; Branch & Wheeler 2017; Hoeflich 2017 for recent reviews). However, it is still unknown how the thermonuclear runaway is triggered and propagates throughout the progenitor star (Arnett 1969; Nomoto et al. 1976; Khokhlov 1991; Niemeyer et al. 1996; Reinecke et al. 2002; Plewa et al. 2004; Röpke 2007; Pakmor et al. 2011, 2012; Seitenzahl et al. 2013). A comprehensive summarize and comparison of these works is provided by Branch & Wheeler (2017). The principal contenders are double-degenerate (DD) models, in which two WDs merge (Iben & Tutukov 1984; Webbink 1984), and single-degenerate (SD) models, in which a WD accretes matter from a companion (Whelan & Iben 1973) until the critical Chandrasekhar mass of $M_{\rm Ch} \sim 1.4 M_\odot$ is reached. There is some evidence that the Type Ia SN population could consist of both the SD and DD progenitor systems (see e.g. Maoz et al. 2014). It also remains unclear what the fractions are for various processes contributing to the Type Ia SN population.

Within this general picture for progenitors, three major classes of explosion have been proposed, which are distinguished by the triggering mechanism of the explosion,

1. Explosion of a single CO WD with a mass close to $M_{\rm Ch}$. The explosion is triggered by compressional heating near the WD center as a *deflagration* front. Because the compressional heat release increases rapidly towards $M_{\rm Ch}$, the exploding WD lands in a very narrow mass range (Hoeflich & Khokhlov 1996) though actual triggers may differ as much as slow accretion, pulsational instabilities, or nova eruptions. The donor star may be a moderately evolved Roche-lobe-overflowing star in an SD system (Whelan & Iben 1973) or a tidally disrupted WD in a DD system Whelan & Iben (1973); Piersanti et al. (2004);

2. Dynamical merging of two CO WDs in a binary system after losing or shedding angular momentum via gravitational radiation (Iben & Tutukov 1984; Webbink 1984; Benz et al. 1990; Nugent et al. 1997; Pakmor et al. 2010). The thermonuclear explosion is triggered by the heat of the merging process or as a consequence of the WD-WD collisions. It is unclear whether the dynamical merging process or a violent collision of two WD leads to a Type Ia SN, an 'accretion induced collapse' (AIC), or a WD with high magnetic fields (Rasio & Shapiro 1994; Hoeflich & Khokhlov 1996; Segretain et al. 1997; Yoon et al. 2007; Lorén-Aguilar et al. 2009; García-Berro et al. 2012)

3. Another class involves explosions of a sub-$M_{\rm Ch}$ CO WD triggered by detonating a thin surface He layer on the WD, which triggers a detonation front (Woosley et al. 1980; Nomoto 1982b,a; Livne 1990; Woosley & Weaver 1994; Hoeflich & Khokhlov 1996; Kromer et al. 2010).

In the SD channel, the explosions of Type Ia SNe are triggered by a subsonic ignition of degenerate material. If the pure subsonic deflagration (Reinecke et al. 2002) persists for the entire duration of the explosion, the front would result in a rather homogeneous angular distribution of the ejecta, in terms of both the material velocities and the chemical composition. The deflagration in $M_{\rm Ch}$ WDs, however, is not suitable to describe the class of normal Type Ia SNe because it fails to explain the rather high kinetic energy of the ejecta, the large amount of ^{56}Ni production (Hillebrandt et al. 2013), together with the presence of unburnt carbon and oxygen. A pure detonation scenario was also ruled out given the fact that the whole star is not burnt to iron and nickel. The delayed detonation scenario initially requires a subsonic deflagration that, after a period of time, transitions to a supersonic detonation (Khokhlov 1991). The detonation front burns the outer layers to intermediate mass elements (IME), i.e. from Si to Ca. The ejecta are predicted to be stratified in terms of density and chemical abundance, and hence exhibit significant homogeneity on large scales (Gamezo et al. 2005; Seitenzahl et al. 2013; Sim et al. 2013). Another mechanism suggests that the WD could explode at a sub-$M_{\rm Ch}$ (Fink et al. 2010). A CO WD accreting mass from a donor star, depending on the assumed mass transfer rates and the mass of the CO WD, could be able to accumulate a layer of helium which may develop to a degenerate-helium-shell flash under the right physical conditions (Taam 1980). Such unstable thermonuclear shell ignition could trigger a second detonation in the sub-$M_{\rm Ch}$ WD (Shen et al. 2010).

In the DD channel, the explosion of the SN could be triggered through a dynamic merger of two CO WDs (Pakmor et al. 2010). Starting from two CO WDs with masses of $0.9M_{\odot}$ and $1.1M_{\odot}$, the so-called violent merger model is able to reproduce the peak brightness, the color, as well as spectral shape and the velocity profiles of most of the line features, although the predicted rise time of the

$B-$band light curve is long compared to that of normal Type Ia SNe (Hayden et al. 2010). Other configurations, i.e. with very low mass-transfer rates, could fail to produce an explosive phenomenon and burn the C-O mixture into an O-Ne-Mg WD (Saio & Nomoto 1998) or form a single neutron star (Saio & Nomoto 1985). Thermonuclear explosions might also be triggered by direct, head-on collisions of WDs, and high-resolution numerical simulations are able to reproduce the primary observational signatures of Type Ia SNe (Kushnir et al. 2013).

One difficulty in distinguishing models reliably by means of conventional photometry or spectroscopy results from the ambiguity of the shape of the SN explosion. The geometry of the explosion and the structure of the SN ejecta, which are too distant to be spatially resolved, can only be probed with polarimetry. The polarized emission from a SN arises from a departure from spherical symmetry (Shapiro & Sutherland 1982). Electron scattering in asymmetric ejecta leads to the incomplete cancellation of electric field vectors (E-vectors), which produce nonzero degrees of observable polarization (Höflich 1991; Hoeflich et al. 1995). The continuum polarization tests whether the photosphere deviates from spherical symmetry, while line polarization traces mostly the distribution of elements in the SN ejecta. Material in the SN ejecta with considerable optical depth may unevenly block the photospheric light beneath, thereby producing a polarization variation and/or polarization position angle rotation in certain spectral features (Kasen et al. 2003; Wang et al. 2006).

Recent studies, in at least one case, have firmly established the progenitor as a compact object consistent with a WD (Nugent et al. 2011). The same data also excluded any luminous red giant companion star (Li et al. 2011). The absence of luminous red giants in Type Ia SN progenitor systems is corroborated by studies of supernova remnants in the Milky Way (González Hernández et al. 2012) and in the LMC (Edwards et al. 2012). These results favor the DD channel for Type Ia SNe. This process could be sufficiently asymmetric and lead to a clear polarimetric signature. By contrast, observations consistently find a very low continuum polarization (i.e. $\lesssim 0.2\%$, Wang & Wheeler 2008), with a diversity in subluminous events (i.e., SN 1999by, Howell et al. 2001 and SN 2005ke, Patat et al. 2012). Spectropolarimetry has only been available from ∼seven days past explosion and cannot penetrate the opaque ejecta that have already expanded beyond the innermost interaction zone. Low continuum polarization at these intermediate epochs indicates the photosphere is remarkably spherical (Wang & Wheeler 1996; Wang et al. 2003b; Maund et al. 2013; Zheng et al. 2017; Hoeflich et al. 2017). The approximate spherical symmetry is expected to be maintained in the SD models (Khokhlov 1991).

Recent high-cadence wide-field optical surveys and rapid follow-up observations of SNe, within hours of the explosion, are opening up a new phase in our understanding of SNe. This set of transients, discovered very early, will be extremely valuable for constraining the progenitor systems and explosion physics of SNe. The ejecta quickly sweep away almost all traces of the pre-explosion configuration within a few days. Such information is particularly valuable since it is directly connected to the final mass-loss history of the progenitor system right before the explosion. It is only accessible during the earliest phases. Early polarization measurements, before the pre-explosion configuration is left far behind by the rapidly advancing photosphere, can set constraints on the progenitor systems. Different degrees and types of asymmetry in the SN ejecta are produced by various multi-dimensional explosion models. Large departures in the global symmetry can be expected for dynamical processes. By contrast, $M_{\rm Ch}$ CO WD explosions triggered by a deflagration and sub-$M_{\rm Ch}$ CO WD explosions triggered by detonation of a He layer will mostly appear in the chemical distribution. Mergers can be

expected to produce large, time-variant continuum polarization whereas the latter cases may produce abundance asymmetries manifesting themselves in line polarization. Early polarimetry also provides unrivalled clues for differentiating various progenitor scenarios: e.g., high continuum polarization is expected for DD mergers (Pakmor et al. 2012, 2013; Moll et al. 2014; Raskin et al. 2014; Bulla et al. 2016a), low continuum but significant line polarization is predicted for delayed-detonation explosions (Khokhlov 1991; Hoeflich et al. 1995; Bulla et al. 2016b), and low line and continuum polarization should prevail in homogeneously mixed structures of deflagrations (Gamezo et al. 2004).

Polarimetry can also provide diagnostics for other Type Ia SN hypotheses. Theoretical models by Kasen (2010) show that the ejecta-companion interaction may be detected a few days past explosion. These predictions may be supported by a UV light curve excess (iPTF14atg, Cao et al. 2015) and a clearly-resolved blue bump in the light curve of SN 2017cbv (Hosseinzadeh et al. 2017). The early blue excess could, however, also be explained by vigorous mixing of radioactive ^{56}Ni in the SN ejecta (Hosseinzadeh et al. 2017; Miller et al. 2018). If such an early blue bump was caused by ejecta-companion interaction, the brightest bump would be observed from looking straight down the companion, from which the view is symmetric so that there is no net polarization. Large polarimetric signatures would come from an off-axis viewing angle in which the bump is fainter or invisible. Early polarimetry and its correlation with the light curve morphology would provide an important diagnostic of the ejecta-companion interaction case.

We present extensive UV-optical photometry, optical and near-infrared (NIR) spectroscopy, and optical spectropolarimetry of the nearby Type Ia SN 2018gv in the host galaxy NGC 2525. The organization of this paper is as follows: Observations and data reductions are detailed in Section 2. Section 3 describes the photometric evolution and estimates derived for the extinction arising in the host galaxy. Section 4 presents the spectral evolution and Section 5 investigates the spectropolarimetric properties of the SN. Discussions and a brief summary of the study are given in Section 6 and 7, respectively.

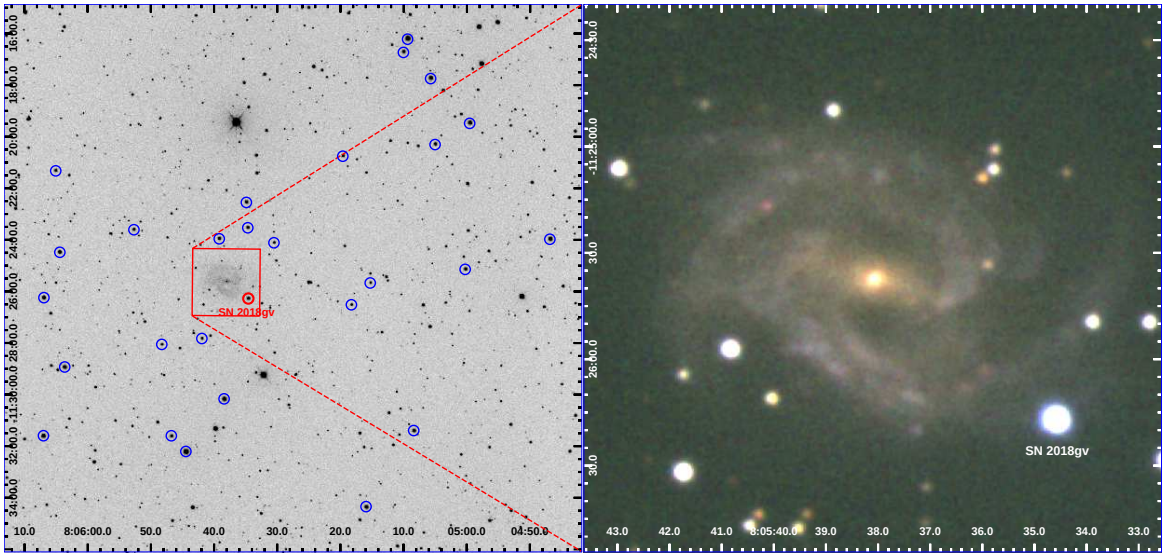

Figure 1. Left panel: LCO $V-$band image showing the location of SN 2018gv. Reference stars are marked with blue circles. The red square outlines the right panel. Right panel: color image of SN 2018gv in NGC 2525 from LCO B, V, and $r'-$band exposures. North is up, east is left.

2. OBSERVATIONS AND DATA REDUCTION

SN 2018gv was discovered at UT 2018-01-15 16:21:06 with an 0.5-m/f6.8 telescope at an unfiltered magnitude of 16.5 mag (Itagaki 2018). Follow-up spectroscopy on UT 2018-01-16 12:41:15 (Siebert et al. 2018) reveals that SN 2018gv was a very young, normal Type Ia SN, at $\sim 11-13$ days before the maximum luminosity according to the classification with SNID (Blondin & Tonry 2007). We measure its J2000.0 coordinates on the images obtained by the Sinistro cameras on Las Cumbres Observatory (LCO) Global Network of 1 m telescopes to be $\alpha = 08^{\rm h}05^{\rm m}34\farcs58$, $\delta = -11°26'16\farcs77$. SN 2018gv exploded $3\farcs46$ W and $39\farcs15$ S of the nucleus of the host spriral galaxy NGC 2525 (see Fig. 1). We queried the SIMBAD[1] database to retrieve reported heliocentric radial velocity measurements of the host galaxy. Among six reported measurements, we adopt a median value of 1582 km s^{-1} with a standard deviation of 12.6 km s^{-1}, which falls into the value obtained by the 2MASS catalog (Tully 2015). This implies a redshift of $z = 0.00527 \pm 0.00004$ for SN 2018gv, which is used throughout the paper together with the adopted Hubble constant of $H_0 = 73.24 \pm 1.74$ km s^{-1} Mpc^{-1} (Riess et al. 2016).

2.1. *Optical Photometry*

2.1.1. *Ground-Based Photometry*

Extensive $UBg'Vr'i'$ photometry was obtained with the Sinistro cameras on the LCO network of 1 m telescopes. The images were pre-processed including bias subtraction and flat-field correction using the BANZAI automatic pipeline (McCully et al. 2018). Figure 1 shows the field around SN 2018gv. Because the SN is bright and in the outskirts of the galaxy, template subtraction and PSF-fitting are not necessary. Therefore, the flux of the SN and the local reference stars were measured with a circular aperture of $3\farcs0$ in radius. The background was estimated by the median pixel value of an annulus around the SN with an inner radius of $9\farcs0$ and an outer radius of $12\farcs0$. We calibrated the instrumental BV and $g'r'i'$ magnitudes of SN 2018gv to the standard Johnson BV system (Johnson 1966) in Vega Magnitude and the SDSS photometric system (Fukugita et al. 1996) in AB magnitude, respectively, based on the magnitude of local comparison stars from the AAVSO Photometric All Sky Survey (APASS) DR9 Catalogue (Henden et al. 2016, see Table 1). $U-$band magnitudes are only available for five of the comparison stars from the All-sky spectrally matched Tycho2 stars catalogue (Pickles & Depagne 2010). The final $Bg'Vr'i'$ and $U-$band calibrations were carried out based on the median of the difference between catalogue magnitude and the instrumental magnitude of the 27 comparison stars and the five comparison stars, respectively. The field containing the comparison stars is also shown in the left panel of Fig. 1.

2.1.2. *SWIFT UVOT Photometry*

Ultraviolet and optical photometry was obtained using the Ultra-Violet/Optical Telescope (UVOT; Roming et al. 2005) on the Neil Gehrels Swift Observatory (Gehrels et al. 2004). Photometry was reduced using the pipeline of the Swift Optical Ultraviolet Supernova Archive (SOUSA; Brown et al. 2014) using the zero-points of Breeveld et al. (2011).

2.2. *Optical/Near-Infrared (NIR) Spectroscopy*

[1] http://simbad.u-strasbg.fr/simbad/

A journal of spectroscopic observations of SN 2018gv is provided in Table 2. The spectral sequence of SN 2018gv spans $t = -15.2$ to $+83.6$ days. All phases are given relative to the $B-$band maximum at MJD 58,149.698 or UT2018-01-31.698 (see Section 3) throughout the paper.

2.2.1. *LCO Optical Spectroscopy*

LCO optical spectra were taken with the FLOYDS spectrographs mounted on the 2m Faulkes Telescope North and South at Haleakala, USA and Siding Spring, Australia, respectively, through the Global Supernova Project. A $2''$ slit was placed on the target at the parallactic angle. One-dimensional spectra were extracted, reduced, and calibrated following standard procedures using the FLOYDS pipeline [2] (Valenti et al. 2014).

2.2.2. *Gemini Optical Spectroscopy*

We obtained an optical spectrum of SN 2018gv using the Gemini Multi-Object Spectrographs (GMOS, Davies et al. 1997) on Gemini North telescope on 2018-01-17 UT with an airmass of 1.22 (GN-2017B-Q-12; PI Howell). For this spectrum, we obtained 2×300 s exposures in both the B600 and R400 gratings with central wavelengths of 450 nm and 750 nm respectively. We covered the chip gap by moving the central wavelength for the second exposure by 5 nm and 7.5 nm for the blue and red setups respectively.

The Gemini data were reduced using the standard techniques using a combination of the Gemini-IRAF[3] and custom procedures written in Python[4]. We obtained observations of the *HST* spectrophotometric standard star, HZ44, as part of the same program. The sensitivity function was derived using the *HST* spectrophotometric data. The telluric correction was then derived from the standard star observation.

2.2.3. *Hobby-Eberly Telescope (HET) Spectroscopy*

Additional spectra covering the optical regime between 3700 and 10500 Å were taken with the Low Resolution Spectrograph 2 (LRS2, Chonis et al. 2016) on the 10-meter *Hobby-Eberly Telescope* (Ramsey et al. 1998). LRS2 is composed of two dual-arm spectrographs, LRS2-B and LRS2-R, each having two spectral regions with a $\sim$ 100 Å overlap. The LRS2-B UV-arm extends from 3700 Å to 4700 Å, while the Orange arm covers the 4600−7000 Å interval, with a resolving power of 1900 and 1100, respectively. The Red arm of LRS2-R records spectra from 6500 to 8420 Å while the range 8180 to 10500 Å is covered by the Far-Red arm, both having $R \sim 1800$ spectral resolving power. Both arms are fed by their own $12'' \times 6''$ Integral Field Unit (IFU) that contains 280 densely packed fibers with lenslet coupling. The diameter of a single fiber/lenslet is $\sim 0\farcs6$ on sky. The fill factor of both IFUs is $\sim$ 98% which provides very good spatial sampling on the sky without the need for dithering (see Chonis et al. 2016 for additional details).

The reduction of the LRS2 IFU data was done with self-developed IRAF[5] and Python scripts. Fiber-to-fiber transmission variations were corrected by observing at least one frame of blank sky during twilight and requiring a homogeneous, flat, output signal on the reconstructed image within the field of view. Wavelength calibration was performed by a combination of Hg and Cd spectral lamp

[2] https://github.com/svalenti/FLOYDS_pipeline
[3] https://www.gemini.edu/node/11823
[4] https://github.com/cmccully/LCOgemini
[5] IRAF is distributed by the National Optical Astronomy Observatories, which are operated by the Association of Universities for Research in Astronomy, Inc., under cooperative agreement with the National Science Foundation.

exposures for LRS2-B and an FeAr spectral lamp for LRS2-R. For sky subtraction, the mean sky spectrum was constructed by 3σ-clipping the fibers having signal exceeding the median of all fibers, then computing the median combination of all remaining fibers. Flux calibration was completed based on nightly observations of spectrophotometric standard stars taken at approximately similar airmasses to the SN. Telluric lines were removed from the final spectra by using a mean telluric spectrum (constructed from multiple observations of telluric standard stars) scaled to the flux level of the actual SN spectrum.

2.2.4. *SALT Optical Spectroscopy*

We observed SN 2018gv with the Southern African Large Telescope (SALT) using the Robert Stobie Spectrograph (RSS; Smith et al. 2006) on 2018-01-25.8 UT under Rutgers University program 2017-1-MLT-002 (PI: SWJ). We used the PG0900 grating and 1.″5 wide longslit with a typical spectral resolution $R = \lambda/\Delta\lambda \approx 1000$. Exposures were taken in four grating tiltpositions to cover the optical spectrum from 350 to 930 nm. The data werereduced using a custom pipeline based on standard Pyraf spectral reductionroutines and the PySALT package (Crawford et al. 2010).

2.2.5. *ARC Optical Spectroscopy*

On 2018-03-22 UT we obtained one low-resolution spectrum with the Dual Imaging Spectrograph (DIS[6], mounted on the 3.5 m Astrophysics Research Consortium (ARC) telescope at the Apache Point Observatory. The B400 and R300 gratings were used with central wavelengths of 4500 and 7500 Å , respectively. The instrument was rotated to the parallactic angle and 3×300 second exposures were obtained. The data were reduced using standard procedures and calibrated to a standard star obtained the same night using the PyDIS package (Davenport 2018).

The $UBg'Vr'i'$ lightcurves and FLOYDS/LCO spectra were obtained as part of the Global Supernova Project. All photometry and spectroscopy will become available via WISeREP [7] (Yaron & Gal-Yam 2012).

2.3. *VLT Spectropolarimetry*

Spectropolarimetry of SN 2018gv was conducted using the Focal Reducer and low dispersion Spectrograph (FORS2) on UT1 (Antu) of the ESO Very Large Telescope (VLT). Observations were carried out in the FORS2 Polarimetry with Multi-Object Spectroscopy (PMOS) mode (Appenzeller et al. 1998) on January 18 2018 (epoch 1) and January 31 2018 (epoch 2), corresponding to $t = -13.6$ day and $t = -0.5$ day, respectively. Details of the VLT spectropolarimetry are available in Appendix A. The intensity-normalized Stokes parameters (I, Q, U) are binned in ∼25 Å wide bins (∼7.5 pixels) to further increase the signal-to-noise ratio (S/N). The observed degree of linear polarization ($p_{\rm obs}$) and its position angle ($PA_{\rm obs}$) are given by:

$$\begin{aligned} p_{\rm obs} &= \sqrt{Q^2 + U^2}, \\ PA_{\rm obs} &= \frac{1}{2}\arctan\left(\frac{U}{Q}\right). \end{aligned} \tag{1}$$

The calculated $p_{\rm obs}$ is by definition a positive number and is therefore biased toward larger values than the true degree of polarization p. We correct the polarization bias following the equation given

[6] https://www.apo.nmsu.edu/arc35m/Instruments/DIS/
[7] https://wiserep2.weizmann.ac.il/

in Wang et al. (1997):

$$p = (p_{\rm obs} - \sigma_p^2/p_{\rm obs}) \times h(p_{\rm obs} - \sigma_p), \text{ and } PA = PA_{\rm obs}, \quad (2)$$

where σ_p gives the 1-σ uncertainty in $p_{\rm obs}$, h is the Heaviside step function. Calculation and bias correction of the polarization, as well as the estimation of associated uncertainties were performed by our own specially written software, following the prescriptions described by Patat & Romaniello (2006) and the scheme presented by Maund et al. (2007).

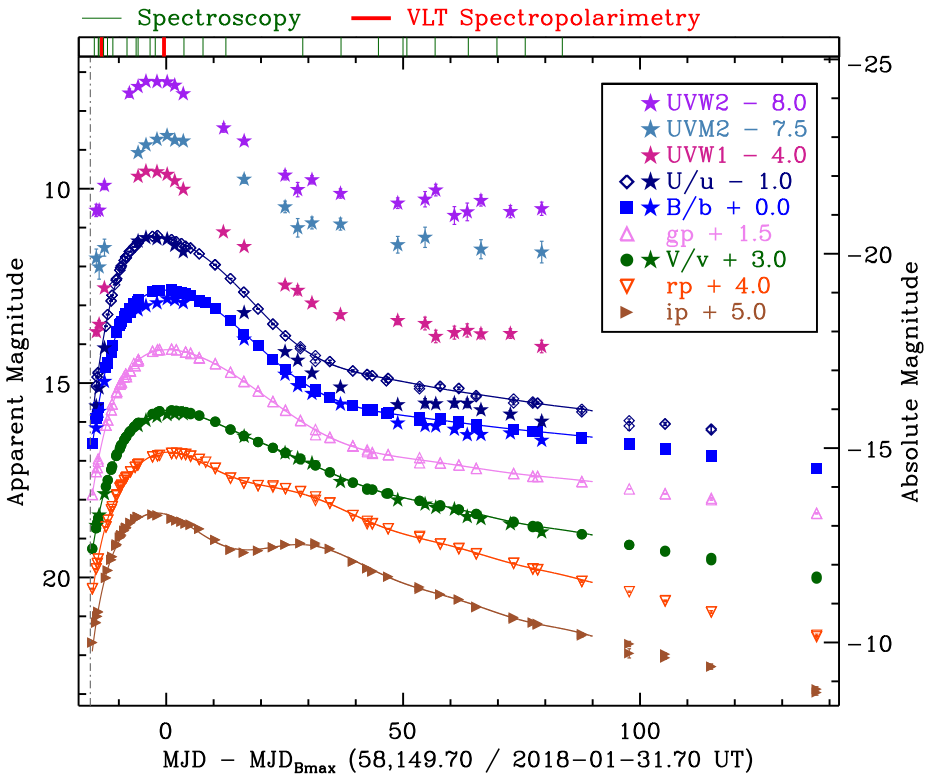

Figure 2. The optical light curves of SN 2018gv. The vertical dot-dashed line shows the time of discovery. Short vertical lines at the top of the panel mark the spectroscopic and spectropolarimetric observations. Solid curves present polynomial fits to the LCO photometry.

3. LIGHT CURVES OF SN 2018GV

In Fig. 2, we show the $UBg'Vr'i'-$band light curves after correction for interstellar extinction. The $uvw2$, $uvm2$, $uvw1$, u, b, and v photometry without the extinction corrections are also presented. The $UBg'Vr'i'-$band light curves were sampled during the period $t \approx -15$ to $+137$ days relative to the $B-$band maximum. We conduct high-order polynomial fits to the light curves before day $+110$ and plot the fits between the first observation and day $+90$. Short lines on the top axis indicate the epochs of spectroscopy and spectropolarimetry.

We list the calibrated LCO $UBg'Vr'i'$ Photometry in Table 3. All tabulated photometry was not corrected for the extinctions from the host and the Milky Way. Photometric parameters including the times of the light curve peaks, maximum brightness, the decline in the magnitude from the maximum light to the magnitude 15 days after, i.e. $\Delta m(15)$, which characterizes the width of the light curve,

are reported in Table 4. K-corrections were applied to our photometry when calculating $\Delta m(15)$. The presented values of the peak brightness have been corrected for the extinction from the Milky but not the host galaxy because we estimate little or no extinction from the host galaxy towards SN 2018gv. A detailed analysis of the extinction will be provided in the following subsection.

3.1. *Extinction*

The Galactic reddening towards the SN 2018gv line of sight has been estimated as $E(B-V)^{MW}_{18gv} = 0.051$ mag using the NASA/IPAC NED Galactic Extinction Calculator adopting the $R_V = 3.1$ extinction law (Cardelli et al. 1989) and the extinction map given by Schlafly & Finkbeiner (2011). We consider the host galaxy reddening to be low for the following reasons: 1) the SN's position in the outskirts of the host galaxy NGC 2525; 2) the evolution of the $B-V$ color of the SN is consistent with the Lira-Phillips relation at 30−90 days after the $B-$band maximum light (Phillips et al. 1999). Although an empirical relation between the amount of dust extinction and the strength of the absorption doublet of Na ID 5890 and 5896 Å has been proposed by Munari & Zwitter (1997) and widely used, the validity of the application of the methodology has been questioned for use with low-resolution spectra (Poznanski et al. 2011). All spectroscopic observations discussed in this study were carried out in a low-resolution regime, and thus we have not considered extinction estimation based on Na ID absorption features.

A linear relationship between the $B-$band magnitude and the $B-V$ color evolution of Type Ia SNe within a few days to approximately a month relative to the $B-$band peak brightness has been found by Wang et al. (2003a). This color-magnitude (CMAG) relation provides a robust way (denoted as the 'CMAGIC' method hereafter) to deduce the SN distance as well as the dust extinction from the host galaxy when the magnitude at the SN maximum light was also measured. Applying the 'CMAGIC' method, we deduce the color excess of SN 2018gv as $E^{18gv}_{BV} = 0.028 \pm 0.027$ mag, see Appendix B. A sanity test of the method based on the photometry of SN 2011fe (Munari et al. 2013) is also provided therein. Note that the color-magnitude relation has also been applied to the entire set of sample I of Carnegie-Supernovae Program (CSP I) (Krisciunas et al. 2017). For normal-bright Type Ia SNe like SN 2018gv, the color-magnitude diagram is stable but there is a systematic shift for transitional and subluminous Type Ia SNe as predicted by models (Hoeflich et al. 2017).

We also compare the $B-V$ color of SN 2018gv at 30−90 days after the $B-$band maximum light to the color evolution described by the Lira-Phillips relation (Phillips et al. 1999; Folatelli et al. 2010, see Equations 3a and 3b, respectively).

$$\begin{aligned} (B-V)_0 &= 0.725 - 0.0118(t_V - 60)\ \text{(a)}, \\ (B-V)_0 &= 0.732(0.006) - 0.0095(0.0005)(t_V - 55)\ \text{(b)}; \end{aligned} \tag{3}$$

The mean difference between the $B-V$ color and the Lira law given by Equation 3(a) is $E(B-V) = 0.036 \pm 0.018$ mag, which has a dispersion of 0.06 mag (see the lower left panel of Fig. 4). This is in good agreement with the estimation based on the CMAGIC method. The mean difference between the SN 2018gv observations and the Lira law fitted by Folatelli et al. (2010) gives $E(B-V) = 0.092 \pm 0.036$ mag. Considering a dispersion of 0.077 mag in the Lira law suggested by Equation 3(b), we conclude that the extinction estimated by the CMAGIC method agrees with that interpreted from the Lira law.

The final estimated values of the Galactic and the host galaxy extinction in different bandpasses are listed in Table 4. Here we have assumed that the dust in the host of SN 2018gv has similar

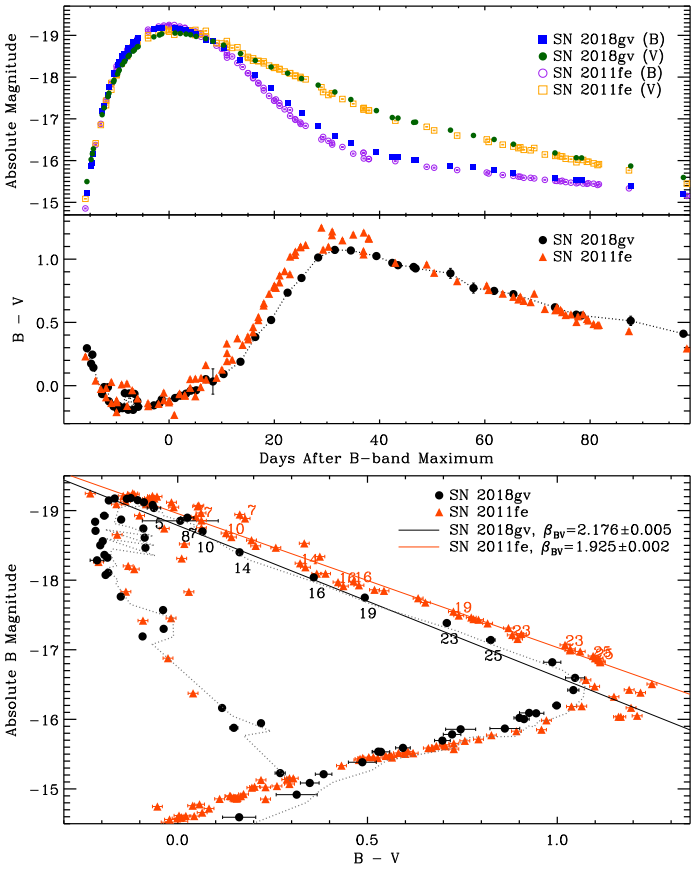

Figure 3. The upper panel presents the B and $V-$band light curves of SN 2018gv and SN 2011fe. The middle panel shows the color vs. rest-frame day plot. The dotted black line shows the $B-V$ color without the extinction correction of the host galaxy. In the bottom panel, the black circles and the orange triangles show the color-magnitude diagrams of SN 2018gv and SN 2011fe, respectively. The dotted black line is shown for comparison which represents the color-magnitude plot of SN 2018gv before correcting for the host extinction. The epochs within the linear regions are labeled by corresponding rest-frame days. The black and the orange solid lines are the linear fit to the linear regions of SN 2018gv and SN 2011fe, respectively.

properties as Galactic dust with $R_V = 3.1$. In this study, we only apply the extinction corrections for both the Galactic and the host component to SN 2018gv photometry when estimating the UV-optical pseudo-bolometric luminosities. This will be discussed in Section 4.2. Figure 3 illustrates the CMAGIC method applied to the $B-$band with $B-V$ color of SN 2018gv after correcting for the Galactic extinction. Similar diagrams derived from the well-sampled light curves of SN 2011fe are presented.

3.2. *Color Curves*

Figure 4 shows the color evolution of SN 2018gv ($uvw2-uvw1$, $uvw1-u$, $U-B$, $g'-r'$, $B-V$, and $r'-i'$), corrected for the Galactic and host reddening derived in Section 3.1. The color curves of SN 2018gv are overplotted with those of the Type Ia SNe 2011fe (Munari et al. 2013; Zhang et al. 2016), 2012fr (Contreras et al. 2018), and 2017cbv (Hosseinzadeh et al. 2017), corrected for reddening in both the Milky Way and the host galaxies.

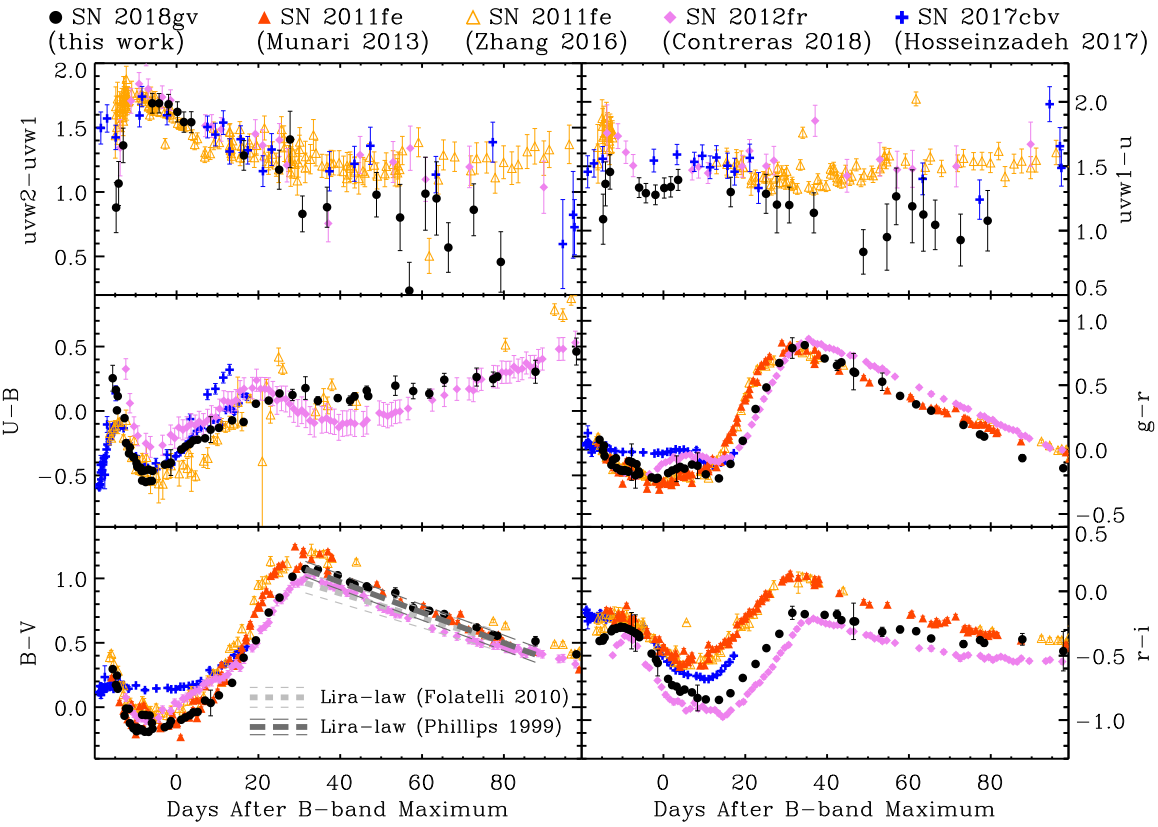

Figure 4. The Galactic and host reddening-corrected $uvw2 - uvw1$, $uvw1 - u$, $U - B$, $B - V$, $g' - r'$, and $r' - i'$ color curves of SN 2018gv compared with the Galactic reddening corrected color curves of SN 2011fe, SN 2012fr, and SN 2017cbv.

The $uvw2 - uvw1$ and $uvw1 - u$ colors of SN 2018gv appear to have similar trends to those of the selected SNe, except that SN 2018gv has bluer colors than the comparison SNe before $t \approx -10$ days, i.e. by $\sim$0.3 index. The early $U - B$ color of SN 2018gv shows a rapid decline and reached a minimum of ~ -0.5 mag at $t \approx -7$ days and then became redder in a linear fashion in magnitude space until t$\sim$ 25 days. The color curve hereafter entered a plateau phase and slowly turns red over time. SN 2012fr, exhibited a similar behavior, whereas SN 2017cbv and SN 2011fe became redder until $t \approx -14$ days, and then started to become bluer and reached the turning point at $t \approx -7$ days. The $B - V$ and the $g' - r'$ colors of the selected SNe show a similar evolution, except for SN 2017cbv, which displayed constant colors from the earliest epoch to t$\approx$ +7 days. The $r' - i'$ color curves of SN 2018gv and other selected SNe have very similar shapes but the rising phases to the secondary maximum display offsets of up to 10 days.

3.3. *Early Light Curves*

If SN 2018gv exploded as an ideal, expanding fireball with constant temperature and velocity, its luminosity should scale as the surface area of the expanding fireball, and therefore the SN flux (f) should increase quadratically with time (Riess et al. 1999). This $f \propto t^2$ relation reasonably describes the composite light curves collected from surveys (i.e. Riess et al. 1999; Goldhaber et al. 2001; Conley et al. 2006; Garg et al. 2007; Hayden et al. 2010; Ganeshalingam et al. 2011; Firth et al. 2015) and some of the very well sampled individual Type Ia SNe (i.e. SN 2011fe, Nugent et al. 2011).

A more fundamental explanation of the $f \propto t^2$ relation is provided by Arnett (1982) which considers radioactive heating and photon diffusion. Nonetheless, such an oversimplified expanding fireball may not be sufficient to explain the non-uniform and time-variant rising of Type Ia SNe in the first ∼3 days (for instance, SN 2013dy, Zheng et al. 2013 and iPTF16abc, Miller et al. 2018).

We model the early $g'-$band flux as a function of time from SN 2018gv as a power law:

$$f(t) \propto (t - t_0)^n, \tag{4}$$

where t_0 gives the time of first light, and n denotes the index of the power law. The best fit to the first 6.5 days after the estimated explosion gives $n = 2.43 \pm 0.48$ and a rise time $t_{\rm rise} = t_{Bmax} - t_0 = 18.51 \pm 0.92$ day, this is consistent with the fit using the first 6.0 days light curve, i.e. $n = 2.59 \pm 0.56$ and $t_{\rm rise} = 18.79 \pm 1.07$ day. The fit adopting the photometry within the first 7.0 days gives $n = 1.89 \pm 0.18$ and $t_{\rm rise} = 17.53 \pm 0.38$ days. One can see that the power-law index and the estimated rising time are broadly consistent with the mean values deduced by previous studies based on relatively arbitrary choices of the time range. Stringent constraints on the early photometric evolution of SN 2018gv, however, cannot be placed without a complete light curve coverage of the early phases.

For comparison, the model was also fitted to the early $g-$band flux of SN 2011fe, which yields one of the most comprehensive observed normal Type Ia SNe with photometry at ∼1 day after the explosion. In addition to adopting the $g'-$band photometry from Nugent et al. (2011), we also apply the transformations of Jordi et al. (2006) to convert the photometry by Zhang et al. (2016) from the $UBVRI$ magnitude system to the Sloan $ugriz$ system. A better sampled early $g-$band flux curve of SN 2011fe was then obtained by combining the two sources. The $f \propto t^n$ power law was fitted to the early (i.e. within 4 days of the estimated time of explosion) $g-$band flux. We obtain $n = 2.20 \pm 0.09$, which is marginally consistent with $n = 2.01 \pm 0.01$ derived by Nugent et al. (2011). The same conclusion holds for the data within the first five days, e.g. $n = 2.03 \pm 0.14$.

In a few cases, the early flux from the SNe exhibits significant deviations from the $f \propto t^2$ model. For example, the blue bump in the U, B, and $g'-$band light curves of SN 2017cbv during the first five days can be explained by interactions between the ejecta and the companion or immediate circumstellar material (Hosseinzadeh et al. 2017). The flux evolution of iPTF16abc at the first ∼four days can be modeled by the power law with $n = 0.98$ (Miller et al. 2018). The photometric and spectroscopic behaviors of iPTF16abc can be best explained by strong ^{56}Ni mixing in the SN ejecta. In these two cases, the early flux can be well characterized by $n \sim 1$.

To test whether SN 2018gv has such a nature, we fit the $f \propto t^n$ law to its early flux by fixing $n = 1$. The fluxes during the first four days after the estimated time of the explosion were adopted. After day 4, the fluxes of SN 2018gv display large deviations from the linear model. For comparison, the $f \propto t^n$ modeling to the fluxes of iPTF16abc and SN 2017cbv in similar phase spanning gives $n = 1.10 \pm 0.12$ and $n = 0.95 \pm 0.04$, respectively, both coincide with the linear model. We conclude that the early flux of SN 2018gv does not favor an n ∼1 index due to the large deviations from the linear model after day 4. Figure 5 summarizes our investigation of the early flux evolution of SN 2018gv and several other SNe discussed above. In all cases the fits were were forced to go through the origin, which determines the time of explosion. Filled symbols represent the data point used in each case. Data points shown by the corresponding open symbols were not used in the fitting. The left panel presents the fitting to the early flux curve of SN 2018gv which allows n to vary. The right

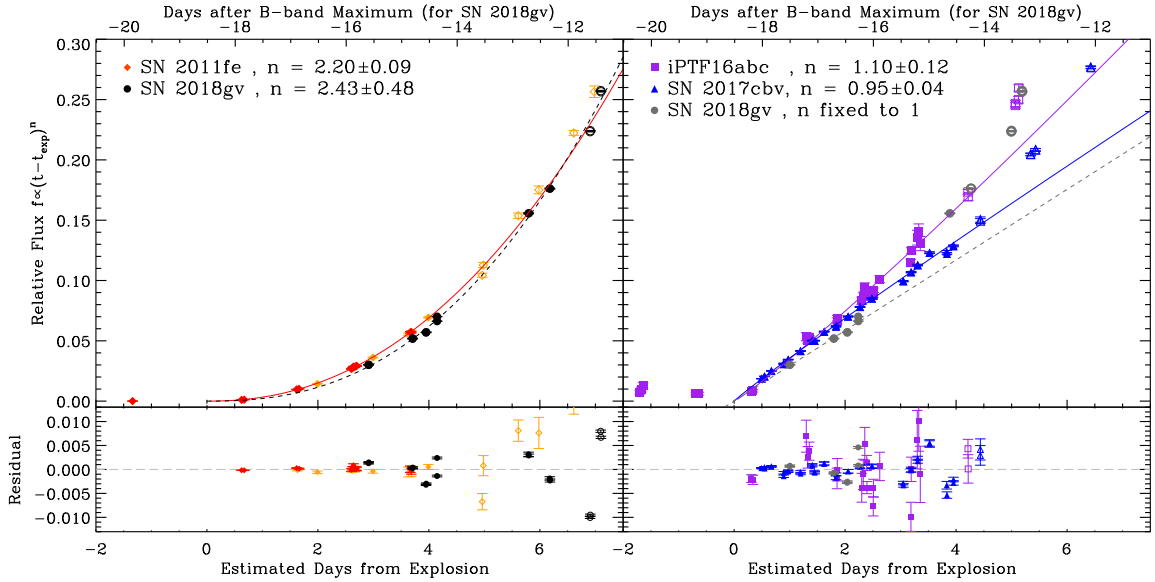

Figure 5. The best-fit $f \propto t^n$ model to describe the early $g'-$band flux from SN 2018gv compared to the early flux evolution of other SNe that have well-sampled early light curves. In the upper-left panel, the black-dashed line shows the fitting of SN 2018gv which allows n to vary. The red-solid line fits the early $g-$band flux of SN 2011fe. The orange diamonds indicate the $B-$band flux of SN 2011fe. In the upper-right panel, the gray-dashed line indicates the linear fit assuming the early flux evolution of SN 2018gv is similar to SN 2017cbv and SN 2018gv, a blue bump has been observed within 5 days after their estimated time of explosion. The residuals are shown in the bottom panels.

panel tests the case of n fixed to 1. The best fits for SN 2018gv and other SNe are shown by dashed lines and solid lines, respectively. Estimates based on different assumptions for the light-curve shape at early phases yield different times of explosion. We concede that the relatively sparsely sampled early light curve is not sufficient to constrain the first light of SN 2018gv. Overall, based on the test and comparisons above, we consider that the early flux evolution of SN 2018gv more resembles the average behavior of normal Type Ia SNe.

4. SPECTROSCOPY

Figure 6 presents the spectral sequence of SN 2018gv. A total number of 26 optical low-resolution spectra spanning from $t \sim -15.2$ to +83.6 days relative to the $B-$band maximum light were obtained. All spectra were corrected for the redshift of the host galaxy and smoothed by rebinning the data to 3 Å. The wavelength scale was corrected to the rest-frame using the host galaxy recessional velocity (1582 km s^{-1}) as described above.

Figure 7a compares the earliest spectrum of SN 2018gv at day −15.2 with the spectrum of SN 2011fe at day −16. The earliest spectrum of SN 2018gv exhibits several prominent broad and blue-shifted absorption features near 3630 Å due to Ca II H&K, (rest-frame wavelength λ_0 ∼3969, 3934 Å); the characteristic 'W'-shaped S II lines of the Type Ia SN spectra before and around the peak (λ_0 ∼5454, 5640 Å); the distinctive strong absorption features around 6020 Å due to Si II ($\lambda_0 \sim$ 6355 Å, denoted as Si II λ6355 hereafter) and around 7890 Å due to the Ca II NIR triplet ($\lambda_0 \sim$ 8579 Å, denoted as Ca II NIR3 hereafter). The C II λ6580 and the O I λ7774 are both identified in the earliest spectra. Oxygen in the ejecta of Type Ia SNe can be unburned fuel or a product of carbon burning. Apart

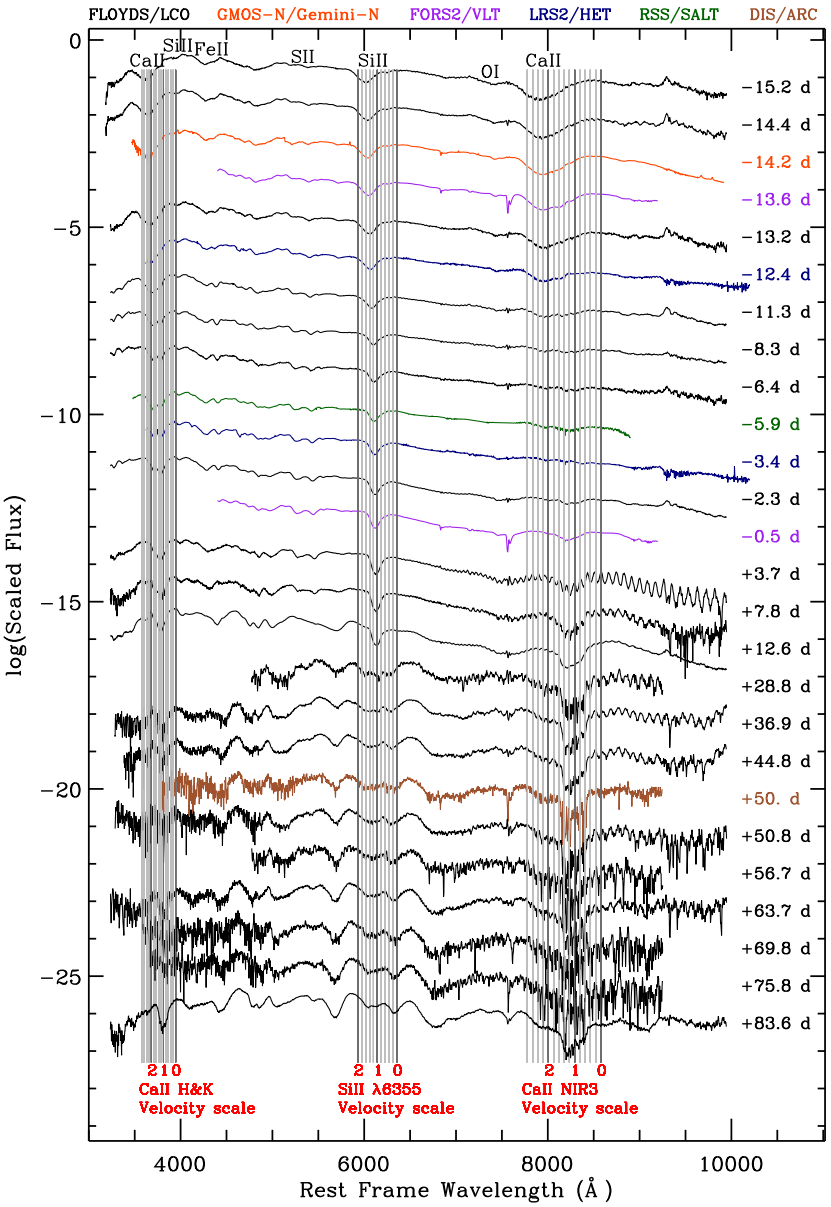

Figure 6. Spectral time series of SN 2018gv (solid curves, phase is label on right). The wavelengths corresponding to 0 km s^{-1}, −10,000 km s^{-1} and −20,000 km s^{-1} around the features indicated by the text are shown as thick gray lines, with 2000 km s^{-1} intervals denoted by thin gray lines. For the purpose of presentation, all spectra were binned to 3 Å.

from an absence of a shoulder on the red wing of the Ca II NIR3 in the SN 2018gv spectrum, we suggest that the spectral features and their strength in the earliest spectrum of SN 2018gv exhibit considerable similarities to those of the SN 2011fe.

By $t \sim -2$ day (shown in Fig. 7b), the width of the broad absorption feature associated with Si II λ6355 develops into a narrower profile, while the adjacent C II λ6580 feature is no longer distinguishable in our observations of SN 2018gv. C II λ6580 is marginally detected in the comparison spectrum of SN 2011fe at an earlier epoch of −5 day. An asymmetric and broad absorption profile is identified in the wavelength range of Ca II NIR3, indicating the existence of a high-velocity (HV)

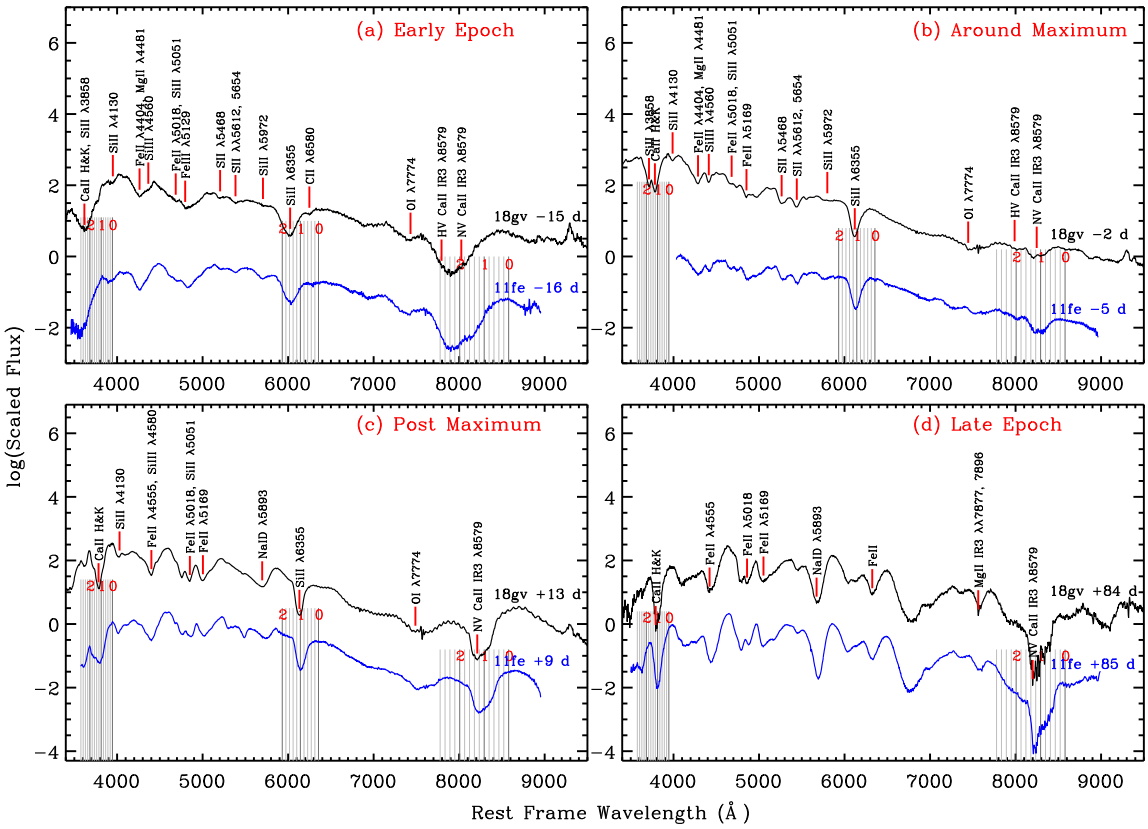

Figure 7. Spectra of SN 2018gv (black) at different epochs compared with the spectra of SN 2011fe (blue) at similar phases (Zhang et al. 2016). The wavelengths corresponding to 0 km s^{-1}, −10,000 km s^{-1} and −20,000 km s^{-1} around the features indicated by the text are shown as thick gray lines, with 2000 km s^{-1} intervals denoted by thin gray lines. All spectra have been corrected for the redshift of the host galaxy. Several prominent lines at different epochs are labeled. The line identifications adopted here are obtained from Branch et al. (2005, 2006). For the purpose of presentation, all spectra were binned to 3 Å, shifted arbitrarily, and presented in logarithmic scale.

component and a normal-velocity (NV) component of the Ca II feature. These two components were blended in the earliest spectra and become shallower. The decomposition and a detailed study of the Ca II NIR3 features of SN 2018gv will be presented in the following subsection. The HV and NV components of the Ca II NIR3 become shallower than those observed at −15 day. At +13 (Fig. 7c) and +84 day (Fig. 7d), significant similarities between the spectral evolution of SN 2018gv and SN 2011fe can be identified. In the following subsections, we detail the spectral evolution of SN 2018gv within the first ∼100 days.

4.1. *Evolution of the Features Around Si II λ6355 and Ca II NIR Triplet*

The prominent Si II λ6355 absorption feature in the early spectra suggests the spectral evolution of SN 2018gv resembles other normal Type Ia SNe. The highest velocity measured across the Si II λ6355 line is ∼ −16,000 km s^{-1} and a blue wing out to about 22,000 km s^{-1} at t∼ −15.2 day. The Si II λ6355 velocity for SN 2018gv measured from the spectra at −0.5 day is found to be ∼ −11,000 km s^{-1}. This is consistent with the interpolation of the exponential fitting to the time-evolution of the velocity profile, i.e. −10,870 km s^{-1}. These measurements suggest that SN 2018gv should be

classified as a normal-velocity (NV) Type Ia SN in the scheme of Wang et al. (2009). The expansion velocity gradient calculated directly from the Si II λ6355 at day -0.5 gives $\dot{v} = 36.6 \pm 6.4$ km s^{-1} day^{-1}. The calculation is also consistent with the velocity gradient measured by interpolating the exponential fitting to the same velocities during the period from $t = 0$ to $+10$ days, i.e. $\dot{v} = 33.3$ km s^{-1} day^{-1}. This is below the threshold of the high-velocity gradient subclass in the classification scheme of Benetti et al. (2005), i.e. $\dot{v} \sim 70$ km s^{-1} day^{-1}. Therefore, we suggest that SN 2018gv belongs to the low-velocity gradient group.

Figure 8 provides the detailed evolution of the Ca II H&K, Si II λ6355, and Ca II NIR3. HV features (HVF) are ubiquitous in the Ca II NIR3 in early phases of Type Ia SNe (Mazzali et al. 2005). We find no sign of an HV component of Si II λ6355 in the spectral time-sequence of SN 2018gv. The broad and asymmetric Ca II NIR3 profiles indicate multiple velocity components associated with Ca II. The Ca II H&K line may have similar HV components, but they appear to overlap with the Si II λ3858 line at early phases.

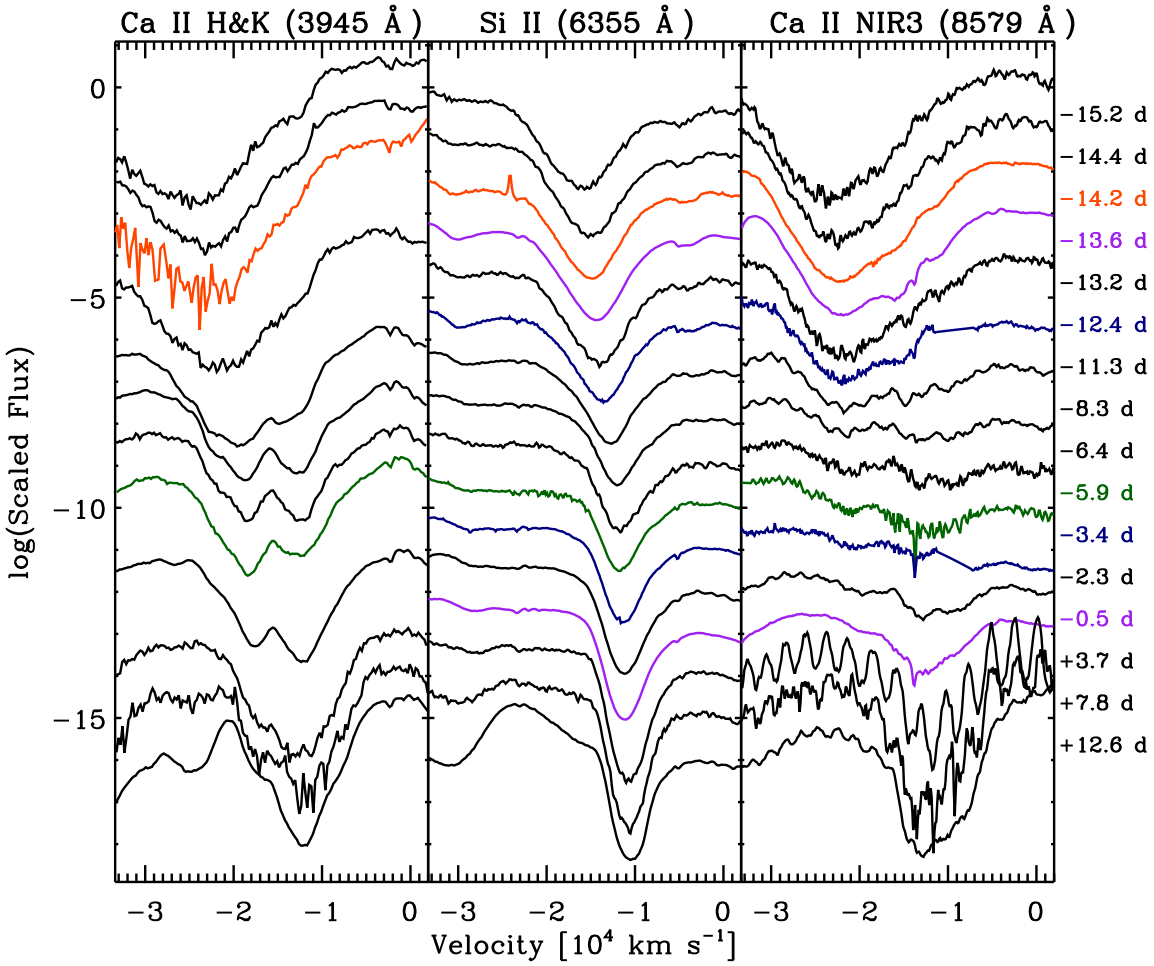

Figure 8. Evolution of Ca II H&K (left panel), Si II λ6355 (middle panel), and Ca II NIR3 (right panel) of SN 2018gv in velocity space. The semi-regular fluctuations in some of the Ca II NIR3 profiles are caused by fringing in the detectors.

In addition to displaying an absorption profile around the 'photospheric' velocity, some elements show a HVF which would require noticeably higher velocities (typically a few thousand km s^{-1} above the photospheric velocity). These absorption lines can be attributed to the materials above the SN photosphere, and has been interpreted as the exponentially declining abundances of Si and other intermediate mass elements, a signature of detonations in C/O rich material (Quimby et al. 2007). The Doppler-broadened profiles at different velocities often overlap with each other as well as the continuum profile. In order to mitigate the line blending and identify different line profiles, we adopt multiple-component Gaussian functions to fit the Si II λ6355 and the Ca II NIR3, separately. Note that the shape of the absorption feature is dependent on the structure and the velocity distribution of the absorbing material, therefore the profile is intrinsically non-Gaussian and can be complex (Mulligan & Wheeler 2018; Mulligan et al. 2019). One should be cautious about the inferred line properties based on multiple-component Gaussian fitting.

First, following Childress et al. (2014), we assign the blue and red ends of the feature of interest by visually inspecting the data; second, we identify a line segment as the 'pseudo-continuum' by connecting the blue and the red end; third, we subtract the flux of the segment profile from the feature of interest; finally, we fit the 'pseudo-continuum' removed regions with the multiple-component Gaussian function:

$$f_c(\lambda) = \sum_{i=1}^{n} A_i \exp\left(- \frac{(\lambda_i - \lambda_i^{\rm rest})^2}{2\sigma_i^2} \right). \quad (5)$$

The fitted parameters are the center wavelength in the rest-frame (λ_i), pseudo-equivalent width (σ_i), and absorption depth (A_i) of each component. A three-component Gaussian function is used to fit the absorption features of the Si II λ5972, Si II λ6355, and C II λ6580 line complex before $t \sim -11$ day. A fourth-component Gaussian function did not find any signature of HV Si II λ6355. The unburned-carbon lines are typically singly ionized (Tanaka et al. 2008) and manifest themselves at the earliest spectra of Type Ia SNe as weak and time-evolving C II λ6580 absorption lines (for example, see recent studies of Parrent et al. 2011; Thomas et al. 2011; Folatelli et al. 2012; Silverman & Filippenko 2012). The unburned carbon and oxygen would be accelerated with the expanding layers and trace the ejecta. The C II λ6580 line in SN 2018gv was as strong as the Si II λ5972 in the earliest spectra around two weeks before the $B-$band light curve peak. It faded rapidly and became indiscernible in the spectra obtained after approximately one week before the $B-$band maximum light, suggesting it is mostly concentrated in the outer part of the ejecta. Therefore, the three-component Gaussian function fitting was only applied before $t \sim -11$ day. The two-component Gaussian fitting procedure has been carried out since $t \sim -11$ day to fit the Si II λ5972 and Si II λ6355 simultaneously. The HV and the photospheric velocity component of the Ca II NIR3 features around the rest-frame wavelength λ8579 Å are also fitted with a two-component Gaussian function. The HV feature was prominent at early phases and faded to almost unseen after the $B-$maximum. The fitting procedure together with the temporal evolution of these two line regions is illustrated in Fig. 9. The velocity evolution of SN 2018gv in early phases is presented in Fig. 10.

Starting from about two weeks after the $B-$maximum, as the photosphere recedes more deeply into the ejecta, lines of intermediate-mass elements ($9 \leqslant Z \leqslant 20$) become significantly weaker while the iron-group elements ($21 \leqslant Z \leqslant 30$) like Fe II start to dominate the spectra. The Si II λ6355 absorption feature remains distinct at v =10,700 km s^{-1} on day +12.6 and has become difficult to identify in the spectra on +28.8 day and +36.9 day.

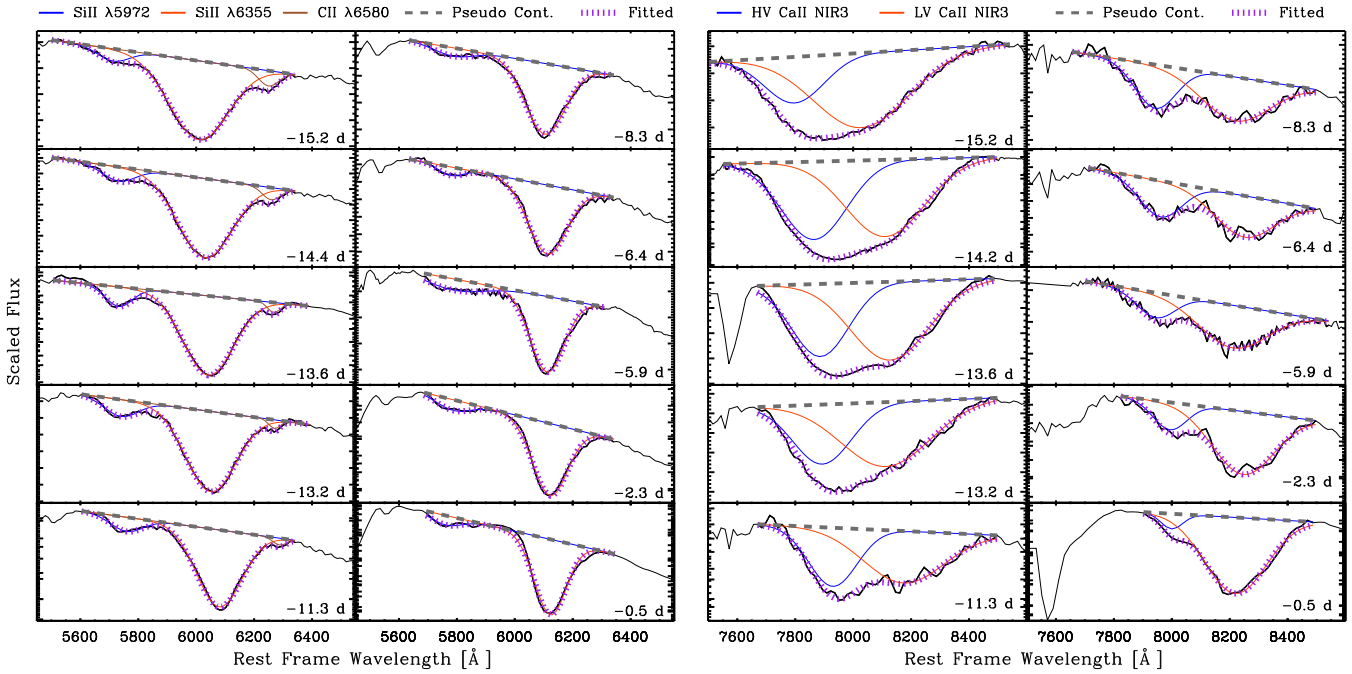

Figure 9. Gaussian fit to the early-time spectra of SN 2018gv. The left panel shows the fit to the region dominated by the Si II λ6355 feature. The fitting shown in the leftmost subpanels has taken into account the Si II λ5972, Si II λ6355, and C II λ6580 features, and the remaining five subpanels show the fitting that does not include C II λ6580. The right panel presents the fit for the region covering both the HVF and photospheric velocity Ca II NIR3 features.

We measure the pesudo-equivalent width (pEW) of the absorptions of the Si II λ5972, Si II λ6355, C II λ6580, the HV and the NV Ca II NIR3 features and analyze their time-evolutions. We also compare the results with those from SN 2011fe as shown in Fig. 11. According to Fig. 9, these features are all embedded in a well-determined pseudo-continuum. We calculate the pEW (e.g., Garavini et al. 2007; Silverman et al. 2012) defined as

$$pEW = \sum_{i=1}^{n} \Delta\lambda_i \left(\frac{f_c(\lambda_i) - f(\lambda_i)}{f_c(\lambda_i)} \right), \tag{6}$$

where λ_i denote the wavelengths of each one of the total N resolution elements in the pseudo-spectrum ranging from the blue endpoint to the red endpoint, $\Delta\lambda_i$ gives the width of the ith resolution element, $f(\lambda_i)$ represents the spectral flux at λ_i and $f_c(\lambda_i)$ is the flux of the pseudo-continuum at λ_i. The 1σ uncertainty of the pEW was derived by error propagation of the uncertainty in the measured flux at each resolution element.

In Fig. 11, the pEW of the Si II λ6355 reached a minimum around 73 Å at ~ -6 day. The pEW of the NV component of Ca II NIR3 reached a minimum of $\sim$25 Å at a similar epoch around -6 day to -2day and became larger until approximately one week after the $B-$band maximum light. The evolution of the pEW of SN 2011fe adopted from Zhao et al. (2015) is shown for comparison. The absorption strength of the HV Ca II NIR3 displays a slower decline in SN 2018gv compared to that of SN 2011fe. Other major absorption features exhibit similar trends as seen in SN 2011fe, as well as several other Type Ia SNe, i.e. see Fig. 15 of Zhang et al. (2016).

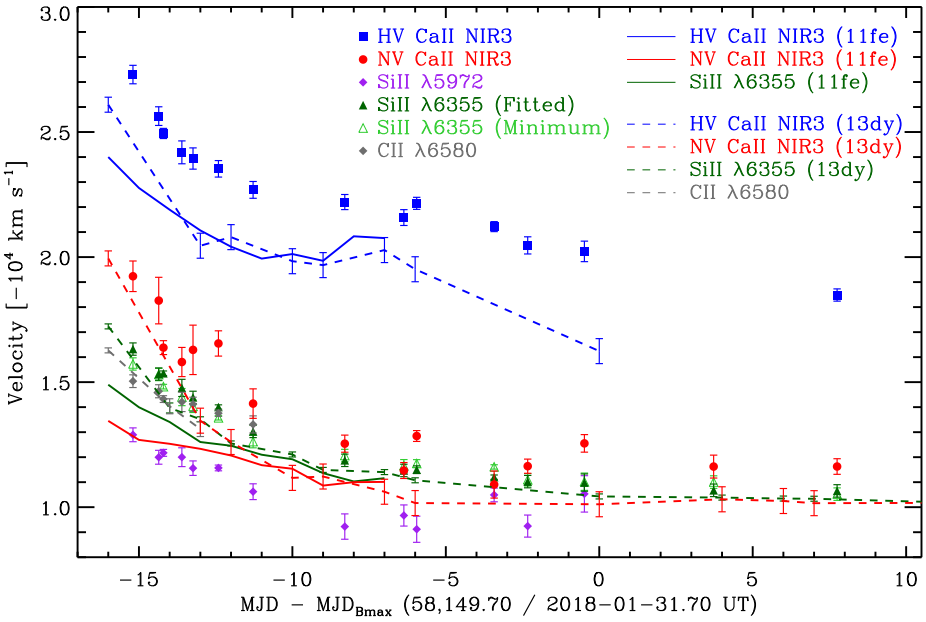

Figure 10. Evolution of the expansion velocity of SN 2018gv in early phases measured from different spectral features including Si II λ5972/6355, C II λ6580, and the HVF together with the photospheric velocity features of the Ca II NIR3. The central wavelength of each absorption component was determined through the multiple-component Gaussian fitting procedure. The local minima of Si II λ6355 were also overplotted and examined to be consistent with the central wavelength of the same feature obtained by the fitting process. The velocity evolution of the line absorptions for SN 2011fe (Zhao et al. 2015) and SN 2013dy at similar phases (Zhai et al. 2016) is shown for comparison.

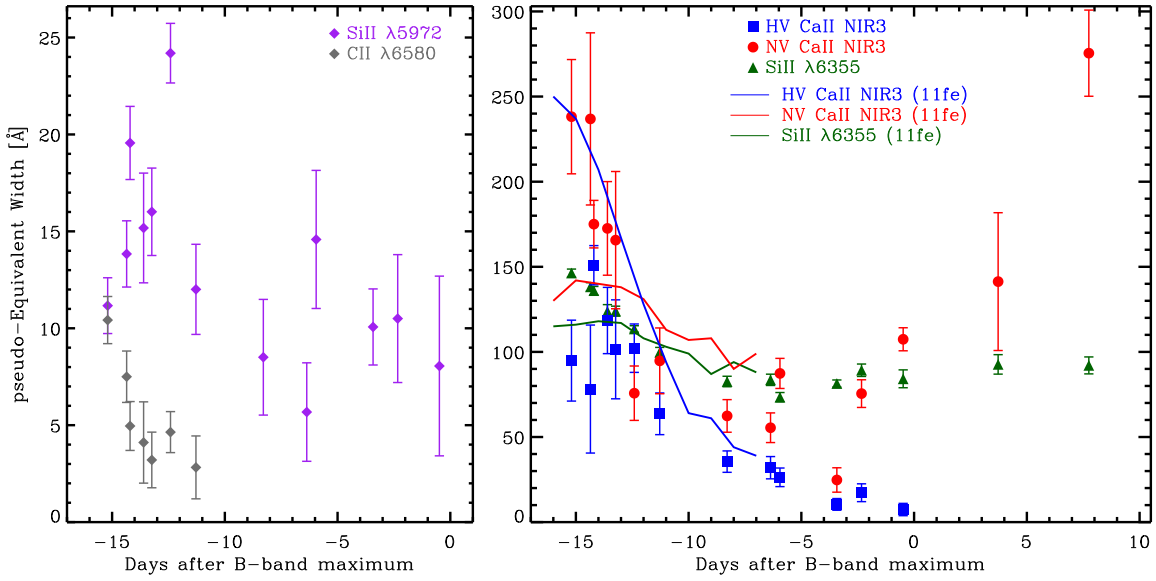

Figure 11. Evolution of the pseudo-equivalent width of SN 2018gv measured for the absorption lines Si II λ5972, C II λ6580 (left panel), Si II λ6355, HVF and photospheric velocity Ca II NIR3 (right panel). In the right panel we also compare the measurement of SN 2018gv with SN 2011fe.

The fit results of the different velocity components are presented in Table 5. The uncertainty in the measurement of the absorption velocity was converted from the associated error in wavelength, which has been estimated by adding the propagated error of the fitted center wavelength (see Equation 5), the rms value in wavelength calibration (typically less than 0.3 Å), and half of the size of the smallest resolution element ($\Delta\lambda/2 = \lambda/2R$), where R gives the spectral resolution in quadrature. The estimated uncertainty mainly depends on the spectral resolution and the S/N of the spectrum.

4.2. *Pseudo-bolometric Luminosity*

As discussed by Brown et al. (2016), estimating the bolometric luminosity of Type Ia SNe could be better carried out by employing flux-calibrated spectrophotometry. The diversity in the UV flux distributions, as well as the lack of NIR information could introduce erratic systematical uncertainties. To better quantify the bolometric characteristics of SN 2018gv, we compute the pseudo-bolometric luminosity of SN 2018gv over a wavelength range from $\sim 1660 - 8180$ Å based on the Swift $uvw2$, $uvm2$, $uvw1$, and the LCO $UBg'Vr'i'$-band photometry. We also conduct a similar calculation for SN 2011fe and compare the result to SN 2018gv. The construction of the spectral energy distribution (SED) of SN 2018gv is illustrated by Fig. 12 and the steps are detailed in Appendix C.

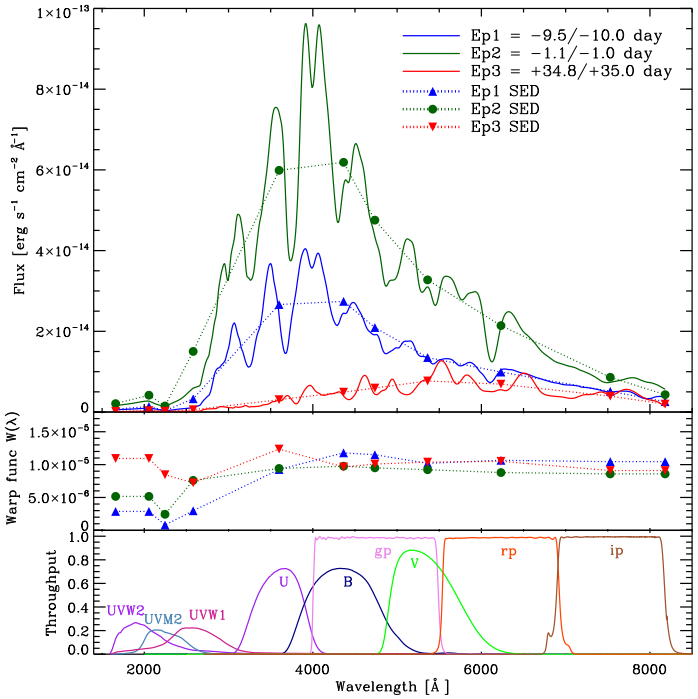

Figure 12. The constructed SED for SN 2018gv. In the upper panel, dots in three different colors show the bandpass monochromatic flux from each of three observations at their effective wavelengths. Dotted lines show the SED constructed with the warping procedure, and solid lines present the warped spectra from Hsiao's template (Hsiao et al. 2007) for the nearest integer epoch (see legend). The middle panel gives the value of the warp function. The lower panel presents the associated bandpasses throughput curves for the SN 2018gv observations.

The UV-optical pseudo-bolometric light curve of SN 2018gv is shown in Fig. 13. For comparison, we also apply the same procedure to the Swift $uvw2$, $uvm2$, $uvw1$ and the $UBVRI$ photometry

(Zhang et al. 2016) of SN 2011fe. We adopt a Cepheid distance modulus of 6.4 Mpc for SN 2011fe (Shappee & Stanek 2011), which is the same as the distance applied in the bolometric luminosity calculation conducted in Zhang et al. (2016). The calculated pseudo-bolometric light curve of SN 2011fe is also shown in Fig. 13. The integration of the SN 2011fe SED was performed over the same wavelength range as SN 2018gv. The middle panel presents the ratio of the UV (1660−3200 Å) to optical (3270−8180 Å). The UV/optical flux ratio ($F_{UV}/F_{\rm Optical}$) of SN 2018gv is comparable to that of SN 2011fe, both of which reached their peak about six days earlier than the bolometric luminosity. This suggests a relatively short diffusion time for their higher-energy photons. We also calculated the fraction of UV to optical flux relative to the total bolometric luminosity over the wavelength range of 1660−24000 Å ($F_{UV-\rm Optical}/F_{\rm Total}$) by integrating the composite spectral template created by Hsiao et al. (2007). This fraction was divided from the pseudo-bolometric luminosity for both SNe to provide a raw estimation of their bolometric luminosity, which is shown by the dashed lines in the first panel.

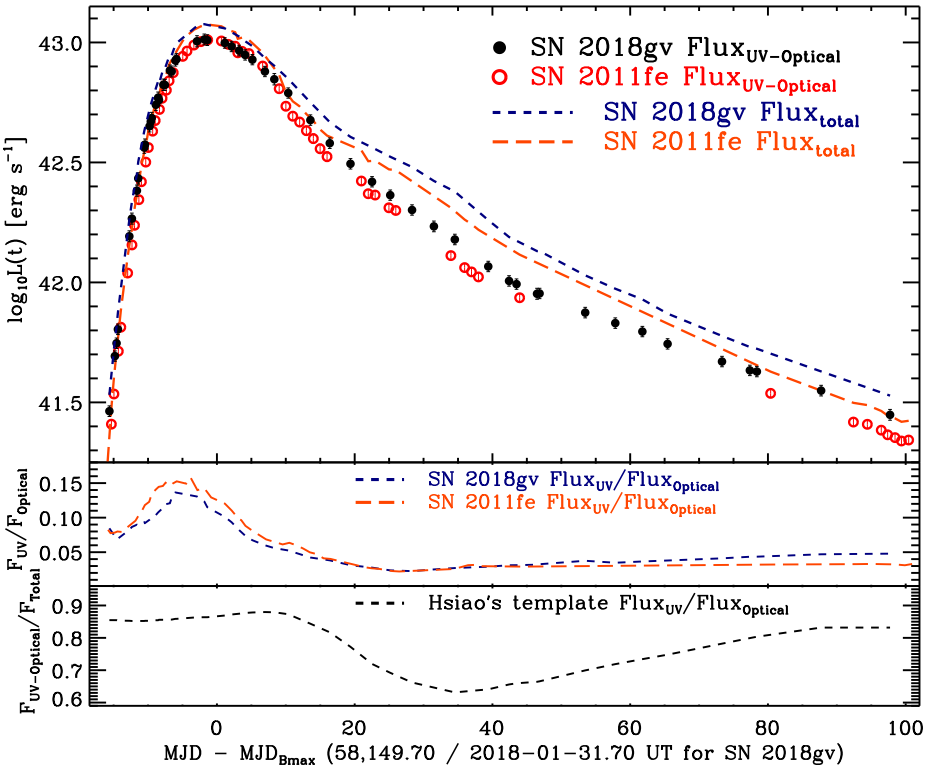

Figure 13. The constructed quasi-bolometric light curves of SN 2018gv (upper panel). The filled black circles represent the bolometric luminosity integrated within a wavelength range of 1660−8180 Å, the open red circles estimate the total bolometric luminosity based on the fraction of optical to total luminosity computed based on SN 2012fr, which is shown by the gray line in the lower panel. The middle panel presents the ratio of the UV (1660−3200 Å) to optical (3270−8180 Å) flux of SN 2018gv compared to that of SN 2011fe. The fluxes were derived by integrating the composite spectral template (Hsiao et al. 2007) as described in Section 4.2.

We tabulate the pseudo-bolometric luminosity of SN 2018gv and SN 2011fe calculated within the UV to optical wavelength ranges within the first 100 days after the $B-$band peak in Table 6. For each SN, the estimated UVOIR luminosity is also presented, which has similar error as the UV-

Optical pseudo-bolometric luminosity. The maximum value of the UV-optical pseudo-bolometric luminosities of SN 2018gv is consistent with the peak value of SN 2011fe. Assuming SN 2018gv has the same NIR/optical flux ratio ($F_{\rm NIR}/F_{\rm Optical}$) as SN 2011fe, we estimate the peak bolometric luminosity of SN 2018gv to be $\log L$ = (43.074±0.023±0.008) erg s^{-1}. The first and the second uncertainties represent the statistical error and the error due to the distance, respectively. Following Stritzinger & Leibundgut (2005), the peak bolometric luminosity produced by the radioactive ^{56}Ni can be written as:

$$L_{\rm max} = (6.45{\rm e}^{-\frac{t_r}{8.8\ {\rm day}}} + 1.45{\rm e}^{-\frac{t_r}{111.3\ {\rm day}}})\left(\frac{M_{\rm Ni}}{M_\odot}\right) \times 10^{43}{\rm erg\ s^{-1}}, \quad (7)$$

where t_r is the rise time of the bolometric light curve, and $M_{\rm Ni}$ denotes the synthesized nickel mass in the SN ejecta. A high-order polynomial fit to the bolometric light curve from $t = -15$ to $+15$ days suggests that the bolometric luminosity peaked around $t = -1.1 \pm 2.4$ days relative to the $B-$band maximum. This is consistent with the mean of the distribution of the time difference between the bolometric light curve peak and the $B-$band maximum (see, e.g. Scalzo et al. 2014). Adopting a $B-$band rise time of 18.51±0.92 days estimated in Section 3.3 and peak luminosity of $L = (1.186 \pm 0.064 \pm 0.022) \times 10^{43}$erg s^{-1}, we derive a nickel mass of 0.56±0.08$M_\odot$ for SN 2018gv. This is also consistent to the estimation assuming a typical bolometric rise time of 19±3 days, i.e. $M_{\rm Ni} \approx 0.59 \pm 0.09 M_\odot$ according to the Arnett law (e.g. see Arnett 1982, and Equation 7 in Stritzinger & Leibundgut 2005). These results are consistent with the nickel mass derived based on the peak of the UVOIR luminosity of $L = 1.191 \times 10^{43}$erg s^{-1}.

Regarding the sanity test simultaneously performed on SN 2011fe, we noticed that the peak pseudo-bolometric luminosity of SN 2011fe derived over a wavelength range of 1660 − 8180 Å ($\log L$ = 43.011±0.016 erg s^{-1}) is systematically lower than the UVOIR bolometric luminosity calculated considering the SED over 1600 − 24000 Å ($\log L = 43.05$ erg s^{-1}, with a typical uncertainty of 0.07 dex, dominated by the uncertainty in the distance Zhang et al. 2016). This discrepancy of ∼8.6% in the peak bolometric luminosity is due to the construction of the pseudo-bolometric light curves because we do not account for the NIR fluxes. After correcting for the ∼9% $F_{\rm NIR}/F_{\rm Optical}$ ratio around the peak, the bolometric luminosity of SN 2011fe $\log L = 43.07$ erg s^{-1} is consistent with Zhang et al. (2016) and confirms the sanity of the method.

5. SPECTROPOLARIMETRY

Spectropolarimetry of SN 2018gv obtained at day −13.6 (epoch 1) and day −0.5 (epoch 2) relative to the $B-$band maximum light, together with the associated flux spectra in the rest frame, is shown in Figs. 14 and 15, respectively. Because of the low and decreasing level of the continuum polarization, the Stokes parameters measured at different wavelengths at the second epoch are overall close to zero, which leads the deduced position angle (PA) measured for interstellar-polarization (ISP)-subtracted data to display random orientations; therefore, we only show the PA calculated before ISP removal.

5.1. *Interstellar Polarization*

Light from SNe always suffers from the extinction caused by the interstellar dust grains along the line of sight, in both the Milky Way and their host galaxies. Dichroic extinction by partially aligned non-spherical paramagnetic interstellar dust grains will polarize the traversed photons, which causes the observed ISP. The removal of the ISP is essential to determine the intrinsic polarization of SNe.

An upper limit on the dichroic extinction-induced polarization by Milky Way-like dust grains yields $p_{\rm ISP}<9\times E(B-V)$ (Serkowski et al. 1975). Assuming both the Galactic and the SN 2018gv host dust follow a similar $R_V = 3.1$ extinction law (Cardelli et al. 1989), the upper limits on the ISP derived from the Milky Way and the host galaxy NGC 2525 reddenings (derived from the values listed in Table 4) yield $p_{\rm ISP}^{MW}<0.46\%$ and $p_{\rm ISP}^{Host}<0.20\%$, respectively.

Following a similar procedure to the spectropolarimetric analysis of SN 2012fr (Maund et al. 2013), we estimate the ISP towards SN 2018gv as $Q_{\rm ISP} = 0.07\% \pm 0.16\%$, $U_{\rm ISP} = -0.49\% \pm 0.09\%$. The corresponding degree and position angle are $p_{\rm ISP} = 0.50\% \pm 0.09\%$ and $PA_{\rm ISP} = 139\overset{\circ}{.}0 \pm 5\overset{\circ}{.}2$, respectively. Detailed information of the ISP estimation is reported in Appendix D. Notice that due to the relatively low ISP suggested by the low extinction towards SN 2018gv, we adopted a wavelength-independent ISP correction to the observations. Before the maximum luminosity, the presence of Fe absorption wings and its line-blanketing depolarization over the wavelength ranges $4800 - 5600$ Å may not be sufficient to characterize the true ISP. Therefore, we would like to stress that the ISP determination described here is only tentative. However, the ISP only resets the origin of the polarization on the $Q - U$ diagram, and should not alter the polarized spectral features. The consistent ISP estimates derived for the two epochs also suggest that the uncertainties in the ISP do not have a strong impact on the interpretation of the intrinsic polarization of SN 2018gv.

5.2. *The $Q - U$ Plane And The Dominant Axis*

Plotting the observed spectropolarimetry on the Stokes $Q-U$ plane provides an intuitive diagnostic for investigating the relative behavior of the Stokes parameters of the continuum and for different spectral features (Wang et al. 2001). In most of the cases, the observations indicate the roles of both axisymmetric and nonaxisymmetric components. In the latter case, axisymmetry may be broken by the presence of clumps of different composition, optical depth, and even different velocities. For an axially symmetric structure, the resulting polarization can be described by a single, straight line on the Stokes $Q - U$ plane, namely the 'dominant axis' (Wang et al. 2003b), i.e.

$$U = \alpha + \beta Q. \tag{8}$$

Recalling Equation 1, the slope of the line characterizes the PA, which is only related to the position angle of the symmetry axis on the sky. The distance to the origin gives the degree of polarization, which is determined by the scattering opacity of different elements.

The polarimetry can therefore be decomposed into two components relative to the dominant axis. Linear least-squares fitting to the polarimetry on the $Q-U$ plane can be used to determine the dominant axis (axis d). Such a dominant direction can sometimes be recognized through the distribution of the points in the $Q - U$ plane. Deviations from the dominant axis, in the perpendicular direction along the orthogonal axis (axis o), indicate departures from axial symmetry. This projection is equivalent to finding the first two Principal Components (P_d, P_o) of the data or applying a rotation to the $Q - U$ plane, i.e. see Equation 1−2 of Wang et al. (2003b) and Equation 2−3 of Stevance et al. (2017).

Figure 16 shows the ISP-corrected Stokes parameters on the Stokes $Q - U$ plane for both epochs. The determination of the dominant axis of SN 2018gv was conducted for both epochs, by performing an error-weighted linear least squares fitting to the data. In Fig. 16, the black long-dashed lines fit the dominant axis to the observed polarization in the wavelength range $4300 \leq \lambda \leq 9100$ Å, representing

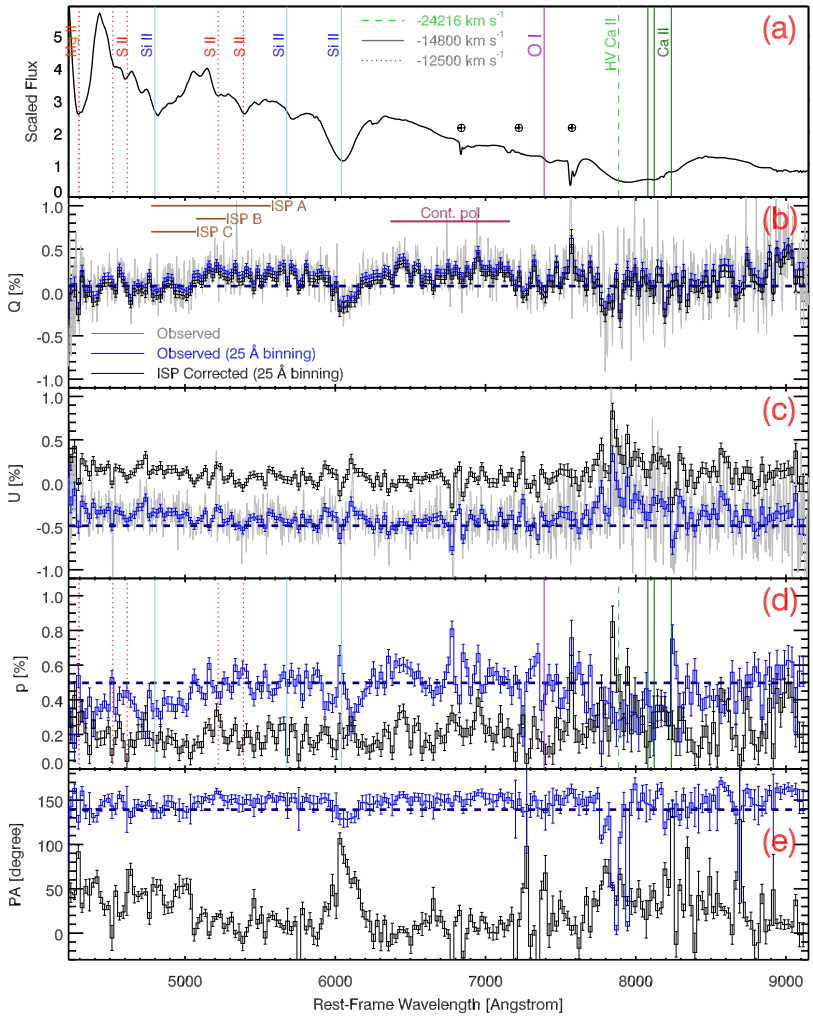

Figure 14. Spectropolarimetry of SN 2018gv at −13.6 day (epoch 1) relative to the $B-$band maximum light at MJD 58149.698. The five panels (from top to bottom) give (a) the scaled observed flux spectrum with Si II, Ca II, O I and Mg II lines labeled for different velocities; (b) the normalized Stokes parameter Q; (c) the normalized Stokes parameter U; (d) the polarization spectrum (p); and (e) the polarization position angle PA. Line identifications provided in the top panel. The diagrams in panels (b)-(e) represent the polarimetry before (blue) and after (black) the ISP correction. The Q and U components of the ISP and the corresponding p and PA are shown by the horizontal gray lines in panels (b)-(e), respectively. The data have been rebinned to 25 Å for clarity.

the direction of axial symmetry. The direction of the dominant axis changed from $PA = 168.^{\circ}9 \pm 1.^{\circ}2$ to $178.^{\circ}3 \pm 0.^{\circ}7$. We suggest that a dominant axis seems to be present at both epochs, and it is almost parallel to the U axis. Though the observations complied with a dominant axis, the large values of χ^2 as labeled on the lower-left corner of each panel indicate that the data are poorly described by just a linear relation. Large deviations on the $Q-U$ plane from the dominant axis indicate a significant departure from axial symmetry. In the classification scheme of Wang & Wheeler (2008), the spectropolarimetry of SN 2018gv is an example of spectropolarimetric (SP) Type D1. This type is characterized by data that show an elongated ellipsein a $Q-U$ diagram so that a dominant axis can

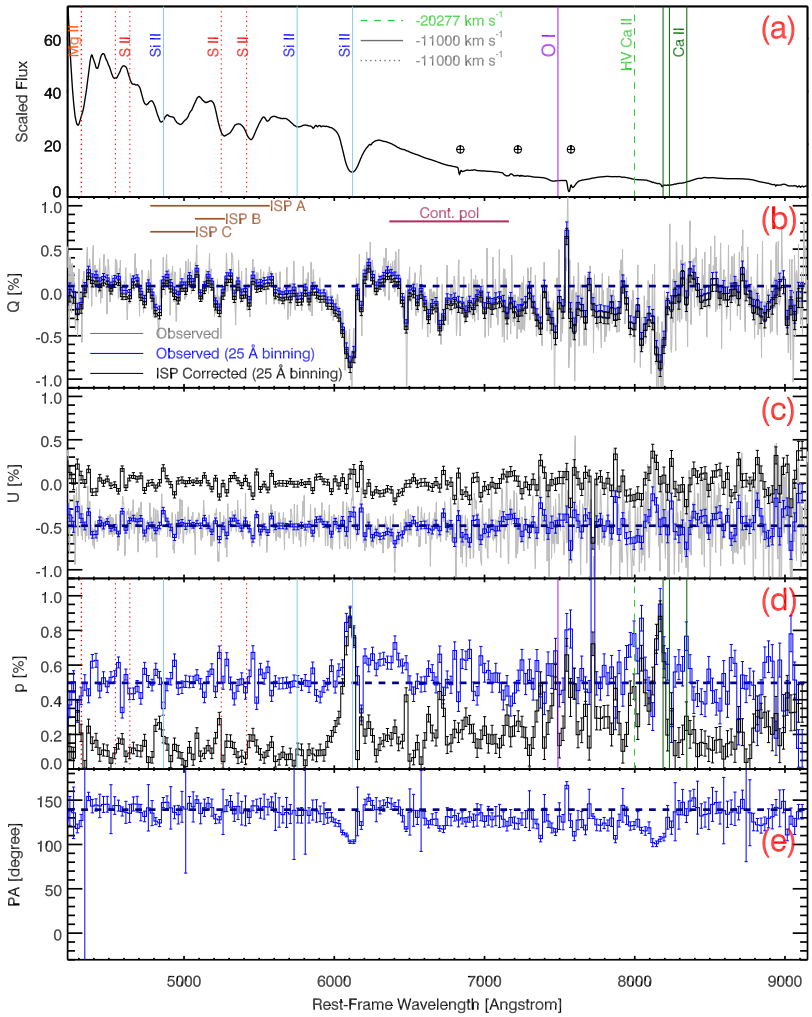

Figure 15. Same as Fig. 14, but for spectropolarimetry of SN 2018gv at −0.5 day (epoch 2). Because the intrinsic continuum polarization is very low around maximum brightness, the ISP-subtracted PA exhibits quasi-random values. Therefore, in panel (e), we only present the PA before the ISP-correction (blue).

be identified, but for which a straight line does not provide a satisfactory fit. Significant deviations are found orthogonal to the dominant axis.

5.3. *Continuum Polarization*

Linear polarization in the continuous spectrum is due to the Thomson scattering of free electrons, and it is independent of wavelength. After correcting for the ISP, the continuum polarization of SN 2018gv at the two epochs was estimated based on the Stokes parameters over the wavelength range 6400−7200 Å, which is known to be free of strongly polarized lines (Patat et al. 2009). Scattering in the degrees of polarization can still be seen within the selected polarized lines-free wavelength ranges which used to estimate the continuum polarization. Such fluctuation arises from the bound-bound transitions, primarily of iron-peak elements, which modify the emergent radiation by depolarizing the continuum flux and produce some line polarization (Hoeflich et al. 1996; Höflich et al. 2006). The error-weighted mean across this region at the two epochs gives $Q_{\rm Cont1} = 0.20\% \pm 0.08\%$, $U_{\rm Cont1} = 0.04\% \pm 0.09\%$, and $Q_{\rm Cont2} = -0.13\% \pm 0.13\%$, $U_{\rm Cont2} = -0.04\% \pm 0.09\%$, respectively. The error

has been estimated by adding the statistical uncertainties and the standard deviation calculated from the 25Å binned spectra within the continuum wavelength range in quadrature. At epoch 1, the level of continuum polarization of SN 2018gv is consistent with the low levels of continuum polarization measured from Type Ia SNe at early epochs, i.e. $0.06\% \pm 0.12\%$ at day -11 for SN 2012fr (Maund et al. 2013), and $\sim 0.3\%$ at -9.1 day for SN 2016coj without the removal of ISP (Zheng et al. 2017). At epoch 2, a difference of $\Delta Q_{\rm Cont} = -0.33\% \pm 0.15\%$ and $\Delta U_{\rm Cont} = -0.08\% \pm 0.13\%$ can be identified. This marks the time-evolution of the degree and the position angle of the continuum polarization, i.e. from $p_{\rm Cont1} = 0.20\% \pm 0.08\%$, and $PA_{\rm Cont1} = 4.^{\circ}8 \pm 11.^{\circ}3$, to $p_{\rm Cont2} = 0.14\% \pm 0.13\%$ and $PA_{\rm Cont2} = -82.^{\circ}4 \pm 27.^{\circ}2$, respectively. At both epochs, the measured degrees of continuum polarization are consistent with the low levels typically measured for Type Ia SNe (Wang & Wheeler 2008), indicating an approximately spherical symmetry.

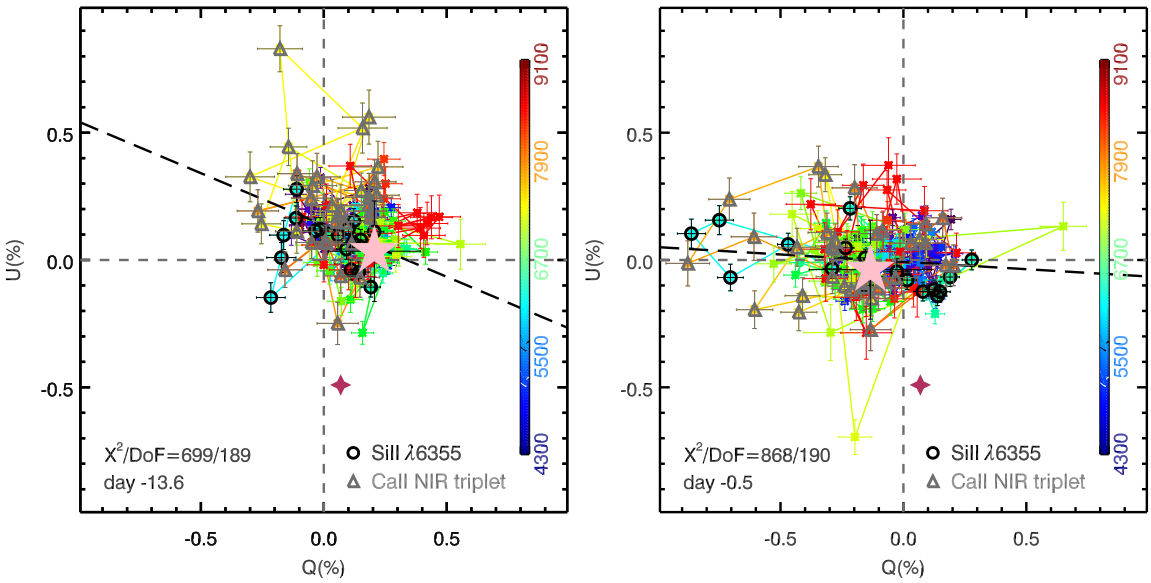

Figure 16. The ISP-corrected Stokes parameters of SN 2018gv, on the Stokes $Q-U$ plane. The data have been rebinned to 25 Å. In each panel, the color bar indicates the wavelength and the filled maroon star shows the position of the estimated ISP. The black line traces the dominant axis computed using the data in a wavelength range $4300 \leq \lambda \leq 9100$ Å. The solid pink $\star$ in each panel indicates the deduced continuum polarization over the wavelength range $6400 - 7200$ Å. The open black circles and the open gray triangles mark the spectral regions covering the Si II λ6355 and the Ca II NIR3 features, respectively.

5.4. *Line Polarization*

In addition to the wavelength independent continuum polarization arising from a globally axisymmetric ejecta, we observe wavelength dependent polarization features associated with spectral lines at both epochs in association with spectral lines identified in the Stokes I flux spectrum. This indicates a departure from axisymmetry. The most likely interpretation of line polarization in the context of Type Ia SNe gives that the underlying electron-scattering photosphere is covered by certain element-rich clumps with high optical depth. These indicate additional asymmetries, that are dependent on the chemical composition, ionization, and velocity structure of the ejecta, exterior to the photosphere. Different elements may have different electron scattering opacities as well as different geometric dis-

tributions. Polarimetry measures the degree of incomplete cancellation of photon 'E-vectors' as the photons interact with line-transitions in, possibly, asymmetrically-distributed material.

For prominent, broad lines, the polarization profile over wavelength probes the structure of the ejecta in velocity space. For complex structures, which depart from a simple axial symmetry, the resulting polarization across the wavelengths associated with particular spectral features, may deviate from the straight line which is the tracer of axial deviation from spherical symmetry (Wang & Wheeler 2008). The presence of asymmetric structures in the ejecta can be inferred from the observation of loops in the $Q-U$ plane. Such loops are defined as a gradual rotation of the PA as a function of observed wavelength across a spectral line. The SN with loops across spectral lines on the $Q-U$ diagram were assigned SP Type L in Wang & Wheeler (2008). The presence of one or more loops across a specific spectral feature indicates a significant variation in the degree of polarization and the polarization position angle at different velocities (corresponding to different depths into the ejecta; Wang & Wheeler 2008).

5.4.1. Si II Lines

At −13.6 day, the peak around 5900−6200 Å in Q and the troughs at similar wavelengths in the U spectrum can be attributed to the Si II λ6355 line at $v \sim -14{,}000$ km s^{-1} (see Fig. 14). After correcting for the ISP, the degree of polarization across this line did not show any distinguishable features in p (see the black line in Fig. 14d), but exhibited a difference of $\sim$ 90 degrees in PA compared to the continuum (see Fig. 14e). Such a pattern in the PA over the Si II λ6355 feature indicates that the Si-rich portion of the ejecta is likely to be oriented perpendicular to the principal axis of symmetry of the total ejecta. The line profile at ∼4810 Å can be identified as the blue-shifted Si II $\lambda\lambda$5041, 5056 doublet which has a similar velocity to Si II λ6355; however, the feature is also blended with a series of iron lines, i.e. Fe II λ4913, 5018, 5169. At −0.5 day, the polarization peak around Si II λ6355 occurs at ∼6100 Å. The central velocity of the feature is measured as $\sim -11{,}000$ km s^{-1}. The polarization is the highest at the absorption minimum of this feature. The polarization profile is asymmetric with a sharp drop towards lower velocities.

5.4.2. Ca II NIR Triplet

At −13.6 day troughs in q and peaks in u are also seen between 7800 and 8300 Å (see Fig. 14). Though the observed line profiles of Ca II NIR3 at early phases can be well fit by a double Gaussian function describing a normal and HV components with separate central wavelengths, the polarization spectra (with low levels of S/N) do not exhibit separate features for the HV and photospheric velocity components. One can still identify a 'notch' around 7800−7900 Å in Q accompanied by a 'peak' at a similar wavelength in U. These features are associated with the HV Ca II NIR3 at $\sim -24{,}200$ km s^{-1}. Less obvious features can be seen within the wavelength region of 8000−8300 Å. These features have velocities similar to that inferred for the photosphere from the Si II λ6355 at $\sim -14{,}000$ km s^{-1} and also deviate from the overall spectral ranges in p and PA. After correcting for the ISP, the PA across the Ca II NIR3 shows different values compared to either that of the continuum or the Si II λ6355, indicating the configuration of the Ca-rich ejecta is not identical to the Si II λ6355 line forming regions and distinct from the photosphere as well. At −0.5 days, the Ca II NIR3 is dominated by the photospheric component at $\sim -11{,}500$ km s^{-1}. The HV component is still discernible and located at $\sim -20{,}200$ km s^{-1}. The polarization behaviors over the HV regions and the photosphere do not show distinct variation.

5.4.3. Mg II λ4481, Si II λ5041, Si II λ5454, 5640 and O I λ7774 Lines

Despite approaching the blue end of spectral coverage, a ∼0.3% polarization can be marginally identified with the line of Mg II λ4481 after ISP-correction (see Fig. 14d). Si II λ5041 does not exhibit clear polarization, but the PA across Si II λ5041 and Mg II λ4481 are both larger compared to the PA from 5100−7200 Å, except for the Si II λ6355 and telluric features (see Fig. 14e). This suggests some commonality in their geometry. Same interpretation also holds for epoch 2, in which Mg II λ4481 and Si II λ5041 polarized at ∼0.3−0.4%. At all epochs, the distinctive 'W'-shaped S II (λ5454, 5640) absorption features appear at lower velocities compared to the velocity derived from the Si II λ6355 line. For instance, from epoch 1 to epoch 2, the S II λ5454, 5640 velocities evolve from −13,800 km s^{-1} and −13,500 km s^{-1} to −10,100 km s^{-1} and −10,400 km s^{-1}, respectively. The slower velocities measured for S II λ5454, 5640 are due to this feature being optically thin at larger radii compared to Si II and Ca II. This is corroborated by the consistent low polarization measured across this feature, which suggests that sulfur is more concentrated in lower-velocity regions than calcium and silicon. Additionally, we find that the O I λ7774 line appears to be weak in the flux spectrum, and no sign of that feature can be identified in the polarization spectrum. The primordial oxygen from the WD maintains its initial spherically symmetric distribution despite the asymmetric explosion. This gives an important constraint on the explosion models (Höflich et al. 2006).

5.5. *The Inferred Ejecta Geometry*

Following from Section 5.2, we present the dominant and the orthogonal polarization components after correcting for ISP in Fig. 17. The dominant component, that is, the polarization projected onto the dominant axis, represents global geometric deviations from spherical symmetry. Any polarization signal orthogonal to the dominant axis carries information about deviations from axial symmetry. In Fig. 18, we show the loops across the Si II λ 6355 and Ca II NIR3 features. At epoch 1, the polarization modulations associated with Si II λ6355 are principally observed in the dominant polarization component P_d (i.e. the middle-left panel in Fig. 17). In the orthogonal polarization component (see bottom left panel in Fig. 17) a narrow polarization profile can be identified at the wavelength coincident with the position of the absorption minima of Si II λ6355. Such a residual indicates that the bulk orientation of Si-rich ejecta is different from that of the dominant axis of the photosphere (as inferred from the continuum polarization). A line complex can be observed in the polarization modulations associated with Ca II NIR3. The HV component shows modulation in both the dominant and the orthogonal polarization components. The NV component, however, exhibits significantly less modulation in both the dominant and orthogonal components.

At epoch 2, the polarization modulations associated with Si II λ6355 and Ca II NIR3 both fall predominantly along the P_d axis. The signal in the orthogonal polarization component, over the observed wavelength range is consistent with the expected level of uncertainty. The rotation of the PA over Si II λ6355 (i.e see Fig. 18) can be interpreted as the rotation of the principal axis of symmetry with depth into the ejecta. The HV component of Ca II NIR3 has become significantly shallower by epoch 2. Due to insufficient S/N, it is unclear if the HV Ca II NIR3 component carries the same axial asymmetry as other lines. The polarization signal associated with Ca II NIR3 is dominated by the NV component. Moreover, the PA of the Ca II NIR3 are almost aligned with the Si II λ6355 at epoch 2, suggesting that the line-forming regions of silicon and calcium have already settled to a relatively similar geometric configuration.

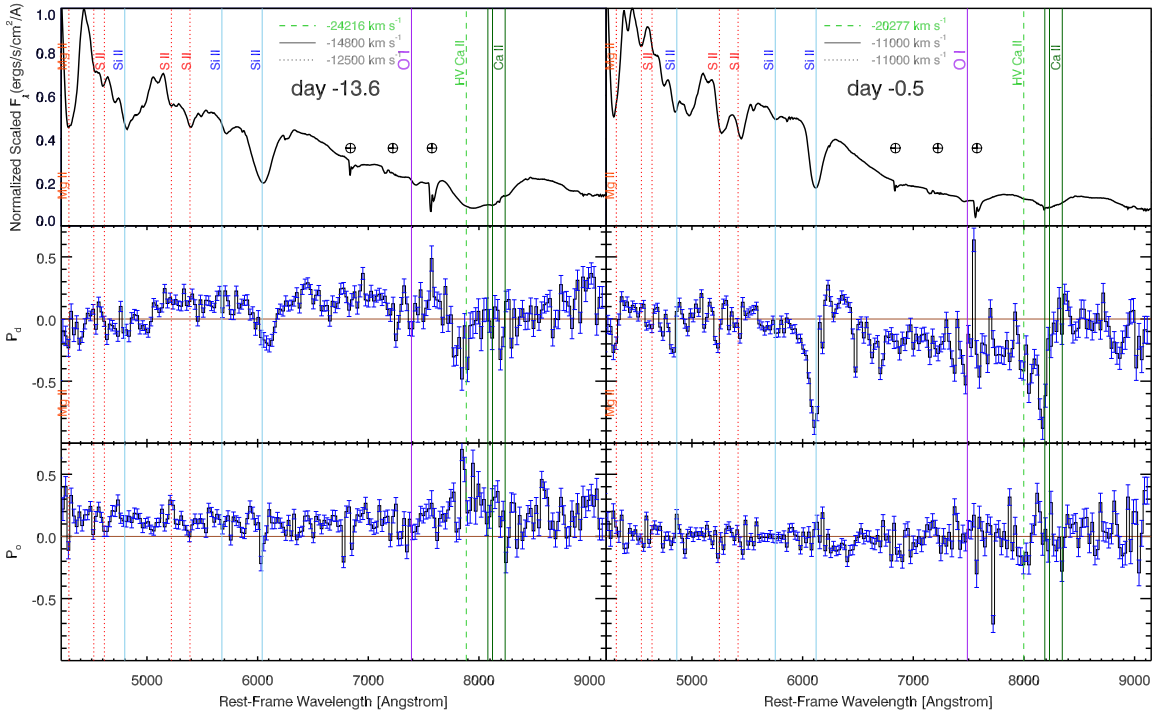

Figure 17. The normalized flux spectra together with the PCA of SN 2018gv spectropolarimetry at −13.6 day (epoch 1, left panels) and −0.5 day (epoch 2, right panels). The top row gives the flux spectra normalized to the maximum value within the range. The middle and the bottom rows illustrate the polarization spectra projected onto the dominant axis and the orthogonal axis, respectively. The vertical solid lines mark the positions of certain spectral features at different velocities as labeled in the figure. Some major tellurics are labeled by ⊕. At −13.6 day, the Si II λ6355 and the Ca II NIR3 features exhibit similar but not identical deviations from the dominant axis, suggesting that the geometrical structures of Si II, Ca II and the photosphere are different. No polarization is detected across other weaker lines. At −0.5 day as shown by the right panels, the Si II λ6355 and the Ca II NIR3 features appear to have the same dominant axis. Over the wavelength range 6400−7200 Åcharacterizing the continuum polarization, the error-weighted mean of P_O has evolved from 0.109%±0.095% to −0.044%±0.089% from −13.6 to −0.5 days, indicating a more spherically symmetric geometrical structure of the inner ejecta. Notice that the two epochs are characterized by different position angles of the dominant axis and therefore do not share the same orientation of the photosphere.

In epochs 1 and 2 (see Fig. 18), the Si II λ6355 and the Ca II NIR3 both exhibit loops in the $Q-U$ space. In epoch 1, linear fittings of Stokes $Q-U$ data points across each line suggest that the Si-rich and the Ca-rich regions reside in different positions of the ejecta, which are also incompatible with the global geometry indicated by fitting all the data points across the entire observed wavelength. In epoch 2, the data points across the Si-rich and the Ca-rich ejecta tend to fall along a single locus. The orientation of these ejecta is also consistent with the overall shape of the ejecta.

The geometry of the Si-rich and the Ca-rich ejecta can also be visualized in polar plots (e.g. see Maund et al. 2009; Reilly et al. 2016; Hoeflich et al. 2017; Stevance et al. 2019). Such plots present the position angles measured for selected spectral features at different radial velocities in polar coordinates. In Fig. 19 we show polar plots for the Si II λ6355 and the Ca II NIR3 profiles at both epochs. At epoch 1 (−13.6 day, left panel), the large offset in the radial profile of Si II λ6355 (shown in blue)

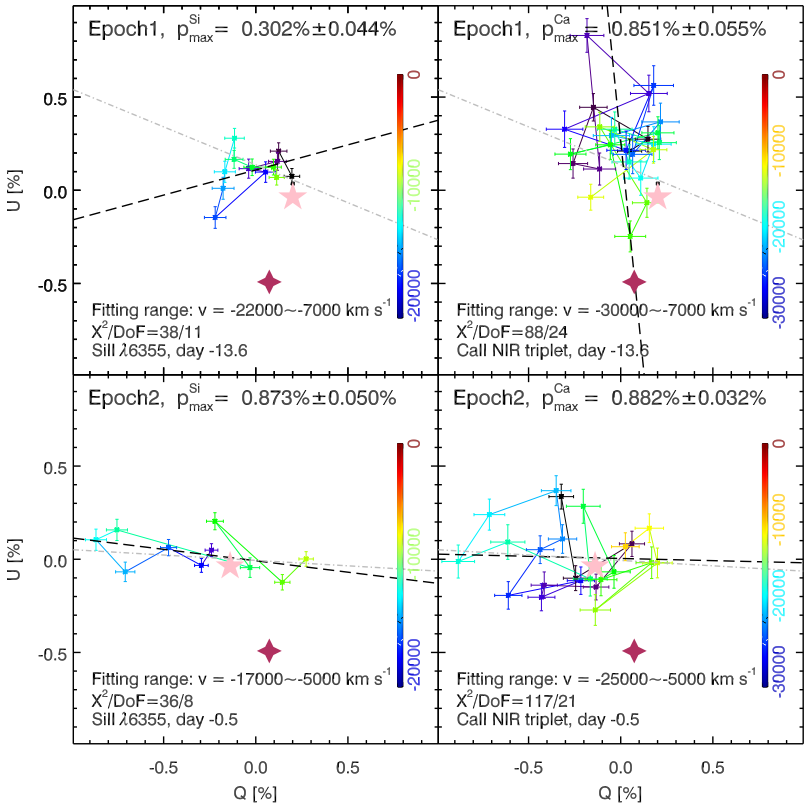

Figure 18. The polarization for the Si II λ6355 (left panels) and the Ca II NIR3 (right panels) features on the Stokes $Q-U$ plane at −13.6 day and −0.5 day. The data have been rebinned to 25 Å. In each panel, the points are color coded according to the velocity relative to the respective wavelengths measured in the rest frame for the two features. The data were corrected for the ISP (the location of which is indicated by the filled maroon star) and the continuum polarization is shown by the solid pink ⋆. The maximum polarization across the feature after ISP-correction is also presented. The dashed black line fits the displayed data points and the dotted gray line traces the dominant axis computed in the wavelength range $4300 \leq \lambda \leq 9100$ Å.

compared to the total ejecta (the gray sector) confirms the large deviations from the dominant axis of the continuum polarization. The even more erratic radial profile of the Ca-rich component also indicates a complex structure of the line forming regions. At epoch 2 (−0.5 day, right panel), the change in the position angle of the continuum polarization (see Section 5.3) can be seen as the rotation of the gray-shaded sector. The radial profiles of both the Si-rich and the Ca-rich components have settled to a similar orientation as the total ejecta indicated by the gray sector.

6. DISCUSSION OF THE SPECTROPOLARIMETRY OBSERVATIONS

6.1. *The Si II λ6355 Polarization Compared with a Larger Sample*

First, we notice that the polarization of Si II on the $Q-U$ diagram can be well fitted by a straight line (e.g. see the right panel of Fig. 16 and the lower-left panel of Fig. 18). With a clearly defined dominate axis, SN 2018gv would thus be classified as SP Type D0 Wang & Wheeler (2008). Such significantly polarized Si II feature is suggestive of a global asymmetry of silicon layer.

The peak polarization across the Si II λ6355 line evolves with time. In order to compare with different SNe at similar phases, Wang et al. (2007) fitted the data with a second order polynomial

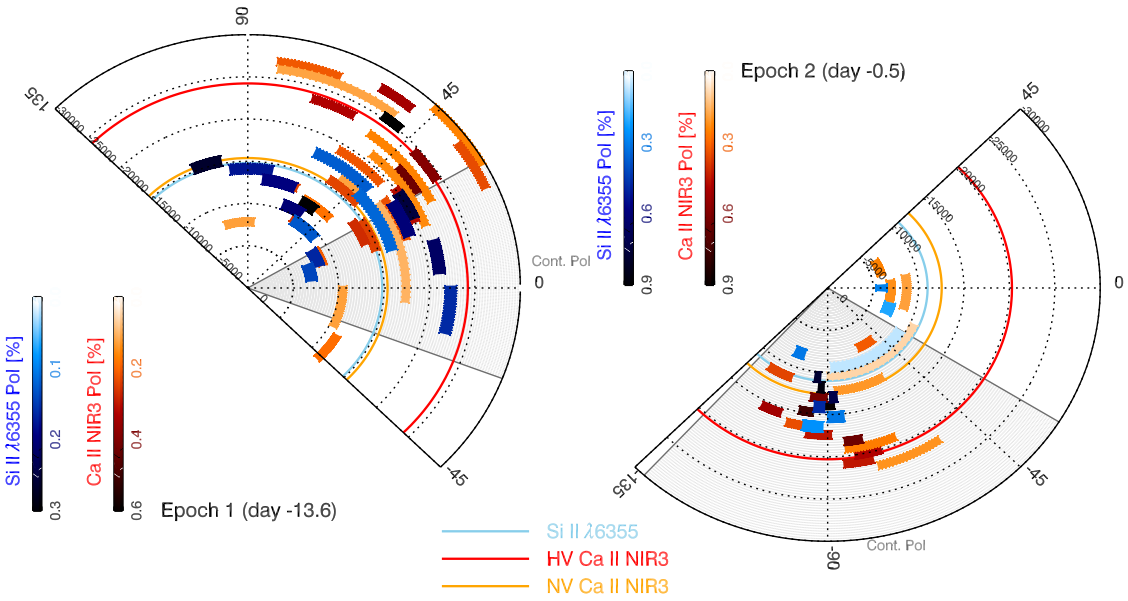

Figure 19. Polar plots of SN 2018gv showing the velocity and polarization angle across the profiles for Si II λ6355 and Ca II NIR3 as a function of radial velocity. In each panel, the color bars indicate the ISP-corrected polarization degrees with the continuum polarization not subtracted. The numbers along the radial and position angle are labeled in km s^{-1} and in degrees, respectively. The data have been rebinned to 25 Å for better visualization. The center and the angular extent of each colored-bin represent the average PA and the associated error, respectively. Note that larger angular extent suggests greater uncertainty on the PA. The continuum polarization angle is shown in grey, and its angular extent indicates the 1-σ uncertainty. Typical uncertainties in the data points are smaller in epoch 2 compared with epoch 1 due to higher S/N. Velocities measured at the minima of the flux spectra of each species are indicated by colored semicircles as labeled.

to describe the time dependence of the degree of the Si II polarization: $p_{\rm SiII}(t) = 0.65 - 0.041(t - 5) - 0.013(t + 5)^2$. Here t denotes the time (in days) after the $B-$band maximum light and $p_{\rm SiII}(t)$ gives the measured polarization (in percent) of Si II λ6355. Wang et al. (2007) derived a correlation between the maximum line polarization of Si II λ6355 and $\Delta m_{15}(B)$:

$$p_{\rm SiII}^{corr-5} = 0.48(03) + 1.33(15)(\Delta m_{15} - 1.1), \quad (9)$$

where $p_{\rm SiII}^{corr-5}$ is defined as the polarization of the Si II λ6355 corrected to -5 day in a unit of percent. This correlation indicates that at a given epoch, dimmer SNe exhibit higher Si line polarization, hence higher chemical nonuniformity. This can be understood if the dimmer the SN, the less material was burnt. Such a incomplete burning is not sufficient to erase chemically-lumpy configurations. The quantity $p_{\rm SiII}^{corr-5}$ can be obtained by applying the correction given by Wang et al. (2007):

$$P_{\rm SiII}(t) = P_{\rm SiII}^{corr-5} - 0.041(t - 5) - 0.013(t + 5)^2; \quad (10)$$

For SN 2018gv, adopting $p_{\rm SiII}(t) = 0.87\% \pm 0.05\%$ at $t = -0.5$ day gives $p_{\rm SiII}^{corr-5} = 0.91\% \pm 0.05\%$. This is significantly larger than the typical 1-σ upper range of polarization shown as Fig. 2 of Wang et al. (2007).

Such a big discrepancy does not necessarily mean that SN 2018gv has a peculiar Si II λ6355 polarization because the empirical relationship proposed by Wang et al. (2007) does not account for the

considerable intrinsic polarization variations from SN to SN. The high degree of polarization observed for SN 2018gv suggests that the presence of large scale departure from spherical symmetry. Cikota et al. (2019, ApJS accepted) re-analyzed this relationship using a larger sample of 35 Type Ia SNe and found a significantly larger scatter. The observed degree of silicon polarization of SN 2018gv at -0.5 days falls in the $\sim$0.1%$-$1.7% range determined from a larger sample. Future high-precision spectropolarimetry of more Type Ia SNe with complete coverage of the rising phase is essential to determine the commonality and probe the intrinsic diversity in the geometric structure of the ejecta.

According to Maund et al. (2010), the peak polarization degree of the Si II λ6355 line at -5 day is correlated with the average daily decline rate of the expansion velocity measured from the same line:

$$P_{\rm SiII}^{corr-5} = 0.267 + 0.006 \times \dot{v}_{\rm SiII}. \quad (11)$$

The velocity gradients were derived based on the measurements taken between maximum and approximately two weeks after, when the Si II feature disappears (Benetti et al. 2005), while the corrected day -5 Si II polarizations were obtained based on Equation 10. Adopting the velocity gradient of SN 2018gv around the peak or between days 0 to +10, i.e. $\dot{v}_{\rm SiII} = 36.6 \pm 6.4$ km s^{-1} or 34.3 km s^{-1}, the estimated polarization gives $p_{\rm SiII} = 0.49\% \pm 0.04\%$ or 0.47%, respectively. These values are lower compared to the determined $p_{\rm SiII}^{corr-5}$.

Cikota et al. (2019) explored the possible correlations among the polarimetric and other observational properties of Type Ia SNe. Based on an archival data sample of 23 SNe that have at least one observation between day -11.0 and day 1.0, they found a strong linear correlation between the Si II λ6355 polarization and the expansion velocity traced by the same line:

$$P_{\rm SiII} = (6.40 \pm 1.28) \times 10^{-5} \times v_{\rm SiII@-5d} - (0.484 \pm 0.147), \quad (12)$$

where $p_{\rm SiII}$ is the maximum polarization of the Si II λ6355 line between day -11 and +1, and $v_{\rm SiII@-5d}$ gives the velocity measured from the Si II λ6355 profile at -5 days relative to the $B-$band peak brightness. Adopting an interpolated $v_{\rm SiII@-5d} = -11{,}300$ km s^{-1} at day -5 and a typical uncertainty of 27 km s^{-1}, Equation 12 yields a maximum Si II λ6355 polarization of 0.24%$\pm$0.21%. Therefore, we conclude that SN 2018gv is consistent with the Si II velocity-polarization relationship at day -13.6 ($p_{\rm SiII} = 0.30\% \pm 0.04\%$), but exhibits a significantly higher Si II λ6355 polarization at day -0.5 ($p_{\rm SiII} = 0.87\% \pm 0.05\%$).

6.2. *The Asymmetric Polarization Profile of Si II λ6355*

We notice that the most prominent Si II λ6355 feature in the polarization spectrum around the $B-$maximum exhibits an asymmetric profile. Fig. 20 portrys the polarization profiles of Si II λ6355 and Ca II NIR3 at day -0.5 with an 8Å bin size. In Fig. 20-d1, one can see that the polarization signal across the Si II λ6355 feature declines gradually from the absorption minimum in the flux spectrum towards shorter wavelengths. In contrast, the polarization profile exhibits a sharp drop from its peak towards longer wavelengths. We roughly estimated the blue side of the wing ranges from 5950$-$6120 Å, and the red side covers 6120 $-$ 6170 Å, corresponding to $-19{,}100$ to $-11{,}100$ km s^{-1} and $-11{,}100$ to -8700 km s^{-1} in velocity space, respectively. Considering the Si II λ6355 velocity measured from the same spectrum as $-10{,}984\pm345$ km s^{-1}, the velocity range measured from the polarized spectrum gives -8100 to +2400 km s^{-1} relative to the SN photosphere velocity traced by the same line. Such an asymmetric profile was not identified at epoch 1. The Ca II NIR3 displays a

complex polarization profile. At epoch 2, a weaker separate peak over ∼8020−8080 Å (see Fig. 20-d2) can be identified between the HV and NV Ca components, corresponding to a radial velocity of $\sim -18{,}000$ km s^{-1}. Without a finer temporal sampling of the spectropolarimetric evolution, it is not clear whether this component could be the analog of the asymmetry observed in Si II λ6355.

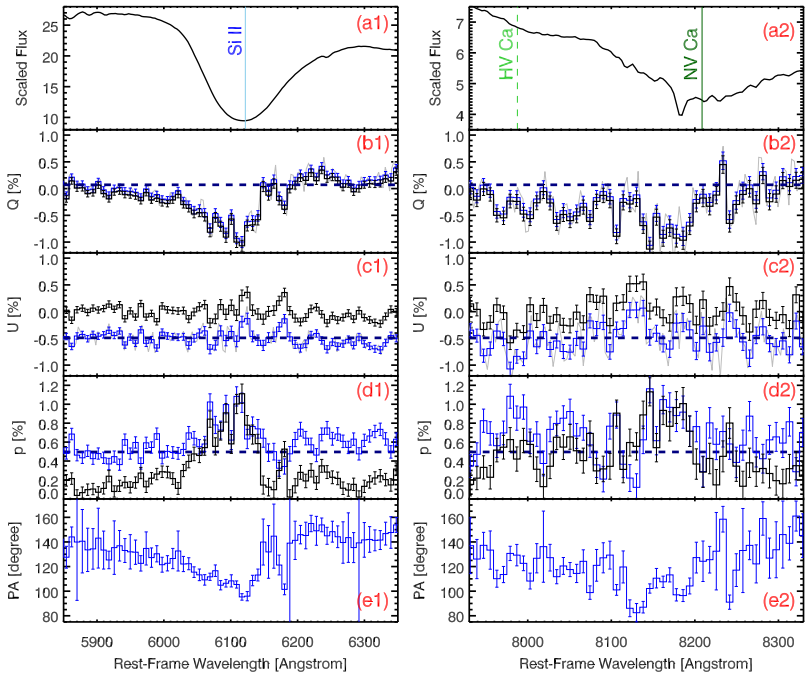

Figure 20. Same as Fig. 15, but on the spectroplarimetry of SN 2018gv across Si II λ6355 (the left panels) and the Ca II NIR3 (the right panels) at day −0.5 (epoch 2). The data have been rebinned to 8 Å . In the left panels, i.e. d1, the Si II polarization declines much faster from its peak around ∼6200 Å ($v \sim -11{,}000$ km s^{-1}) towards longer wavelengths compared to shorter wavelengths. Multiple peaks around ∼6100 Å may indicate the presence of various Si-rich components, which were not identified in the flux spectrum.

Around maximum light, the broad and symmetric flux profile across the Si II λ6355 feature suggests the absence of a distinct chemical 'boundary layer' at any drastically different velocities. Therefore, the sharp cut-off in the corresponding polarization profile at the low-velocity end can be attributed to the presence of a separate Si-rich component at a slightly higher velocity. It may be indicative of Si-rich matter at lower velocity and with similar geometry as the Thomson-scattering photosphere. The apparent asymmetry of the HV components of the Si-rich ejecta is consistent with an off-center delayed detonation. Such an asymmetric explosion would compress the core more significantly towards the direction away from the center, therefore pushing the intermediate mass elements and developing the asymmetric HV components (i.e. see Section 4.3 of Fink et al. 2010 and Fig. 1 of Bulla et al. 2016b). The absence of a similar structure at the first epoch would imply that the asymmetry becomes visible as more inner parts of the WD are exposed. This seems consistent with an off-center delayed detonation.

We suggest that the width of the wing towards the lower velocities characterizes the scale height of the Si-rich ejecta above the photosphere. Such an asymmetric polarization profile may not necessarily be a ubiquitous phenomenon since ignition of detonation at small off-center distances would lead to a relatively uniform distribution of silicon (see Höflich et al. 2002, 2006). A slightly off-centered det-

onation leads to a relatively uniform distribution of the elements synthesized near the central region. The velocity spread is, therefore, smaller so that there would be no splitting into NV and HV components of Si II λ6355. This is in agreement with the study based on larger samples (Silverman et al. 2015). For example, HV features of Si II λ6355 are seen in only ∼one-third of the Type Ia SNe even at early times ($t< -5$ days). Such HV features tend to appear at the earliest phases and in objects with large photospheric velocities (Silverman et al. 2015). By contrast, HV features of Ca II NIR3 are observed in ∼91% of the Type Ia SNe with spectra obtained earlier than day −4 (Silverman et al. 2015). Spectropolarimetry of a solid sample would deliver an alternative method of identifying and resolving the different components in the ejecta, which often are ambiguous in flux spectra. At earlier phases, the absence of such asymmetry would suggest that the Si-rich ejecta are well above the photosphere. A gradually-changing polarization profile towards the higher velocities may imply that the outer part of the Si-rich ejecta has already developed a diffuse structure above the photosphere. If indeed the polarized Ca-rich component at ∼8020−8080 Å (∼ −18,000 km s^{-1}) is related to the asymmetric polarization profile of Si II λ6355, it could be interperated as a HV Ca-rich layer in the ejecta formed further out relative to the Si-rich layers. This is corroborated by the higher velocities measured across the NV Ca II NIR3 feature.

6.3. *Implications of the Polarization and Different Models*

We compare the polarization of SN 2018gv to simulations by Bulla et al. (2016a,b), who calculated polarization spectra for different Type Ia SN explosion models at various equatorial viewing angles, and off-center delayed-detonation models with various off-center points for a delayed detonation model for a normal-bright SNe (Höflich et al. 2006). The low continuum and line polarizations as early as day −13.6 contradicts the high polarization levels of violent merger models (Pakmor et al. 2012; Bulla et al. 2016a). The observed low continuum, the moderate levels of Si II and Ca II NIR3 line polarizations, and the low polarization of O I λ7774 lead us to consider that SN 2018gv is broadly consistent with the overall geometric properties predicted by off-centered delayed-detonation models (i.e. Seitenzahl et al. 2013; Bulla et al. 2016b) and sub-$M_{\rm Ch}$ double-detonation models (i.e. Fink et al. 2010; Bulla et al. 2016b).

Regardless of the presence of HV Si II wing which is unresolved in the flux spectra, the observed pre- and near-maximum light polarization properties of SN 2018gv are similar to those of other normal Type Ia SNe, i.e. SNe 1996X (Wang et al. 1997), 2001el (Wang et al. 2003b), 2004dt (Wang et al. 2006), 2006X (Patat et al. 2009), 2011fe (Milne et al. 2017), 2012fr (Maund et al. 2013), 2014J (Porter et al. 2016), and 2016coj (Zheng et al. 2017). Kasen et al. (2003) presented models of SN 2001el and provided a comprehensive parametrization for several possible configurations of the HV Ca II loop. The complex Ca II loop profile observed from SN 2018gv could be interpreted as multiple clumped shells, or a superposition of multiple clumped shells with a characteristic ellipsoidal shell. More work is needed to account for the formation of such a complex HV polarization feature and its different orientation from the photosphere.

Additionally, comparing SN 2018gv to the simulations of Bulla et al. (2016b), we infer that the relatively high line polarization of SN 2018gv around the peak (i.e. ∼0.87±0.05%) does not favor a large number of ignition kernels in delayed-detonation models (Seitenzahl et al. 2013). A large number of ignition kernels (i.e. N>100) would lead to a more symmetric distribution of intermediate-mass elements and thus produce a generally lower degree of line polarization. More theoretical modeling is needed to account for the HV features observed in Si II λ6355 and Ca II NIR3 lines and

to investigate the shape and time-evolution of the flux and polarized spectra (Mulligan & Wheeler 2018).

In the following and guided by the flux spectra, we discuss the polarization characteristics of SN 2018gv in terms of off-center delayed detonations (Höflich et al. 2006) which are based on spherical delayed detonation models for the deflagration phase (Hoeflich et al. 2017). In addition, we perturb the underlying structure to use the observed polarization to identify and quantify the underlying aspherical components, namely asymmetry in density and abundances. The treatment of the asymmetries as perturbation is justified because, overall, they are small. We use spherical models as baseline because they suppress deflagration mixing, a requirement from the discussion above and many observations from the (Höflich & Stein 2002; Fesen et al. 2007; Diamond et al. 2015), and references therein. Possible reasons may include the effect of high-magnetic fields as indicated by late-time light curves, near mid-IR spectra (Penney & Hoeflich 2014; Remming & Khokhlov 2014; Hristov et al. 2018). We choose deflagration to detonation transition (DDT) models for normal-bright Type Ia SNe because the photometric characteristics of SN 2018gv are very similar to the observations of the light curves, color curves and color-magnitude diagrams as shown and as discussed in Section 3. As baseline-model we use model 27 with the velocity, density and abundance distribution given in Figures 1 and 2 of Hoeflich et al. (2017). Model 27 has a rise time of 18.8 d and $\Delta m_{15}(B/V) = 0.62/0.98$ mag compared to 18.51 ± 0.92 day and 0.63/0.96 mag of SN 2018gv.

In Fig. 21, we show the mass above the photosphere as a function of time, and the corresponding density slope n for $\rho \propto r^{-n}$ of the delayed detonation model cited above. Note that the overall structures are rather similar for a wide range of models including sub-$M_{\rm Ch}$ but the mass fraction scales with the total mass.

As discussed in previous sections, SN 2018gv shows many characteristics of model 27: a) We see little C II and O I early on corresponding to the outer layers at $\approx 5 \times 10^{-3} M_\odot$; b) line wings of Si II λ6355 extends to the very outer layers, i.e. >23,000 km s^{-1}, and evolves smoothly with time which starts at about $3 \times 10^{-3} M_\odot$ in the wings, and the Si II line extends down to about 0.3 to 0.4 $M_\odot$ from the outside. We note that this early start and such a large, continuous range for Si is barely compatible with double-detonations of a sub-$M_{\rm Ch}$ mass WD which would require at least 2×10^{-2} and $3 \times 10^{-3} M_\odot$ for a WD with 0.6 and $1.2 M_\odot$, respectively (Shen & Moore 2014). The long, logarithmic decline of the Si abundances till close to the surface is inherent to detonations going through C/O matter in $M_{\rm Ch}$ mass models. It also leads to the inverted triangular shaped Si line-wings ($\triangledown$) visible till about -13.2 day in Fig. 8 corresponding to a photospheric velocity of ≈15,000 km s^{-1} which, in the model, marks the transition to the Si/S dominated layers in the envelope. A linear line wing is a consequence of the logarithmic decline of the Si abundance in combination of low optical depth (Quimby et al. 2007).

Based on the delayed-detonation model, we want to discuss the polarization of SN 2018gv in terms of parameterized asphericity. Polarization can be formed by i) aspherical density distributions (van de Hulst 1957; Höflich 1991); ii) partial obscuration of the underlying Thomson-scattering dominated photosphere by line-absorption (Kasen et al. 2006; Höflich et al. 2006), and iii) off-center energy sources (Chugai 1992; Hoeflich et al. 1995). SN 2018gv does not show a flip in the polarization angle and, thus, this case is not applicable.

We first want to consider asymmetric chemical distributions produced by off-center DDT models in which the axis of chemical asymmetry is given by the center of the density distribution and the point

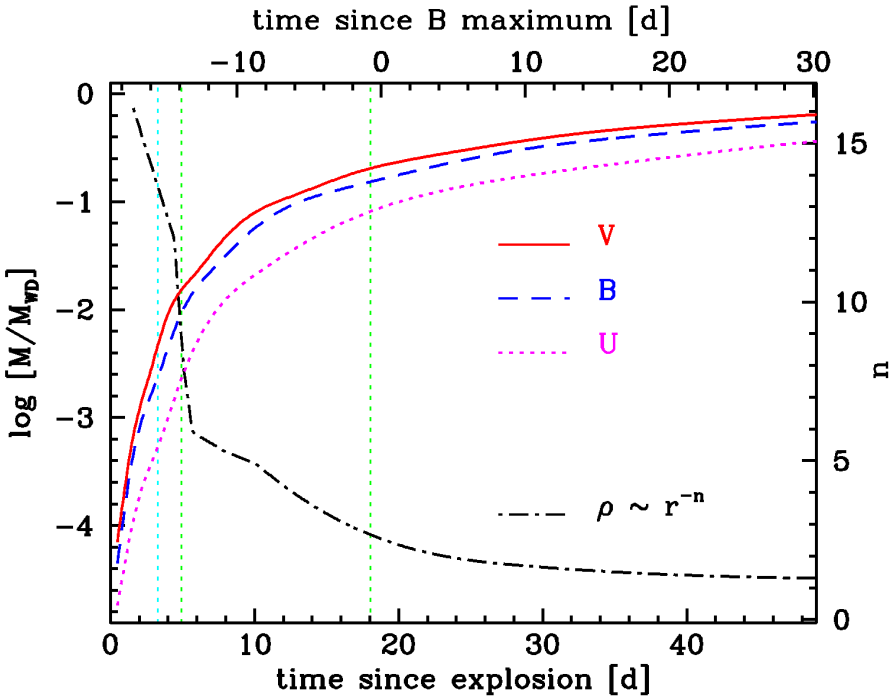

Figure 21. Mass above the photosphere as a function of time for the normal-bright delayed-detonation model 27 (Hoeflich et al. 2017). In addition, we give exponent n which approximates the density structure at the photosphere in B and V. The vertical lines at 3.3, 4.9 and 18.0 days since explosion mark the times with the first flux (cyan) and the polarization spectra (green), respectively. The uncertainty in the phase are ≈ 0.92 days corresponding. In the $V-$band range, we probe the outer $(0.3-1)\times10^{-2}M_\odot$, $(1-3)\times10^{-2}M_\odot$ and $0.2-0.3M_\odot$, respectively.

of the DDT. The polarization of SN 2018gv can be understood in very similar terms as SN 2004dt, a normal-bright Type Ia SN but with a slightly steeper decline rate (i.e., $\Delta m_B(15) = 1.13 \pm 0.04$ mag, Wang et al. 2012). At about one week before maximum, the polarization in SN 2004dt was high in Si II lines, weak in Mg II without showing O I polarization (Höflich et al. 2006; Wang et al. 2006). The observation was reproduced by an off-center DDT model seen from 30° relative the axis of symmetry. At this phase the photosphere passes the interface between explosive carbon and incomplete silicon burning. It could be understood in terms of covering the underlying scattering photosphere by optically thick lines in combination with the chemical gradients. Namely, all strong Si II lines show similar polarization because both are optically thick at this phase, the magnesium polarization is formed in thin shell produced by explosive carbon burning. Oxygen shows little polarization because, in a C/O WD, in explosive carbon burning increases O to about 70% but the constrast is too small with the unburned C/O layers at about 50%.

Similarly, SN 2018gv shows no O I polarization because there is neither an abundance jump in Oxygen in the line forming region at −13.6 and −0.5 day. The Si II λ6355 line shows little polarization at −13.6 day because the line is partially optically thin as discussed above as indicated by the linear blue line wings (see above) and, thus, there is little asymmetric covering of the underlying photosphere. By −0.5 day, the underlying has entered the Si/S-rich region resulting p of about 0.8%. Compared to SN 2004dt with a p(SiII) =1.8% (Wang et al. 2006; Höflich et al. 2006). The line polarization may lower because, for the higher luminosity of SN 2018gv, the Si region is shifted

towards lower density and lower optical depth, at a different phase or we may see the object from a slightly larger inclination. The first effect likely is important because the flux in the blue wing of the Si II line is hardly polarized. Future dense series of earlier-phase spectroplarimetry will allow for a separation of the effects.

Now, we want to shift towards the continuum polarization which, early on, can be understood in terms of an asymmetric density/electron distribution. The low continuum polarization observed gives important limits on the overall this asymmetry. During the phase considered, the photosphere is formed in the C/O/Mg/Si/S layers, and the ionization fraction does hardly change because similar ionization potentials of the main electron donors. As a result, the electron distribution at the photosphere can be approximated by the density distribution. The polarization depends on the density structure and decreases with steeper density slopes because the incoming radiation at the photosphere becomes more isotropic.

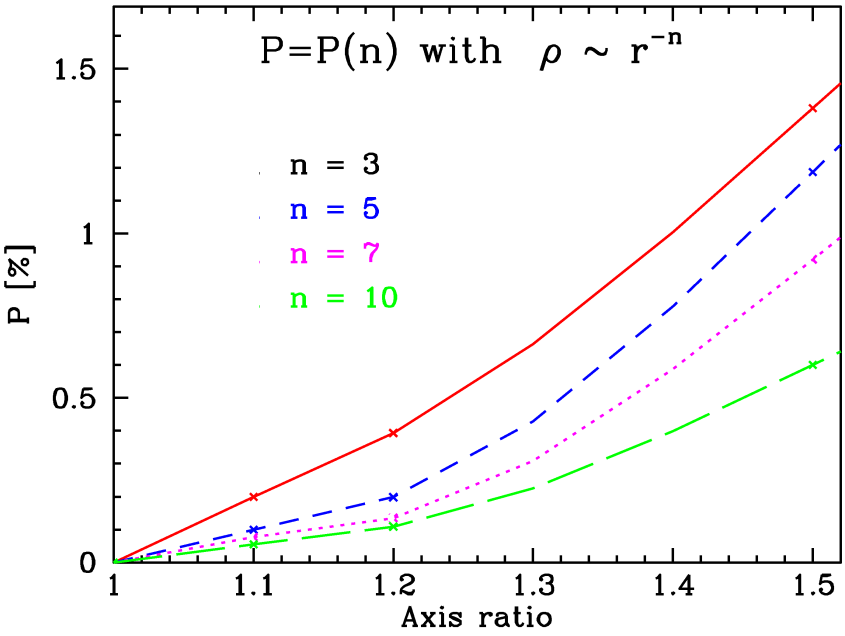

Figure 22. Continuum polarization as a function of asymmetry in a scattering dominated frequency range formed in the region of intermediate mass elements. We assume a oblate ellipsoide with an axis ratio of A/B and depolarization at a Thomson optical depth of 5.

In Fig. 22, we give the the polarization seen equator-on for oblate ellipsoids with an axis ratio of A/B for various density slopes n for structures realized in models. For SN 2018gv, the continuum polarization is 0.20%±0.13% and 0.15%±0.16% at about −13.6 day and maximum light, respectively. The outer $(1-2)\times10^{-2}M_{\odot}$ are aspherical with a well defined axis because the constant polarization angle. The size of asymmetry is about 10% to 35% when seen equator on. We see significant asymmetry early on. By maximum light, p declined and it is consistent with no polarization. The size of asymmetry is between 0% and 15%. Note that p goes roughly as $\propto \sin^2(\Theta)$ but, due to multiple scattering effects, the change of p becomes less steep Höflich (1991).

It is beyond the scope of this paper for a full analysis, but we would like to put SN 2018gv into context of different mechanism for producing asymmetry. a) Dynamical or head on collisions of

WD show larger asymmetries and can be ruled out because they predict larger asymmetries in the inner layers or off-center energy sources (Benz et al. 1990; Pakmor et al. 2011; Sato et al. 2016; Katz et al. 2016; García-Berro et al. 2017; García-Berro & Lorén-Aguilar 2017); b) Rapidly rotating WDs close to $M_{\rm Ch}$ produce asymmetric initial configuration and are consistent with the polarization seen in this object (Eriguchi & Mueller 1993; Yoshida 2018); He-triggered detonations do produce strong asymmetries in the outer layers and, consistent with SN 2018gv, show almost spherical inner layers (Shen & Moore 2014). One problem, though, may be that the early observations place the photosphere into He-rich layers and its burning products for all but WDs at the upper end of the masses possible. Both the flux and polarization spectra indicate no 'double-chemical' structure of Si/S starting within the outer $3 \times 10^{-3} M_{\odot}$. The lack of O I polarization puts an even stronger limit on a He layer atop $10^{-2} M_{\odot}$.

Though the picture of a rotating WD within the off-center delayed-detonation scenario seems to be consistent, we need earlier observations and denser series of spectroplarimetry obtained than obtained for SN 2018gv.

7. SUMMARY

We present extensive UV and optical photometry, optical spectroscopy as well as optical linear spectropolarimetry of SN 2018gv. We are able to draw the following conclusions:

1) The rising light curve is consistent with a power-law exponent [$f(t) \propto (t - t_0)^n$]. Our fitting to the early $g'-$band light curve yields a rise time of $\sim$18 days and an index of $n \sim 2$;

2) We adopt the 'CMAGIC' method and estimate the host-galaxy reddening towards SN 2018gv to be negligible [i.e. $E(B-V)_{\rm host} = 0.028 \pm 0.027$ mag];

3) The light curves show that SN 2018gv is a normal Type Ia SN with a typical $B-$band peak magnitude of -19.06 ± 0.05 and a luminosity decline rate $\Delta m_{15}(B) = 0.96 \pm 0.05$ in the rest-frame;

4) The comprehensive photometry allows us to construct the UV-optical pseudo-bolometric light curve of SN 2018gv in the 1660$-$8180 Å range. The bolometric luminosities are estimated after further correcting for the fraction of the NIR flux. The maximum bolometric luminosity gives $L = (1.186 \pm 0.064 \pm 0.022) \times 10^{43}$ erg s^{-1}, yielding a synthesized nickel mass of $0.56 \pm 0.08 M_{\odot}$;

5) The early-time spectra of SN 2018gv exhibit strong similarity to those of the normal Type Ia SN 2011fe in most respects. No significant HV component is detected in the Si II λ6355 absorption feature as early as -15.2 days relative to the $B-$band maximum. Strong HV features are unambiguously detected in Ca II NIR3 features. At velocities from $-27{,}000$ to $-20{,}000$ km s^{-1}, they are detached from the photosphere;

6) The earliest spectropolarimetry to date of a Type Ia SN at day -13.6 has been obtained for SN 2018gv. The degree of continuum polarization is as low as $\sim$0.2%. The observation of low continuum polarization overlaid by significant line polarization is inconsistent with the double-degenerate violent merger case but consistent with the single-degenerate delayed-detonation and double-detonation models;

7) An asymmetric polarization profile of the Si II λ6355 feature around the light curve peak has been observed. The very strong polarization at line center implies a sharp increase of the opacity gradient in the direction transverse to the line of sight as the photosphere recedes to the interface layer of Fe and IME. The sharp drop of polarization towards lower velocities suggests the presence of a distinct chemical 'boundary layer', while the slow decline of polarization towards higher velocities indicates the formation of a rather diffuse and homogeneous ejecta profile above the photosphere;

8) The flux and polarization spectra are consistent with classical off-center delayed detonation transitions with $M_{\rm Ch}$ mass WDs but originating from a rapidly rotating WD. However, our observations are insufficient to address a possible alignment of the symmetry axes in density and abundances. Double-detonation models would require masses close to $1.2 M_{\odot}$.

9) Such an asymmetric Si II λ6355 polarization profile around the SN peak luminosity may indicate that in opposite directions from the stellar center IMEs were produced over different distances. This is consistent with an off-center delayed detonation.

Taken together, our observations suggest that SN 2018gv resembles other normal Type Ia SNe in many respects. Polarimetry of infant SNe (SNe discovered within 1−2 days after their explosion) provide an important probe of the kinematics and chemical structures of SNe and their circumstellar environment during the final stages of the progenitor evolution. Wide-field, high-cadence transient surveys, such as the Zwicky Transient Facility (Bellm et al. 2019), ATLAS (Tonry 2011), ASAS-SN (Shappee et al. 2014), and DLT40 (Tartaglia et al. 2018) will discover and monitor nearby infant SNe over the next few years. A large polarimetry sample of such objects will enable stringent constraints on the explosion mechanisms and the circumstellar environment of Type Ia SNe.

We are grateful to the European Organisation for Astronomical Research in the Southern Hemisphere for the generous allocation of observing time. We would like to especially thank the staff of the Paranal Observatory for their proficient and diligent support of this project in service mode. We acknowledge Gwen Eadie, Dino Bektešević, and Bryce Bolin, co-observers on the night the DIS spectrum was obtained. The polarimetry studies in this work are based on observations made with ESO VLT at the Paranal Observatory under programme ID 0102.D-0528. PyRAF, PyFITS, STSCI_PYTHON are products of the Space Telescope Science Institute, which is operated by AURA for NASA. STScI is operated by the Association of Universities for Research in Astronomy, Inc., under NASA contract NAS5-26555. This research has made use of NASA's Astrophysics Data System Bibliographic Services. This research has made use of the SIMBAD database, operated at CDS, Strasbourg, France. This research has made use of the NASA/IPAC Extragalactic Database (NED) which is operated by the Jet Propulsion Laboratory, California Institute of Technology, under contract with the National Aeronautics and Space Administration. The research of Y. Yang is supported through a Benoziyo Prize Postdoctoral Fellowship. P. Hoeflich is supported by the NSF project "Signatures of Type Ia Supernovae, New Physics and Cosmology", grant AST-1715133. The research of J. Maund is supported through a Royal Society University Research Fellowship. The supernova research by L. Wang is supported by NSF award AST-1817099 and HST-GO-14139.001-A. P. J. Brown was partially supported by a Mitchell Postdoctoral Fellowship. H.F. Stevance is supported

by a PhD scholarship fron the University of Sheffield. This work at Rutgers University (S. W. Jha) is supported by NSF award AST-1615455. M. L. Graham acknowledges support from the DIRAC Institute in the Department of Astronomy at the University of Washington. The DIRAC Institute is supported through generous gifts from the Charles and Lisa Simonyi Fund for Arts and Sciences, and the Washington Research Foundation. This work makes used of data from the Las Cumbres Observatory Network. D. Hiramatsu, C. McCully, and G. Hosseinzadeh were supported by NSF grant AST-1313484. Research by D. J. Sand is supported by NSF grants AST-1821987 and 1821967. X. Wang is supported by the National Natural Science Foundation of China (NSFC grants 11178003 and 11325313). J. C. Wheeler is supported by NSF grant AST-1813825. J. Zhang is supported by the NSFC (grants 11773067, 11403096), the Youth Innovation Promotion Association of the CAS (grants 2018081) and the Western Light Youth Project of the CAS.

Table 1. Photometric standards in the SN 2018gv field

ID	α(J2000)	δ(J2000)	U (mag)	B (mag)	V (mag)	g (mag)	r (mag)	i (mag)
1	8:05:39.190	-11:23:57.77		13.199(028)	12.707(015)	12.897(027)	12.590(044)	12.533(044)
2	8:05:34.667	-11:23:32.26		14.029(027)	12.973(023)	13.439(040)	12.640(047)	12.402(029)
3	8:05:38.418	-11:30:10.37	11.80	11.856(035)	11.494(010)	11.612(041)	11.417(038)	11.432(028)
4	8:05:34.874	-11:22:33.51		13.008(033)	12.655(022)	12.754(023)	12.598(043)	12.638(035)
5	8:05:44.471	-11:32:12.54	11.07	10.888(022)	10.714(017)	10.729(030)	10.772(074)	10.870(039)
6	8:06:03.681	-11:28:56.15		13.276(041)	11.996(022)	12.597(047)	11.549(041)	11.166(025)
7	8:05:15.921	-11:34:21.17		13.545(050)	11.890(051)	12.631(063)	11.243(090)	10.072(000)
8	8:05:08.379	-11:31:24.17		12.948(021)	12.450(020)	12.644(024)	12.308(048)	12.239(027)
9	8:06:06.937	-11:26:14.69		13.309(036)	11.904(026)	12.577(048)	11.366(045)	10.914(038)
10	8:06:07.016	-11:31:35.82		12.222(020)	11.694(026)	11.904(033)	11.551(051)	11.443(041)
11	8:06:04.411	-11:24:29.13		13.381(032)	12.293(019)	12.786(045)	11.944(044)	11.680(026)
12	8:04:46.849	-11:23:58.66		13.279(015)	11.684(033)	12.448(044)	11.076(045)	10.496(090)
13	8:04:59.549	-11:19:29.13	13.73	12.901(009)	11.726(017)	12.247(043)	11.312(037)	10.968(022)
14	8:05:09.374	-11:16:13.25	10.51	10.836(020)	10.839(024)	10.740(036)	10.959(055)	11.205(029)
15	8:05:52.649	-11:23:37.18		13.838(022)	13.274(029)	13.501(032)	13.112(041)	13.038(027)
16	8:05:41.910	-11:27:49.40		14.812(026)	13.737(033)	14.240(067)	13.356(043)	13.071(015)
17	8:05:30.515	-11:24:07.41		14.503(041)	13.956(018)	14.183(034)	13.792(048)	13.717(025)
18	8:05:48.271	-11:28:03.66		14.380(025)	13.840(016)	14.068(032)	13.699(044)	13.603(044)
19	8:06:05.047	-11:21:19.65		13.645(022)	13.253(030)	13.378(013)	13.200(029)	13.153(042)
20	8:05:15.276	-11:25:40.51		14.811(022)	13.774(036)	14.219(022)	13.460(033)	13.141(028)
21	8:05:19.620	-11:20:45.77		13.686(022)	13.208(016)	13.382(034)	13.089(053)	13.019(012)
22	8:05:05.024	-11:20:18.45		13.324(020)	12.814(011)	13.009(029)	12.678(056)	12.584(022)
23	8:05:00.250	-11:25:08.76		13.549(011)	12.696(031)	13.056(030)	12.391(039)	12.180(034)
24	8:05:10.005	-11:16:43.26		14.011(023)	12.622(035)	13.342(030)	12.007(047)	11.407(013)
25	8:05:46.770	-11:31:36.23		13.927(031)	12.901(030)	13.367(044)	12.530(046)	12.228(023)
26	8:05:18.257	-11:26:31.45		15.140(049)	14.023(020)	14.521(035)	13.636(041)	13.288(021)
27	8:05:05.733	-11:17:44.99	13.74	12.718(022)	11.826(013)	12.219(032)	11.544(050)	11.298(022)

Table 2. Log of spectroscopic observations of SN 2018gv

UT Date (2018)	MJD	Phase[a] (days)	Range (Å)	Exposure (s)	Instrument/Telescope
Jan 16 12:08	58134.50	-15.18	3200−9900	2700	FLOYDS/LCO 2.0 m FTN
Jan 17 08:13	58135.34	-14.34	3200−9900	2700	FLOYDS/LCO 2.0 m FTN
Jan 17 11:53	58135.50	-14.19	3500−9900	300	GMOS-N/Gemini-N 8.1 m
Jan 18 02:20	58136.10	-13.59	4400−9200	4×900	FORS2/VLT 8.2 m
Jan 18 11:05	58136.46	-13.23	3200−9900	2700	FLOYDS/LCO 2.0 m FTN
Jan 19 06:55	58137.29	-12.40	3600−10200	767	LRS2/HET 10 m
Jan 20 10:04	58138.42	-11.27	3200−9900	2700	FLOYDS/LCO 2.0 m FTN
Jan 23 09:42	58141.41	-8.28	3200−9900	1800	FLOYDS/LCO 2.0 m FTN
Jan 25 07:57	58143.33	-6.36	3200−9900	1800	FLOYDS/LCO 2.0 m FTN
Jan 25 20:35	58143.75	-5.94	3500−8900	2401	RSS/SALT 11 m
Jan 28 06:33	58146.27	-3.41	3600−10200	507	LRS2/HET 10 m
Jan 29 08:50	58147.37	-2.32	3200−9900	1800	FLOYDS/LCO 2.0 m FTN
Jan 31 05:08	58149.21	-0.47	4400−9200	4×120	FORS2/VLT 8.2 m
Feb 04 10:13	58153.43	3.74	3200−9900	1800	FLOYDS/LCO 2.0 m FTS
Feb 08 10:45	58157.45	7.76	3200−9900	1800	FLOYDS/LCO 2.0 m FTS
Feb 13 06:38	58162.28	12.59	3200−9900	1800	FLOYDS/LCO 2.0 m FTN
Mar 01 12:06	58178.50	28.82	4800−9300	1800	FLOYDS/LCO 2.0 m FTS
Mar 09 13:45	58186.57	36.89	3300−9900	1800	FLOYDS/LCO 2.0 m FTS
Mar 17 11:28	58194.48	44.79	3400−9900	1800	FLOYDS/LCO 2.0 m FTS
Mar 22 03:49	58199.66	49.97	3800−9200	900	DIS/ARC 3.5 m
Mar 23 11:28	58200.48	50.79	3300−9900	1800	FLOYDS/LCO 2.0 m FTS
Mar 29 10:26	58206.43	56.75	4800−9300	1800	FLOYDS/LCO 2.0 m FTS
Apr 05 10:43	58213.45	63.76	3200−9900	1800	FLOYDS/LCO 2.0 m FTS
Apr 11 11:36	58219.48	69.80	3600−9300	2700	FLOYDS/LCO 2.0 m FTS
Apr 17 11:04	58225.46	75.77	3700−9200	2700	FLOYDS/LCO 2.0 m FTS
Apr 25 06:52	58233.29	83.60	3200−9900	2700	FLOYDS/LCO 2.0 m FTN

[a]Relative to the $B-$band maximum light, MJD_{Bmax} = 58,149.698±0.510 / 2018 Jan 31 16:45

Table 3. LCO $UBg'Vr'i'$ photometry of SN 2018gv. The table is published in its entirety in the electronic edition of the journal. A portion is displayed for guidance regarding its form and content.

MJD[a]	U (mag)	MJD[a]	B (mag)	MJD[a]	V (mag)	MJD[a]	g' (mag)	MJD[a]	r' (mag)	MJD[a]	i' (mag)
...	...	134.078	16.763(008)	134.086	16.426(008)	134.090	16.562(006)	134.094	16.417(008)	134.098	16.777(014)
...	...	134.082	16.772(008)	134.086	16.415(008)	134.094	16.552(006)	134.098	16.425(008)	134.102	16.769(014)
134.863	16.330(013)	134.871	16.123(005)	134.879	15.896(006)	134.883	15.969(004)	134.887	15.914(006)	134.891	16.254(011)
134.867	16.312(014)	134.875	15.111(005)	134.879	15.888(006)	134.887	15.964(004)	134.891	15.911(006)	134.895	16.269(012)
...	...	....	...	...	...	...	...	...	...	...	...
150.820	12.557(002)	150.828	12.813(002)	150.828	12.861(003)	150.832	12.818(002)	150.836	12.941(003)	150.836	13.593(006)
150.824	12.556(002)	150.828	12.817(002)	150.832	12.862(003)	150.832	12.817(002)	150.836	12.941(003)	150.836	13.582(006)
...	...	....	...	...	...	...	...	...	...	...	...
254.980	17.218(044)	254.984	16.920(013)	254.988	16.472(013)	254.992	16.542(009)	254.996	16.743(016)	254.996	17.164(034)
254.980	17.354(112)	254.988	16.899(013)	254.988	16.497(013)	254.992	16.536(008)	254.996	16.727(016)	254.996	17.072(031)
264.723	17.427(084)	264.727	17.061(030)	264.730	16.717(029)	264.734	16.653(017)	264.738	17.021(033)	264.738	17.393(064)
264.727	17.461(088)	264.730	17.094(031)	264.734	16.657(028)	264.734	16.691(018)	264.738	17.020(032)	264.742	17.390(065)
...	...	286.961	17.404(026)	286.965	17.136(023)	286.965	17.038(013)	286.969	17.620(031)	286.973	18.056(070)
...	...	286.961	17.400(026)	286.965	17.189(024)	286.969	17.047(013)	286.969	17.660(032)	286.973	17.972(064)

[a]MJD - 58,000, MJD of the $B-$band maximum light;

Table 4. Photometric parameters of SN 2018gv

Band	λ_{pivot} (Å)	$A_\lambda^{\rm MW}$ (mag)	$A_\lambda^{\rm Host}$ (mag[b])	t_{max}^a (day)	Δm_{15} (mag[c])	m_{peak} (mag[c])	M_{peak} (mag[c])
U	3600	0.251	0.131±0.125	47.518(430)	1.027(050)	12.230(046)	-19.442(048)
B	4365	0.210	0.109±0.110	49.698(510)	0.963(054)	12.609(051)	-19.063(053)
V	5362	0.159	0.087±0.086	50.598(520)	0.626(028)	12.696(025)	-18.976(027)
g'	4736	0.191	0.102±0.097	49.928(545)	0.726(043)	12.641(044)	-19.031(045)
r'	6232	0.132	0.068±0.068	50.078(450)	0.703(018)	12.778(043)	-18.894(044)
i'	7529	0.098	0.053±0.052	47.688(405)	0.878(016)	13.342(055)	-18.330(066)

[a]Uncertainties of maximum-light dates in unit of 0.01 days. The date is MJD−58100.

[b]Uncertainties were not added when deducing the photometric parameters.

[c]Uncertainties are indicated by the number in parentheses and in unit of 0.01 magnitude.

Table 5. Fit Results of the different velocity components, velocities shown in absolute value.

	Si II λ5972		Si II λ6355		C II λ6580		High Velocity Ca NIR3		Normal Velocity Ca NIR3	
Phase	v	pEW	v	pEW	v	pEW	v	pEW	v	pEW
(day)	(km s^{-1})	(Å)	(km s^{-1})	(Å)	(km s^{-1})	(Å)	(km s^{-1})	(Å)	km s^{-1})	(Å)
-15.18	12894(277)	11.2(1.4)	16321(245)	146.3(2.3)	15038(254)	10.4(1.2)	27297(369)	94.9(23.8)	19233(610)	238.2(33.6)
-14.34	11996(277)	13.8(1.7)	15322(245)	138.2(2.4)	14635(261)	7.5(1.3)	25636(373)	78.2(37.6)	18260(930)	236.9(50.6)
-14.19	12172(138)	19.6(1.9)	15354(92)	136.0(2.5)	14322(134)	5.0(1.3)	24942(203)	150.9(11.5)	16379(278)	175.0(14.0)
-13.59	11999(375)	15.2(2.8)	14769(343)	123.8(4.0)	14209(386)	4.1(2.1)	24187(456)	118.4(19.5)	15804(582)	172.5(27.5)
-13.23	11559(289)	16.0(2.3)	14390(246)	124.0(2.9)	14112(285)	3.2(1.4)	23941(424)	101.5(29.1)	16290(988)	165.7(40.3)
-12.40	11569(115)	24.2(1.5)	14004(86)	113.5(1.9)	13755(125)	4.6(1.1)	23528(330)	102.2(14.2)	16546(504)	75.7(16.0)
-11.27	10619(316)	12.0(2.3)	13029(247)	99.8(2.8)	13309(342)	2.8(1.6)	22686(336)	63.6(12.2)	14142(589)	94.7(19.3)
-8.28	9225(507)	8.5(3.0)	11873(248)	82.6(3.1)			22200(302)	35.5(6.3)	12539(341)	62.4(9.6)
-6.36	9667(422)	5.7(2.5)	11468(248)	83.6(3.3)			21579(316)	32.0(6.5)	11466(319)	55.4(8.7)
-5.94	9117(522)	14.6(3.6)	11499(154)	73.4(2.7)			22148(241)	26.3(5.5)	12846(216)	87.4(8.8)
-3.41	10490(275)	10.1(2.0)	11199(87)	81.4(2.1)			21217(199)	10.4(3.4)	10905(541)	24.8(7.2)
-2.32	9244(441)	10.5(3.3)	11022(248)	89.2(3.6)			20467(130)	17.3(5.2)	11639(283)	75.5(8.1)
-0.47	10533(727)	8.1(4.6)	10984(345)	84.2(5.3)			20227(410)	7.4(3.6)	12551(350)	107.4(6.8)
3.74			10673(251)	92.7(5.7)					11673(458)	141.3(40.5)
7.76			10650(249)	92.1(5.0)			18483[a]		11626(311)	275.5(25.3)

[a]Multi-Gaussian component fitting failed. Velocity assigned by the local minimum and no error estimatation applied.

Table 6. The pseudo-bolometric (UVO) and the estimated bolometric (UVOIR) luminosity of SN 2018gv (left) and SN 2011fe (right)

Phase[a] Day	$\log L$ (UVO) (erg s^{-1})	Error[b] (erg s^{-1})	$\log L$ (UVOIR) (erg s^{-1})	Phase[c] Day	$\log L$ (UVO) (erg s^{-1})	Error[b] (erg s^{-1})	$\log L$ (UVOIR) (erg s^{-1})
-15.61	41.463	0.022	41.532	-16.31	40.962	0.016	41.030
-14.81	41.693	0.022	41.761	-15.95	41.151	0.016	41.219
-14.57	41.747	0.022	41.815	-15.32	41.409	0.016	41.478
-14.38	41.805	0.022	41.874	-14.95	41.535	0.016	41.603
-12.72	42.192	0.023	42.261	-14.31	41.713	0.016	41.782
-12.34	42.266	0.023	42.335	-13.95	41.813	0.016	41.882
-11.62	42.382	0.023	42.452	-12.96	42.039	0.016	42.108
-11.42	42.434	0.023	42.503	-12.33	42.156	0.016	42.226

Continued on next page

Table 6 – *Continued from previous page*

Phase[a] Day	$\log L$ (UVO) (erg s^{-1})	Error[b] (erg s^{-1})	$\log L$ (UVOIR) (erg s^{-1})	Phase[c] Day	$\log L$ (UVO) (erg s^{-1})	Error[b] (erg s^{-1})	$\log L$ (UVOIR) (erg s^{-1})
-10.55	42.562	0.024	42.631	-11.96	42.238	0.016	42.308
-10.45	42.574	0.024	42.643	-11.33	42.345	0.016	42.414
-9.78	42.651	0.024	42.720	-10.96	42.420	0.016	42.489
-9.60	42.670	0.024	42.739	-10.33	42.501	0.016	42.571
-9.47	42.685	0.024	42.753	-9.95	42.562	0.016	42.632
-8.87	42.740	0.024	42.809	-9.33	42.630	0.016	42.699
-8.54	42.770	0.024	42.838	-8.96	42.674	0.016	42.743
-8.41	42.760	0.023	42.827	-8.34	42.721	0.016	42.789
-7.78	42.824	0.024	42.891	-7.96	42.767	0.016	42.835
-7.55	42.823	0.023	42.890	-7.34	42.801	0.016	42.869
-6.83	42.883	0.023	42.950	-6.94	42.840	0.016	42.908
-6.57	42.879	0.023	42.946	-6.34	42.874	0.016	42.940
-6.03	42.924	0.023	42.991	-4.96	42.942	0.016	43.007
-5.88	42.931	0.023	42.997	-4.34	42.964	0.017	43.028
-2.89	43.005	0.023	43.069	-3.34	42.989	0.016	43.053
-1.83	43.012	0.023	43.076	-2.34	43.003	0.016	43.067
-1.40	43.010	0.022	43.073	-1.34	43.011	0.016	43.074
1.14	42.998	0.022	43.059	0.65	43.006	0.016	43.067
2.13	42.983	0.022	43.043	1.65	42.992	0.016	43.052
3.23	42.966	0.022	43.024	2.65	42.984	0.016	43.043
4.09	42.948	0.021	43.005	3.03	42.957	0.017	43.015
5.15	42.928	0.021	42.985	3.65	42.963	0.017	43.020
6.97	42.879	0.021	42.935	4.65	42.954	0.017	43.010
8.33	42.847	0.024	42.903	6.64	42.902	0.017	42.957
10.35	42.789	0.021	42.848	9.04	42.807	0.018	42.864
13.57	42.676	0.022	42.750	10.01	42.734	0.018	42.793
16.38	42.580	0.022	42.668	11.01	42.693	0.019	42.755
19.39	42.494	0.022	42.606	12.01	42.668	0.019	42.734
22.52	42.419	0.022	42.562	12.99	42.632	0.019	42.701
25.16	42.364	0.021	42.524	14.00	42.599	0.020	42.673
28.33	42.302	0.022	42.481	14.98	42.557	0.020	42.637
31.50	42.233	0.022	42.423	15.99	42.524	0.020	42.612
34.54	42.179	0.022	42.379	20.97	42.423	0.018	42.551
39.39	42.066	0.022	42.260	21.97	42.370	0.017	42.505
42.41	42.006	0.022	42.189	22.97	42.364	0.017	42.507
43.50	41.993	0.022	42.174	24.97	42.311	0.016	42.471
46.47	41.953	0.023	42.130	25.97	42.300	0.016	42.468
46.84	41.954	0.022	42.131	33.97	42.112	0.016	42.311

Continued on next page

Table 6 – *Continued from previous page*

Phase[a] Day	$\log L$ (UVO) (erg s^{-1})	Error[b] (erg s^{-1})	$\log L$ (UVOIR) (erg s^{-1})	Phase[c] Day	$\log L$ (UVO) (erg s^{-1})	Error[b] (erg s^{-1})	$\log L$ (UVOIR) (erg s^{-1})
53.47	41.874	0.022	42.029	35.96	42.062	0.016	42.262
57.84	41.830	0.022	41.974	36.96	42.044	0.016	42.243
61.77	41.795	0.022	41.929	37.97	42.023	0.016	42.219
65.43	41.744	0.022	41.870	43.95	41.936	0.016	42.116
73.33	41.670	0.022	41.777	80.39	41.538	0.016	41.628
77.38	41.633	0.022	41.731	92.41	41.418	0.017	41.498
78.39	41.629	0.022	41.724	94.43	41.409	0.017	41.489
87.72	41.549	0.022	41.629	96.45	41.384	0.017	41.464
97.73	41.448	0.022	41.528	97.38	41.365	0.017	41.445
–	–	–	–	98.45	41.353	0.017	41.433
–	–	–	–	99.38	41.339	0.017	41.419

[a]Relative to the epoch of $B-$band maximum of SN 2018gv (MJD = 58,149.698±0.510);
[b]Uncertainty in the distance not included;
[c]Relative to the epoch of $B-$band maximum of SN 2011fe (MJD = 55,814.48±0.03));

REFERENCES

Anderson, J. *et al.* 2018, EUROPEAN SOUTHERN OBSERVATORY, Doc. No. VLT-MAN-ESO-13100-1543

Appenzeller, I., Fricke, K., Fürtig, W., et al. 1998, The Messenger, 94, 1

Arnett, W. D. 1969, AP&SS, 5, 180

—. 1982, ApJ, 253, 785

Bagnulo, S., Landolfi, M., Landstreet, J. D., et al. 2009, PASP, 121, 993

Bagnulo, S., Cox, N. L. J., Cikota, A., et al. 2017, A&A, 608, A146

Bellm, E. C., Kulkarni, S. R., Graham, M. J., et al. 2019, PASP, 131, 018002

Benetti, S., Cappellaro, E., Mazzali, P. A., et al. 2005, ApJ, 623, 1011

Benz, W., Bowers, R. L., Cameron, A. G. W., & Press, W. H. . 1990, ApJ, 348, 647

Blanton, M. R., & Roweis, S. 2007, AJ, 133, 734

Blondin, S., & Tonry, J. L. 2007, ApJ, 666, 1024

Branch, D., Baron, E., Hall, N., Melakayil, M., & Parrent, J. 2005, PASP, 117, 545

Branch, D., Jeffery, D. J., Young, T. R., & Baron, E. 2006, PASP, 118, 791

Branch, D., & Wheeler, J. C. 2017, Supernova Explosions, doi:10.1007/978-3-662-55054-0

Breeveld, A. A., Landsman, W., Holland, S. T., et al. 2011, in American Institute of Physics Conference Series, Vol. 1358, GAMMA RAY BURSTS 2010. AIP Conference Proceedings, ed. J. E. McEnery, J. L. Racusin, & N. Gehrels, 373–376

Brown, P. J., Breeveld, A., Roming, P. W. A., & Siegel, M. 2016, AJ, 152, 102

Brown, P. J., Breeveld, A. A., Holland, S., Kuin, P., & Pritchard, T. 2014, A&SS, 354, 89

Bulla, M., Sim, S. A., Pakmor, R., et al. 2016a, MNRAS, 455, 1060

Bulla, M., Sim, S. A., Kromer, M., et al. 2016b, MNRAS, 462, 1039

Cao, Y., Kulkarni, S. R., Howell, D. A., et al. 2015, Nature, 521, 328

Cardelli, J. A., Clayton, G. C., & Mathis, J. S. 1989, ApJ, 345, 245

Childress, M. J., Filippenko, A. V., Ganeshalingam, M., & Schmidt, B. P. 2014, MNRAS, 437, 338

Chonis, T. S., Hill, G. J., Lee, H., et al. 2016, in PROCSPIE, Vol. 9908, Ground-based and Airborne Instrumentation for Astronomy VI, 99084C

Chugai, N. N. 1992, Soviet Astronomy Letters, 18, 168

Cikota, A., Patat, F., Cikota, S., & Faran, T. 2017, MNRAS, 464, 4146

Conley, A., Howell, D. A., Howes, A., et al. 2006, AJ, 132, 1707

Contreras, C., Phillips, M. M., Burns, C. R., et al. 2018, ApJ, 859, 24

Crawford, S. M., Still, M., Schellart, P., et al. 2010, in Society of Photo-Optical Instrumentation Engineers (SPIE) Conference Series, Vol. 7737, Society of Photo-Optical Instrumentation Engineers (SPIE) Conference Series, 25

Davenport, J., d. M. W. T. D. 2018, PyDIS, https://github.com/TheAstroFactory/pydis, doi:10.5281/zenodo.58753

Davies, R. L., Allington-Smith, J. R., Bettess, P., et al. 1997, in PROCSPIE, Vol. 2871, Optical Telescopes of Today and Tomorrow, ed. A. L. Ardeberg, 1099–1106

Diamond, T. R., Hoeflich, P., & Gerardy, C. L. 2015, ApJ, 806, 107

Edwards, Z. I., Pagnotta, A., & Schaefer, B. E. 2012, ApJL, 747, L19

Eriguchi, Y., & Mueller, E. 1993, ApJ, 416, 666

Fesen, R. A., Höflich, P. A., Hamilton, A. J. S., et al. 2007, ApJ, 658, 396

Fink, M., Röpke, F. K., Hillebrandt, W., et al. 2010, A&A, 514, A53

Firth, R. E., Sullivan, M., Gal-Yam, A., et al. 2015, MNRAS, 446, 3895

Folatelli, G., Phillips, M. M., Burns, C. R., et al. 2010, AJ, 139, 120

Folatelli, G., Phillips, M. M., Morrell, N., et al. 2012, ApJ, 745, 74

Fossati, L., Bagnulo, S., Mason, E., & Landi Degl'Innocenti, E. 2007, in Astronomical Society of the Pacific Conference Series, Vol. 364, The Future of Photometric, Spectrophotometric and Polarimetric Standardization, ed. C. Sterken, 503

Fukugita, M., Ichikawa, T., Gunn, J. E., et al. 1996, AJ, 111, 1748

Gamezo, V. N., Khokhlov, A. M., & Oran, E. S. 2004, Physical Review Letters, 92, 211102
—. 2005, ApJ, 623, 337
Ganeshalingam, M., Li, W., & Filippenko, A. V. 2011, MNRAS, 416, 2607
Garavini, G., Folatelli, G., Nobili, S., et al. 2007, A&A, 470, 411
García-Berro, E., Badenes, C., Aznar-Siguán, G., & Lorén-Aguilar, P. 2017, MNRAS, 468, 4815
García-Berro, E., & Lorén-Aguilar, P. 2017, Dynamical Mergers, ed. A. W. Alsabti & P. Murdin, 1237
García-Berro, E., Lorén-Aguilar, P., Aznar-Siguán, G., et al. 2012, ApJ, 749, 25
Garg, A., Stubbs, C. W., Challis, P., et al. 2007, AJ, 133, 403
Gehrels, N., Chincarini, G., Giommi, P., et al. 2004, ApJ, 611, 1005
Goldhaber, G., Groom, D. E., Kim, A., et al. 2001, ApJ, 558, 359
González Hernández, J. I., Ruiz-Lapuente, P., Tabernero, H. M., et al. 2012, Nature, 489, 533
Hayden, B. T., Garnavich, P. M., Kessler, R., et al. 2010, ApJ, 712, 350
Henden, A. A., Templeton, M., Terrell, D., et al. 2016, VizieR Online Data Catalog, 2336
Hillebrandt, W., Kromer, M., Röpke, F. K., & Ruiter, A. J. 2013, Frontiers of Physics, 8, 116
Hoeflich, P. 2017, Explosion Physics of Thermonuclear Supernovae and Their Signatures, ed. A. W. Alsabti & P. Murdin, 1151
Hoeflich, P., & Khokhlov, A. 1996, ApJ, 457, 500
Hoeflich, P., Khokhlov, A. M., & Wheeler, J. C. 1995, ApJ, 444, 831
Hoeflich, P., Wheeler, J. C., Hines, D. C., & Trammell, S. R. 1996, ApJ, 459, 307
Hoeflich, P., Hsiao, E. Y., Ashall, C., et al. 2017, ApJ, 846, 58
Höflich, P. 1991, A&A, 246, 481
Höflich, P., Gerardy, C. L., Fesen, R. A., & Sakai, S. 2002, ApJ, 568, 791
Höflich, P., Gerardy, C. L., Marion, H., & Quimby, R. 2006, New Astronomy Review, 50, 470
Höflich, P., & Stein, J. 2002, ApJ, 568, 779
Hosseinzadeh, G., Sand, D. J., Valenti, S., et al. 2017, ApJL, 845, L11
Howell, D. A. 2011, Nature Communications, 2, 350
Howell, D. A., Höflich, P., Wang, L., & Wheeler, J. C. 2001, ApJ, 556, 302
Hoyle, F., & Fowler, W. A. 1960, ApJ, 132, 565
Hristov, B., Collins, D. C., Hoeflich, P., Weatherford, C. A., & Diamond, T. R. 2018, ApJ, 858, 13
Hsiao, E. Y., Conley, A., Howell, D. A., et al. 2007, ApJ, 663, 1187
Iben, Jr., I., & Tutukov, A. V. 1984, ApJs, 54, 335
Itagaki, K. 2018, Transient Name Server Discovery Report, 57
Johnson, H. L. 1966, ARAA, 4, 193
Jordi, K., Grebel, E. K., & Ammon, K. 2006, A&A, 460, 339
Kasen, D. 2010, ApJ, 708, 1025
Kasen, D., Thomas, R. C., & Nugent, P. 2006, ApJ, 651, 366
Kasen, D., Nugent, P., Wang, L., et al. 2003, ApJ, 593, 788
Katz, M. P., Zingale, M., Calder, A. C., et al. 2016, ApJ, 819, 94
Khokhlov, A. M. 1991, A&A, 245, 114
Krisciunas, K., Contreras, C., Burns, C. R., et al. 2017, AJ, 154, 211
Kromer, M., Sim, S. A., Fink, M., et al. 2010, ApJ, 719, 1067
Kushnir, D., Katz, B., Dong, S., Livne, E., & Fernández, R. 2013, ApJL, 778, L37
Leonard, D. C., Li, W., Filippenko, A. V., Foley, R. J., & Chornock, R. 2005, ApJ, 632, 450
Li, W., Bloom, J. S., Podsiadlowski, P., et al. 2011, Nature, 480, 348
Livne, E. 1990, ApJL, 354, L53
Lorén-Aguilar, P., Isern, J., & García-Berro, E. 2009, A&A, 500, 1193
Maoz, D., Mannucci, F., & Nelemans, G. 2014, ARAA, 52, 107
Maund, J. R., Wheeler, J. C., Baade, D., et al. 2009, ApJ, 705, 1139
Maund, J. R., Wheeler, J. C., Patat, F., et al. 2007, MNRAS, 381, 201
Maund, J. R., Höflich, P., Patat, F., et al. 2010, ApJL, 725, L167
Maund, J. R., Spyromilio, J., Höflich, P. A., et al. 2013, MNRaS, 433, L20
Mazzali, P. A., Benetti, S., Altavilla, G., et al. 2005, ApJL, 623, L37

McCully, C., Volgenau, N. H., Harbeck, D.-R., et al. 2018, in Society of Photo-Optical Instrumentation Engineers (SPIE) Conference Series, Vol. 10707, Software and Cyberinfrastructure for Astronomy V, 107070K
Miller, A. A., Cao, Y., Piro, A. L., et al. 2018, ApJ, 852, 100
Milne, P. A., Williams, G. G., Porter, A., et al. 2017, ApJ, 835, 100
Moll, R., Raskin, C., Kasen, D., & Woosley, S. E. 2014, ApJ, 785, 105
Mulligan, B. W., & Wheeler, J. C. 2018, MNRAS, 476, 1299
Mulligan, B. W., Zhang, K., & Wheeler, J. C. 2019, MNRAS, 484, 4785
Munari, U., Henden, A., Belligoli, R., et al. 2013, J.NewAstron., 20, 30
Munari, U., & Zwitter, T. 1997, A&A, 318, 269
Niemeyer, J. C., Hillebrandt, W., & Woosley, S. E. 1996, ApJ, 471, 903
Nomoto, K. 1982a, ApJ, 257, 780
—. 1982b, ApJ, 253, 798
Nomoto, K., Sugimoto, D., & Neo, S. 1976, APSS, 39, L37
Nugent, P., Baron, E., Branch, D., Fisher, A., & Hauschildt, P. H. 1997, ApJ, 485, 812
Nugent, P. E., Sullivan, M., Cenko, S. B., et al. 2011, Nature, 480, 344
Pakmor, R., Hachinger, S., Röpke, F. K., & Hillebrandt, W. 2011, A&A, 528, A117
Pakmor, R., Kromer, M., Röpke, F. K., et al. 2010, Nature, 463, 61
Pakmor, R., Kromer, M., Taubenberger, S., et al. 2012, ApJL, 747, L10
Pakmor, R., Kromer, M., Taubenberger, S., & Springel, V. 2013, ApJL, 770, L8
Parrent, J. T., Thomas, R. C., Fesen, R. A., et al. 2011, ApJ, 732, 30
Patat, F., Baade, D., Höflich, P., et al. 2009, A&A, 508, 229
Patat, F., Höflich, P., Baade, D., et al. 2012, A&A, 545, A7
Patat, F., & Romaniello, M. 2006, PASP, 118, 146
Patat, F., Cordiner, M. A., Cox, N. L. J., et al. 2013, A&A, 549, A62
Penney, R., & Hoeflich, P. 2014, ApJ, 795, 84
Pereira, R., Thomas, R. C., Aldering, G., et al. 2013, A&A, 554, A27
Perlmutter, S., Aldering, G., Goldhaber, G., et al. 1999, ApJ, 517, 565
Phillips, M. M., Lira, P., Suntzeff, N. B., et al. 1999, AJ, 118, 1766
Pickles, A., & Depagne, É. 2010, PASP, 122, 1437
Piersanti, L., Tornambé, A., & Castellani, V. 2004, MNRAS, 353, 243
Plewa, T., Calder, A. C., & Lamb, D. Q. 2004, ApJL, 612, L37
Porter, A. L., Leising, M. D., Williams, G. G., et al. 2016, ApJ, 828, 24
Poznanski, D., Ganeshalingam, M., Silverman, J. M., & Filippenko, A. V. 2011, MNRAS, 415, L81
Quimby, R. M., Wheeler, J. C., Höflich, P., et al. 2007, ApJ, 666, 1093
Ramsey, L. W., Adams, M. T., Barnes, T. G., et al. 1998, in PROCSPIE, Vol. 3352, Advanced Technology Optical/IR Telescopes VI, ed. L. M. Stepp, 34–42
Rasio, F. A., & Shapiro, S. L. 1994, ApJ, 432, 242
Raskin, C., Kasen, D., Moll, R., Schwab, J., & Woosley, S. 2014, ApJ, 788, 75
Reilly, E., Maund, J. R., Baade, D., et al. 2016, MNRAS, 457, 288
Reinecke, M., Hillebrandt, W., & Niemeyer, J. C. 2002, A&A, 391, 1167
Remming, I. S., & Khokhlov, A. M. 2014, ApJ, 794, 87
Riess, A. G., Filippenko, A. V., Challis, P., et al. 1998, AJ, 116, 1009
Riess, A. G., Filippenko, A. V., Li, W., et al. 1999, AJ, 118, 2675
Riess, A. G., Macri, L. M., Hoffmann, S. L., et al. 2016, ApJ, 826, 56
Riess, A. G., Rodney, S. A., Scolnic, D. M., et al. 2018, ApJ, 853, 126
Roming, P. W. A., Kennedy, T. E., Mason, K. O., et al. 2005, Space Science Reviews, 120, 95
Röpke, F. K. 2007, ApJ, 668, 1103
Saio, H., & Nomoto, K. 1985, A&A, 150, L21
—. 1998, ApJ, 500, 388
Sato, Y., Nakasato, N., Tanikawa, A., et al. 2016, ApJ, 821, 67
Scalzo, R., Aldering, G., Antilogus, P., et al. 2014, MNRAS, 440, 1498
Schlafly, E. F., & Finkbeiner, D. P. 2011, ApJ, 737, 103
Segretain, L., Chabrier, G., & Mochkovitch, R. 1997, ApJ, 481, 355
Seitenzahl, I. R., Ciaraldi-Schoolmann, F., Röpke, F. K., et al. 2013, MNRAS, 429, 1156

Serkowski, K., Mathewson, D. S., & Ford, V. L. 1975, ApJ, 196, 261
Shapiro, P. R., & Sutherland, P. G. 1982, ApJ, 263, 902
Shappee, B. J., & Stanek, K. Z. 2011, ApJ, 733, 124
Shappee, B. J., Prieto, J. L., Grupe, D., et al. 2014, ApJ, 788, 48
Shen, K. J., Kasen, D., Weinberg, N. N., Bildsten, L., & Scannapieco, E. 2010, ApJ, 715, 767
Shen, K. J., & Moore, K. 2014, ApJ, 797, 46
Siebenmorgen, R., Voshchinnikov, N. V., & Bagnulo, S. 2014, A&A, 561, A82
Siebert, M. R., Dimitriadis, G., & Foley, R. J. 2018, Transient Name Server Classification Report, 75
Silverman, J. M., & Filippenko, A. V. 2012, MNRAS, 425, 1917
Silverman, J. M., Kong, J. J., & Filippenko, A. V. 2012, MNRAS, 425, 1819
Silverman, J. M., Vinkó, J., Marion, G. H., et al. 2015, MNRaS, 451, 1973
Sim, S. A., Seitenzahl, I. R., Kromer, M., et al. 2013, MNRAS, 436, 333
Smith, M. P., Nordsieck, K. H., Burgh, E. B., et al. 2006, in PROCSPIE, Vol. 6269, Society of Photo-Optical Instrumentation Engineers (SPIE) Conference Series, 62692A
Stevance, H. F., Maund, J. R., Baade, D., et al. 2017, MNRAS, 469, 1897
—. 2019, MNRAS, 485, 102
Stritzinger, M., & Leibundgut, B. 2005, A&A, 431, 423
Taam, R. E. 1980, ApJ, 242, 749
Tammann, G. A., & Reindl, B. 2013, A&A, 549, A136
Tanaka, M., Mazzali, P. A., Benetti, S., et al. 2008, ApJ, 677, 448
Tartaglia, L., Sand, D. J., Valenti, S., et al. 2018, ApJ, 853, 62
Thomas, R. C., Aldering, G., Antilogus, P., et al. 2011, ApJ, 743, 27
Tonry, J. L. 2011, PASP, 123, 58
Tully, R. B. 2015, AJ, 149, 171
Valenti, S., Sand, D., Pastorello, A., et al. 2014, MNRAS, 438, L101
van de Hulst, H. C. 1957, Light scattering by small particles (Wiley: New York)
Wang, L., Baade, D., Höflich, P., et al. 2006, ApJ, 653, 490
Wang, L., Baade, D., & Patat, F. 2007, Science, 315, 212
Wang, L., Goldhaber, G., Aldering, G., & Perlmutter, S. 2003a, ApJ, 590, 944
Wang, L., Howell, D. A., Höflich, P., & Wheeler, J. C. 2001, ApJ, 550, 1030
Wang, L., & Wheeler, J. C. 1996, ApJL, 462, L27
—. 2008, ARAA, 46, 433
Wang, L., Wheeler, J. C., & Höflich, P. 1997, ApJL, 476, L27
Wang, L., Baade, D., Höflich, P., et al. 2003b, ApJ, 591, 1110
Wang, X., Filippenko, A. V., Ganeshalingam, M., et al. 2009, ApJL, 699, L139
Wang, X., Wang, L., Filippenko, A. V., et al. 2012, ApJ, 749, 126
Webbink, R. F. 1984, ApJ, 277, 355
Whelan, J., & Iben, Jr., I. 1973, ApJ, 186, 1007
Woosley, S. E., & Weaver, T. A. 1994, ApJ, 423, 371
Woosley, S. E., Weaver, T. A., & Taam, R. E. 1980, in Texas Workshop on Type I Supernovae, ed. J. C. Wheeler, 96–112
Yaron, O., & Gal-Yam, A. 2012, PASP, 124, 668
Yoon, S.-C., Podsiadlowski, P., & Rosswog, S. 2007, MNRAS, 380, 933
Yoshida, S. 2018, arXiv e-prints, arXiv:1812.10898
Zhai, Q., Zhang, J.-J., Wang, X.-F., et al. 2016, AJ, 151, 125
Zhang, K., Wang, X., Zhang, J., et al. 2016, ApJ, 820, 67
Zhao, X., Wang, X., Maeda, K., et al. 2015, ApJS, 220, 20
Zheng, W., Silverman, J. M., Filippenko, A. V., et al. 2013, ApJL, 778, L15
Zheng, W., Filippenko, A. V., Mauerhan, J., et al. 2017, ApJ, 841, 64

APPENDIX

A. APPENDIX: VLT SPECTROPOLARIMETRY REDUCTION

All VLT spectropolarimetric observations were conducted with the 300V grism coupled to a 1″ slit. The high-pass was chosen to stop second order light, from the flux at $\lambda \lesssim 4400$ Å, contaminating the spectrum at wavelength $\lambda\,6500$ Å. This configuration provides a wavelength range of $\sim 4400 - 9200$ Å with a resolution of 11.0 Å ($FWHM$) at a central wavelength of 5849 Å, and a dispersion of $\sim$2.6 Å pixel^{-1}. At both epochs, the spectropolarimetric observations consisted of four exposures each with the half-wave retarder plate positioned at angles of 0°, 45°, 22°.5, and 67°.5, respectively. Exposure times at each plate angle were chosen to be 15 minutes and 2 minutes for epoch 1 and epoch 2, respectively. The spectra were flux calibrated using one 60 s integration of the photometric standard star LTT3218, with the polarimetry optics in place and the retarder plate at 0 degrees.

Spectra obtained at each retarder plate angle were bias subtracted, flat-field corrected and wavelength calibrated using standard tasks within IRAF. The ordinary and extraordinary beams were processed separately, and the typical RMS error on the wavelength calibration gives $\sim$0.25 Å.

The Stokes parameters describe the polarization state of the electromagnetic radiation. I gives the total intensity of the beam, Q and U can be recognized by the projection of the radiation E-vectors to different directions on the plane of the sky ($+Q$ ↔, $-Q$ ↕, $+U$ ↙↗, $-U$ ↖↘). Briefly speaking, the Stokes parameters Q and U can be derived via Fourier transformation, as described in the VLT FORS2 User Manual (Anderson 2018):

$$\begin{aligned} Q_0 &= \frac{2}{N}\sum_{i=0}^{N-1} F(\theta_i)\cos(4\theta_i) \\ U_0 &= \frac{2}{N}\sum_{i=0}^{N-1} F(\theta_i)\sin(4\theta_i), \end{aligned} \tag{A1}$$

where $F(\theta_i)$ give the normalized flux difference between the ordinary (f^o) and extra-ordinary (f^e) beams:

$$F(\theta_i) = \frac{f^o(\theta_i) - f^e(\theta_i)}{f^o(\theta_i) + f^e(\theta_i)}. \tag{A2}$$

In the case of this study, four observations were carried out at retarder angles of 0, 22.5, 45, and 67.5 degrees ($N = 4$). Therefore, $Q_0 = [F(0°) - F(45°)]/2$, and $U_0 = [F(22°.5) - F(67°.5)]/2$. The measured Stokes parameters were also corrected for the offsets to the zero angle of the retarder plate ($-\Delta\chi(\lambda)$). Typical chromatic dependence of the zero angle was less than 4 degrees, since a superachromatic half wave plate is used with FORS2 (see Figure 4.1 of the VLT FORS2 User Manual). The tabulated values are available from the FORS instrument description page[8].

A small amount of wavelength-dependent instrumental polarization in FORS2 ($\lesssim 0.1\%$) has been investigated by Fossati et al. (2007) and Siebenmorgen et al. (2014). Further analytical quantification by Cikota et al. (2017) gives:

$$\begin{aligned} Q^{\rm Instr.}(\lambda) &= 9.66 \times 10^{-8}\lambda + 3.29 \times 10^{-5} \\ U^{\rm Instr.}(\lambda) &= 7.28 \times 10^{-8}\lambda - 4.54 \times 10^{-4}, \end{aligned} \tag{A3}$$

[8] http://www.eso.org/sci/facilities/paranal/instruments/fors/inst/pola.html

where λ is the observed wavelength in Å. In many cases, in order to reduce slit losses, the instrument position angle, χ, is aligned to the parallactic angle and not necessarily aligned to the north celestial meridian, i.e. $\chi \neq 0$. Therefore, the correct measurement of the polarization position angle requires transforming the Stokes parameters from the instrumental reference frame to the sky reference frame. The instrumental polarization tends to be constant among different instrument position angles (see, i.e. Fig. 8 of Siebenmorgen et al. 2014) and needs to be corrected before the transformation between the instrument and sky reference frames (see, i.e. Bagnulo et al. 2017). Linear polarization measurement follows the transformation given by Equation (10) in Bagnulo et al. (2009). Therefore, we write the expression of the Stokes parameters as the following:

$$\begin{aligned} Q &= (Q_0 - Q^{\rm Instr.})\cos(2\chi) + (U_0 - U^{\rm Instr.})\sin(2\chi), \\ U &= -(Q_0 - Q^{\rm Instr.})\sin(2\chi) + (U_0 - U^{\rm Instr.})\cos(2\chi). \end{aligned} \tag{A4}$$

We set χ to 0 deg in our observations and subtract the instrumental polarization calculated from Equation A3 to correct the instrumental effect. The wavelength scale of the Stokes parameters and calculated polarization were also corrected to the rest-frame by adopting the host galaxy recessional velocity (1582 km s^{-1}).

B. APPENDIX: 'CMAGIC' EXTINCTION ESTIMATION

Following Wang et al. (2003a), we fit the linear region of the magnitude−color diagram from 5 to 27 days after the $B-$band maximum light with the CMAG relation:

$$B = B_{BV} + \beta_{BV}(B - V) \tag{B5}$$

Here β_{BV} and B_{BV} denote the slope and the value for the intercept at $(B - V) = 0$ of the linear region in the CMAG diagram, respectively. According to Wang et al. (2003a), the term $\mathcal{E}(B - V)$, namely 'CMAGIC' color excess, is given by:

$$\mathcal{E}(B - V) = \frac{(B_{\rm max} - B_{BV})}{\beta_{BV}}. \tag{B6}$$

The 'CMAGIC' color excess for a reddening-free SN, or $\mathcal{E}_0$, also shows a dependence on the Δm_B^{15}, which characterizes the width of the light curve. By fitting a sample of SNe with little or no color excess ($B_{\rm max} - V_{\rm max} < 0.05$ mag) and also correcting that using $E(B-V)$ of Phillips et al. (1999), the linear dependence of $\mathcal{E}_0$ on Δm_{15}^B derived from this low-extinction sample of Type Ia SNe gives:

$$\mathcal{E}_0 = (-0.118 \pm 0.013) + (0.249 \pm 0.043)(\Delta m_{15} - 1.1), \tag{B7}$$

Finally, the color excesses of Type Ia SNe can be estimated using the formula:

$$E_{BV}(B - V) = \mathcal{E}(B - V) - \mathcal{E}_0; \tag{B8}$$

We fit the absolute B magnitude and $B - V$ color of SN 2018gv between +5 and +27 days to the CMAG relation described by Equation B6. Both quantities have been corrected for the Galactic extinction. The result gives $\mathcal{E}^{\rm 18gv}(B - V) = -0.127 \pm 0.018$ mag, $\mathcal{E}_0^{\rm 18gv} = -0.155 \pm 0.020$ mag, and $E_{BV}^{\rm 18gv} = 0.028 \pm 0.027$ mag.

A sanity test was carried out by applying the same procedure to the B and $V-$band photometry of SN 2011fe published in Munari et al. (2013). In order to be consistent with our extinction estimation of SN 2018gv, we applied only the Galactic extinction, $E(B-V) = 0.01$ mag to the photometry and color of SN 2011fe based on the estimated host Na ID absorption features from high-resolution spectroscopy (Patat et al. 2013). A Cepheid distance modulus $\mu_0 = 29.04$ was used for SN 2011fe (Shappee & Stanek 2011). Finally, we conducted the CMAGIC fitting to estimate the host extinction: $\mathcal{E}^{11fe}(B-V) = -0.125 \pm 0.018$ mag, $\mathcal{E}_0^{11fe} = -0.125 \pm 0.020$ mag, and the color excess of SN 2011fe from the host gives $E_{BV}^{11fe} = 0.000 \pm 0.027$ mag. This is consistent with the evidence for very little dust extinction of SN 2011fe in its host galaxy (Tammann & Reindl 2013; Patat et al. 2013; Pereira et al. 2013; Zhang et al. 2016).

C. APPENDIX: STEPS OF THE PSEUDO-BOLOMETRIC LIGHT CURVE CONSTRUCTION

(1) **Extinction correction and magnitude conversion.** We correct for the Galactic extinction and the host extinction listed in Table 4 to the $UBg'Vr'i'$-band photometry of SN 2018gv. The UBV-band photometry was converted to the AB system adopting the linear offsets given in Table 1 of Blanton & Roweis (2007). Specifically, $U_{\rm AB} = U_{\rm Vega} + 0.79$, $B_{\rm AB} = B_{\rm Vega} - 0.09$, and $V_{\rm AB} = V_{\rm Vega} + 0.02$;

(2) **Synthetic photometry on template spectra.** We adopt the spectral template of Type Ia SNe built by Hsiao et al. (2007) and register the spectral templates to the nearest photometric phase. For each photometric epoch, we then perform synthetic photometry on the appropriate spectrum for the $UBg'Vr'i'$ bandpasses;

In practice, our synthetic photometry was carried out by first calculating the mean photon flux density for different bandpasses:

$$\langle \lambda F_b(\lambda) \rangle = \frac{\int \lambda F_\lambda T_b(\lambda) d\lambda}{\int \lambda T_b(\lambda) d\lambda}, \tag{C9}$$

where F_λ is the flux spectrum in unit of erg cm^{-2} s^{-1} Å^{-1}, and $T_b(\lambda)$ gives the unitless throughput for a certain bandpass, which is denoted as b. Then we synthesize the magnitude in the AB system to compare with our photometry of the SN. According to the *Synphot* User's Guide for the *HST* *Synphot* [9] software, we first obtain the ST magnitude, which is similarly defined as the AB system but gives constant flux per unit wavelength interval rather than unit frequency:

$$STMAG_b = -2.5 \times \log_{10} \langle \lambda F_b(\lambda) \rangle - 21.1. \tag{C10}$$

The conversion between the ST and AB systems is given by:

$$ABMAG_b = STMAG_b - 5\log_{10}\lambda_b^{\rm pivot} + 18.692 - ZP_b. \tag{C11}$$

The source-independent pivot wavelength is defined by:

$$\lambda_b^{\rm pivot} = \sqrt{\frac{\int \lambda T_b(\lambda) d\lambda}{\int T_b(\lambda) d\lambda/\lambda}}, \tag{C12}$$

[9] http://www.stsci.edu/institute/software_hardware/stsdas/synphot

and the zero points for $UBgVri$ bandpasses can be found in Table 3 of Pickles & Depagne (2010);

(3) **Scaling factors between template spectra and photometry.** We calculate the differences between the photometry of SN 2018gv after applying the corrections in step (1) and the synthesized AB magnitude of each template spectrum for each band obtained in step (2). The difference magnitudes were converted into flux space to obtain the scale factors between the observations of SN 2018gv and template spectra, shown in the middle panel of Fig. 12. Therefore, multiplying the scale factor for each bandpass to $\langle \lambda F_b(\lambda) \rangle$ calculated from the corresponding template spectrum gives the mean photon flux density of SN 2018gv at a certain bandpass. This is shown by the filled symbols in the upper panel of Fig. 12. Abscissae are given by the pivot wavelength of each bandpass calculated by Equation C12. Three different colors and symbols illustrate the construction of the spectral energy distribution (SED) of SN 2018gv at three epochs. For each epoch, the abscissa of the leftmost and the rightmost points are determined by $\lambda_U^{\rm pivot} - FWHM_U$ and $\lambda_i^{\rm pivot} + FWHM_i$, respectively, while the two ordinates are assigned to $\langle \lambda F_U(\lambda) \rangle/2$ and $\langle \lambda F_i(\lambda) \rangle/2$, respectively;

(4) **The supernova SED.** We connect the mean photon flux density at $UBg'Vr'i'$ bandpasses and the leftmost and the rightmost boundaries described in step (3) to construct the optical SED of SN 2018gv (SED-dots), shown by the dotted lines in the upper panel of Fig. 12. We also warp the template spectra using linear interpolation to the scale factors (SED-warp). The warped spectra at three epochs are also presented by the solid lines in the upper panel of Fig. 12;

(5) **Integrate the SED to obtain the pseudo-bolometric luminosity.** For each epoch, we integrate the SED over the wavelength $\sim 1660-8180$ Å for both SED-dots and SED-warp to calculate the pseudo-bolometric luminosity. The pseudo-bolometric luminosities of SN 2018gv before $t = 100$ days calculated using SED-warp are on average (4.0±1.1)% higher than those using SED-dots. This discrepancy results from the construction of SEDs, see Brown et al. (2016).

The errors due to photometric uncertainties of each bandpass were computed through a Monte Carlo re-sampling approach using the photometric errors. The typical error before $t = 100$ days amounts to 0.4% of the luminosity. The total error of the pseudo-bolometric luminosity is dominated by the systematical difference between choices of the SED. We characterize this by calculating the variance between the SED-dots and SED-warp integrations. Finally, for each epoch, we add this systematical uncertainty and the error due to photometry in quadrature to obtain the final uncertainties in the pseudo-bolometric light curve. The median value of the final uncertainties is 3.0%±0.8%. The result of the host-galaxy extinction estimation is consistent with no extinction within the associated uncertainties (see Section 3.1 and Table 4). Therefore, we did not include the uncertainties in the estimation of the host galaxy extinction.

D. APPENDIX: ISP ESTIMATION

We identify spectral regions that are likely to be intrinsically depolarized due to the overlap of many Fe absorption wings. This "line blanketing" has a significant effect on opacities, and the spectral regions are significantly depolarized since the line blanketing opacity dominates over electron scattering opacity. As suggested in Howell et al. (2001) and Maund et al. (2013), we start by considering the wavelength region of $4800-5600$ Å (region A) and $5100-5300$ Å (region B) as the intrinsically depolarized regions of SN 2018gv. We notice that there are suspicious line polarization patterns, at epoch 1, in the flux-normalized Stokes Q and U spectra (see panels b-c of Fig. 14 and Section 5.4.3), possibly associated with the S II λ5454 and λ5640 lines at a velocity of $v \sim -13{,}800$ km s^{-1}. The expected effects of line-blanketing, instead, appear particularly prominent at wavelengths below ∼5000

Å (Leonard et al. 2005). We also consider the additional wavelength region C, defined as $4800-5100$ Å.

We measure the Stokes parameters by taking the error-weighted mean value across these wavelength ranges. The measured values at epoch 1 are:

$$\begin{aligned} Q^{A}_{\rm ISP1} = 0.19\% \pm 0.10\%, U^{A}_{\rm ISP1} = -0.41\% \pm 0.07\%, \\ Q^{B}_{\rm ISP1} = 0.26\% \pm 0.06\%, U^{B}_{\rm ISP1} = -0.39\% \pm 0.08\%\text{fi} \\ Q^{C}_{\rm ISP1} = 0.08\% \pm 0.07\%, U^{C}_{\rm ISP1} = -0.37\% \pm 0.06\%; \end{aligned} \tag{D13}$$

At epoch 2, the Stokes parameters over the same wavelength ranges are:

$$\begin{aligned} Q^{A}_{\rm ISP2} = 0.08\% \pm 0.12\%, U^{A}_{\rm ISP2} = -0.49\% \pm 0.08\%, \\ Q^{B}_{\rm ISP2} = 0.07\% \pm 0.15\%, U^{B}_{\rm ISP2} = -0.50\% \pm 0.08\%, \\ Q^{C}_{\rm ISP2} = 0.06\% \pm 0.13\%, U^{C}_{\rm ISP2} = -0.48\% \pm 0.07\%. \end{aligned} \tag{D14}$$

At epoch 1, the possible polarization associated with S II λ5454 and λ5640 makes the Stokes Q and U measured in regions A and B systematically 0.11% and 0.08% higher than those measured at epoch 2, respectively. It can be seen that $Q^{C}_{\rm ISP1}$ is consistent with $Q^{C}_{\rm ISP2}$. For each spectral region, the measurements at both epochs are consistent within the associated uncertainties. Considering that the observation at epoch 2 achieved a higher S/N, which provides a more accurate estimate of the ISP, we adopt the error-weighted mean Stokes parameters measured over the three regions at epoch 2 to represent the Stokes parameters for the ISP: $Q_{\rm ISP} = 0.07\% \pm 0.16\%$, $U_{\rm ISP} = -0.49\% \pm 0.09\%$. The uncertainties were estimated by adding the average errors of the Stokes parameters over the three wavelength ranges, the standard deviation of the Stokes parameters over the three wavelength ranges, and the uncertainties of the weighted mean Stokes parameters in quadrature.